POLITECNICO DI TORINO

Collegio di Ingegneria Energetica

Master of Science Course
in Energy and Nuclear Engineering

Master of Science Thesis

Parametric analysis of cold energy storage system within LAES

Tutor

Prof. Verda Vittorio

Supervisors

Prof. Judith Evans
Ing. Daniele Negro

Candidate
Negro Frer Marco

2018

"E l'invincibile non è quello che vince sempre,
ma quello che anche se perde, non è vinto mai"
Lorenzo "Jovanotti" Cherubini

Acknowledgements

Vorrei ringraziare di cuore innanzitutto i miei genitori, sostenitori amorevoli e coraggiosi durante tutto questo straordinario percorso, ma soprattutto punti di riferimento fondamentali per il mio oggi e per il mio domani.

Un grazie a mio fratello più piccolo, che mi sprona quotidianamente, più con i gesti che con parole forse, dandomi un forte esempio di forza d'animo e perseveranza.

Agli amici di una vita, troppo banalmente definiti una seconda famiglia, perché sono ancora più. Supporto morale, insostituibile ed essenziale in primo luogo all'interno della mia vita e successivamente anche nel mio percorso universitario. Con loro ho condiviso gioie e dolori, lunghi periodi di stress, ma soprattutto di felicità, percepiti anche quando a dividerci c'erano più di mille chilometri di distanza.

Alle mie speciali amiche e colleghe universitarie, senza le quali probabilmente non sarei arrivato fino a qui con questa passione e con questi risultati, con cui ho condiviso una splendida anche se difficile esperienza, stracolma di emozioni forti. Non voglio dimenticare di ringraziare tutti i compagni del Poli, a tutte le persone vere conosciute in coda a un esame o in un'aula, durante una lezione troppo pesante, che magari si sono persi durante il percorso.

Un grazie enorme ai miei nonni, ai miei zii e a mio cugino, che si sono dimostrati uno splendido supporto durante tutti questi anni, mostrandomi insegnamenti di vita che mi hanno formato profondamente.

Un grazie fondamentale va doverosamente alla persona che mi ha sostenuto durante il mio difficile percorso di tesi in Inghilterra, l'Ing. Daniele Negro, che oltre ad avermi seguito con passione e con dedizione durante il mio lavoro, mi ha fornito insegnamenti ben più grandi dal punto di vista formativo e professionale. La mia più sincera gratitudine va a tutti i colleghi d'ufficio della LSBU e della RD&T di Bristol, che per sei mesi mi hanno accolto come una famiglia.

Desidero anche ringraziare il Professor Vittorio Verda che come docente ha contribuito attivamente alla mia formazione e con la sua supervisione mi ha dato la possibilità di concludere questo percorso universitario.

Un ringraziamento finale a tutte le persone che hanno dedicato anche solo un minuto della loro vita per contribuire ad accrescere la mia conoscenza, la mia esperienza e la mia felicità

Index

List of figures

List of tables

1 Introduction

"Climate change and energy are closely interlinked" (1): the global temperature is increased by 2°C with respect to pre-industrial level. EU commission underlined the necessity to shift to a low-carbon economy, with the target to "increase the share of renewable energy in gross final energy consumption to 20 % by 2020" (1).

The last 15 years have seen an unpredictable change in the production and in the consumption of energy, due to high growth in renewable market. From around 8.5% in 2004, the share of energy from renewable sources increase to 17% in 2016 in Europe (2) and the trend shows an increase in the future, due consistent global investments (USD 278.5 billion in 2015 (3)) and awareness of the environmental problem related to carbon emissions.

The landscape of the energy sector is totally changed: the energy production become more affected by daily and seasonal discontinuity due to the intermittence of RES that generated a lot of problem related to the stability of the electrical grid, affecting the Bulk Grid Reliability, making more complicate to prevent voltage collapse, cascading outages and uncontrolled separation (4).

The search for some viable solutions, to properly integrate the Renewable power and balance the grid, found different solutions, including the demand management, the interconnection with external grid and the electrical energy storage(EES) (5).

Power demand varies with time and the price of electricity follows it. When the electric demand is higher, the power suppliers must integrate the base-load power with flexible form of generation such as fossil or nuclear. These costs could be minimized with the insertion of EES connected to the grid (6). When the demand is low, the electrical energy could be stored from the grid though various medium and reconvert when it is needed more and so when the price is higher, generating revenues for EES owners. In addition to that, this technology allows to provide useful services to the management of the grid, such as shaving peaks, improving power reliability and contribute the realization of Smart Grids.

The concept of Smart Grid is not univocal and clarified but could be express as "comprises everything related to the electrical system between any point of electricity production and any point of consumption" (6). This technology is designed to integrate and balance the consumer

needs with the electricity production, minimizing the inefficiencies of the grid, through use of dynamic control systems

The selection of the appropriate EES technology is challenging, because for each country and for each situation there is a different scenario to evaluate. There exist mainly two different approach in Electric energy storage, the Bulk storage and the Distributed storage. The first one is usually built by some private company and provides no direct benefit for the end costumer, while the distributed storage is more efficient and creates interesting possibilities for electric power costumers: shifting consumption away from high demand hours, reducing the demand peak and guarantee a backup power if there is a black out (7). One other drawback of Bulk storage is that exploit the public grid to link the production point and the utility where the energy is consumed. To minimize the losses, one study conducted in Colorado explain that any type of energy storage is more efficient if it is located near the point of consumption (7).

The EES could be divided into 5 main categories, Mechanical, Electrochemical, Electrical, Thermal storage and Chemical Storage.

Currently, Mechanical storage accounts for well over 99% of the global storage capacity, because it is a simple and efficient technology, deployed from 19th century and however very mature. Its principal contributor is the PHS (Pumped Energy Storage), with more than 97% (8)of the total and with an installed power capacity of 127,000 MW (1,500,000 MWh). [6] The basic principle consists into generation of electricity, moving water between two reservoirs at different elevation.

The second contribution is due to CAES (Compressed Air Energy Storage) systems, that accounts only two commercial plants, with an installed capacity of 440 MW (3,730 MWh) (8). It is based on compressing air in off-peak time, storing it in caves and exploiting it when the demand and the price of energy become higher.

One other relevant technology for the electrical storage is the Sodium Sulphur Battery, with an installed capacity of 316 MW (1,900 MWh), which is characterized by high energy density and long-life cycles.

Considering the installed capacity, all other EES technologies remain marginal. Flywheels contribution, for the problem of short term storage duration is not very significative while supercapacitors are in early phase. Another technology with good prospects for the future is represented by chemical energy storage, but their role seems to be marked with the production of fuels, instead electrical injection to the grid.

The main parameters to classify the different EES technologies are the energy density, the power rating, the geological constrains and the maturity. For example, both PHS and CAES are affected by important geographical issues, like the presence of a water reservoir or a cave in the ground.

In the *figure 1.1* are represented the principal EES technologies, considering their role in terms of power in function of the discharge time at rated power. It appears clear that for large scale size, the principal competitors are PHS, CAES, Hydrogen & Fuel Cells and Cryogenic Energy Storage. While the first two technologies are in phase of commercialisation, the Hydrogen related with fuel cells has the current maturity level of Research and Development (9) and the Cryogenic energy storage is at the following state of Demonstration and deployment. For this reason, Hydrogen fuel cells technology would not be discussed in this work.

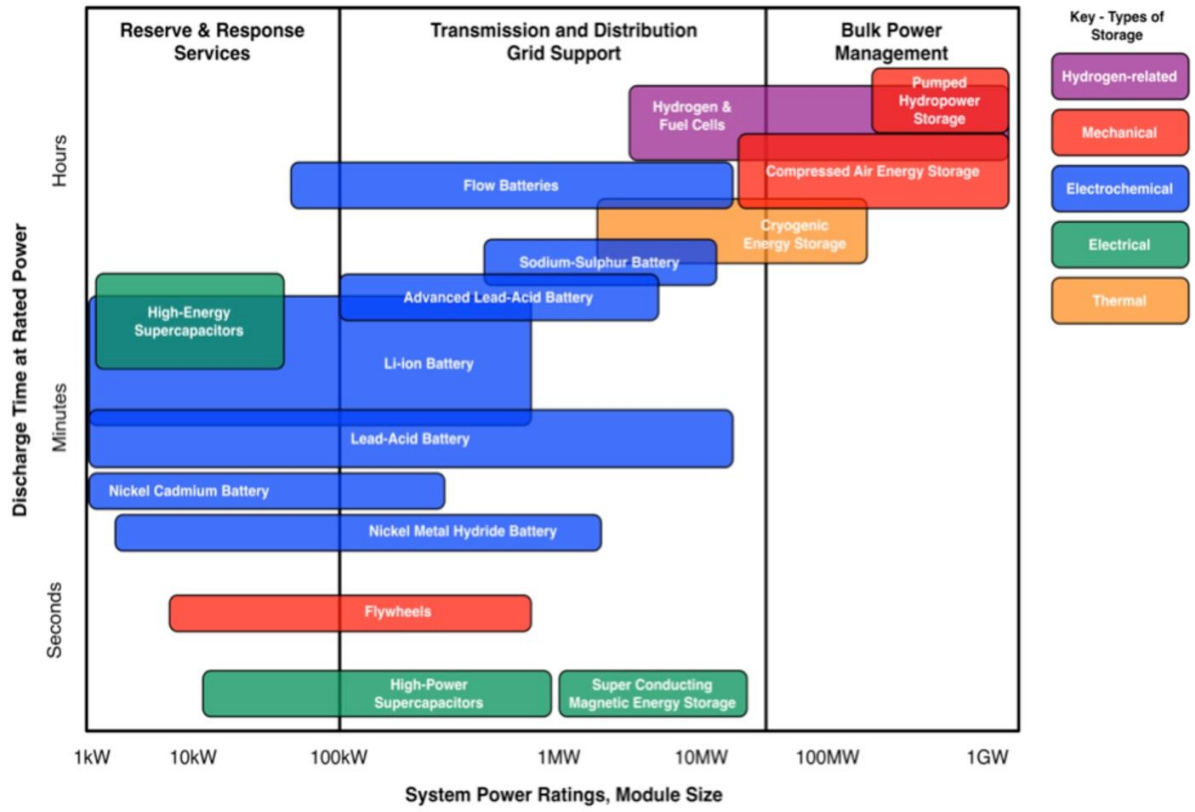

Figure 1-1:Applicable power ranges and discharge power duration of different energy storage technologies

The advantage of Cryogenic Energy Storage plant is expressed in no geographical restriction, so it would be easily located near existing factories or utilities. In control volume of that plants, there are many exchanges of heat fluxes with the external environment. This produces a

possible exploitation of heat/cold waste fluxes and allows an enhancement in energy efficiency via cogeneration.

The *table 1.1* shows a schematic comparison between the large-scale Electrical Energy Storage, that includes PHS, CAES and Liquid Air Energy Storage (LAES), to highlight the advantages and the drawbacks of each technology.

	PHS	***CAES***	***LAES***
Energy density (Wh/L)	0,5–1,5 (10), 1–2 (11)	3–6 (10), 2–6 (11)	120–200 (12)
Power rating (MW)	100–5000 (10)	Up to 300 (10)	10–200 (13)
Rated energy capacity (MWh)	500–8000 (10)	< 1000 (14)	2.5 (15)
Lifetime (years)	40–60 (10)	20–40 (10)	25+ (16)
Cycle efficiency (%)	70–85 (10)	42 (10)	55–80+ (16)
Response time	Minutes (17)	Minutes (17)	Minutes (12)
Storage duration	Hours–months (10)	Hours–months (10)	Hours (15), (16)
Power capital cost ($/kW)	2500–4300 (18)	400–800 (10)	900–1900 (16)
Maturity	Mature	Commercialized	Developing/demo

Table 1-1:Comparison of Large scale EES technology

In this parametric study is considered the LAES, a specific configuration of Cryogenic energy storage, where liquid air is used as cryogens. Many other fluids are available to be used as a medium with this technology, including liquid oxygen, liquid nitrogen, liquid helium and liquified natural gas. All of them must have a saturation temperature below -150°C, at ambient pressure. For its higher availability, air has been recently considered one of the most feasible options.

The EES technologies are characterized by a very high-power rating coupled with a long duration discharge time (>10 hours). All of them are also characterized by a relatively quick response time (some minutes) and long lifetime of the plant (>20 years).

The Cycle efficiency, also called Round Trip Efficiency (RTE), of the LAES considered is very high, but this value corresponds to the ideal conditions and is the consequence of using a waste heat from a co-located industry (Highview Cryo Energy System) (16). The capital cost is lower in average with respect to PHS and slightly higher than CAES.

The main drawback of LAES is represented by low Rated energy capacity, because the dimension of the considered plant is much smaller than existing PHS or CAES.

Furthermore, it's Energy density is two orders of magnitude higher, that means a smaller footprint. This is a great advantage: besides no geographical restrictions, LAES plants could be placed very close to any utility, increasing its feasibility and efficiency.

The LAES system represents a concrete alternative for the large scale EES.

Liquid Air Energy Storage concept proposes to use low-rating electricity, coming from renewable or from off-peak time from the grid, to feed compressors and liquefy air, directly from the environment. The liquid fluid is stored and when the demand is high, is pumped and evolved into gas turbines.

The standard working principle of LAES system is composed by three main processes: Liquefaction and Charge, Storage, Discharge and Power recovery (19) and it is suitable to integration with industrial heat/cold waste:

- *Stage 1: Liquefaction and Charge*

  During the Liquefaction process, ambient air is first filtered to remove moisture, CO_2, impurities and is compressed with a multi-stage intercooled compression. Once the gas reached low temperature and very high pressure, it passed through an expander, to liquefy it. The correct choice of the expander is trivial: the best candidates are represented by a throttling valve and a Claude Expander. It is not considered the use of a traditional turbine, due to the high presence of liquid at the outlet of the expansion.

- *Stage 2: Storage*

  The liquid air is now stored in low pressure insulated vessels, which function as an energy store, in a range of temperature between -160/-200 °C. The technology for this equipment is already deployed for the storage of liquid nitrogen, oxygen and LNG (20).

- *Stage 3: Discharge & Power recovery*

  When power is required, the liquid air is pumped to high pressure, passed through an evaporator and superheated through some Heat Exchangers, that could be represented by external environment or by waste heat (21), as represented in *figure 2*. Hence the high pressurized air is used to drive the turbines and produce electrical power.

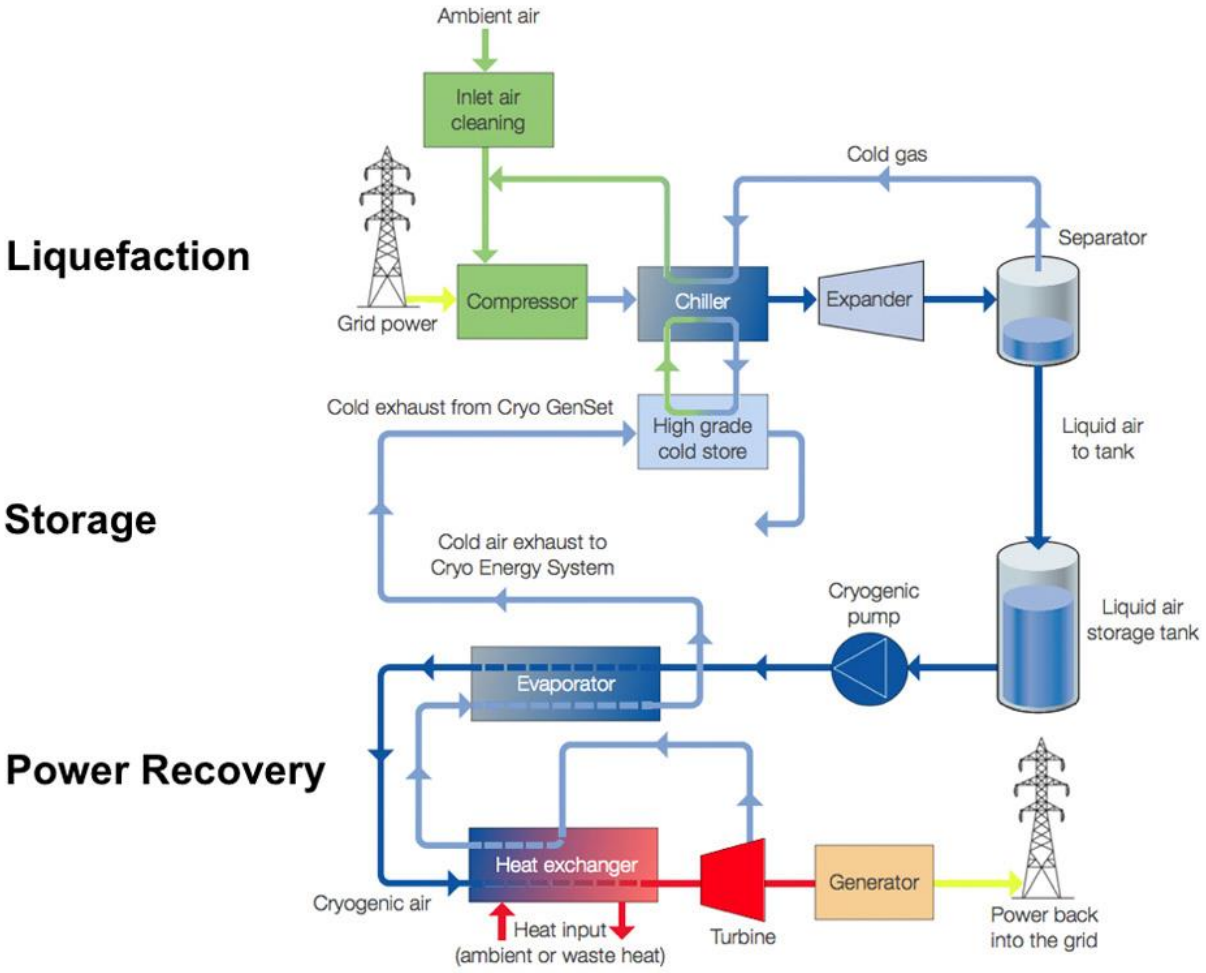

Figure 1-2:Standard configuration of Liquid Air Energy Storage cycle

Some arrangements could make the LAES technology more competitive: the liquefaction process produces a great amount of heat waste, while the re-gasification process generates a lot of cold energy.

A further superheating of the working fluid could be achieved exploiting the heat stored in the charge phase from compressors (20). At the same time, it could be provided some additional cooling capacity to the liquefaction process, if the cold flux from the evaporator was effectively stored. As alternative, the system could integrate waste cold from LNG industrial processes.

With this procedure, the reduction of the amount of work needed in the charge phase would be consistent, with an increasing of the overall efficiency.

In this work was presented a depth study about the Cold Energy Storage (CES), considering its fundamental importance in the global efficiency of the entire system: recent studies found out that the temporary storage of cold thermal energy streams using packed beds improves efficiency of LAES by almost 50% (22).

Nowadays, there exists three main different heat storage technologies: the sensible heat, latent heat and thermo-chemical. The choice of the type of storage depends on several parameters, listed in the *Table 1.2*.

	Sensible Storage	Latent Storage	Thermo-Chemical Storage
Energy *capacity* (*k*Wh/m^3)	15-60	100-150	300-500
Temperature range	100-250 °C	Small	Ambient temperature
Time of Storage	Limited (Thermal losses)	Limited (Thermal losses)	Unlimited
Transport distance	Low	Low	Large
Scale	Industrial	Pilot	Demo/pilot
Technology level	Simple	Medium	Complex

Table 1.2: Comparison different heat storage systems (23), (24)

In term of Energy capacity, the Thermo-chemical storage is highly the most performant technology, but the most important parameters in a practical case study are the level of

development, the complexity and the price. Only some pilot plants of this type are available now, so this solution could not be considered feasible.

Latent heat storage is a process at approximately constant temperature, criterion that does not match with cryogenic applications (the range of temperature is around 100°C), so the Sensible heat storage, coupled with a good insulation layer, remains the best solution, considering its flexibility, maturity level and low price. The low transport distance available, drawback of this technology, is not considered a problem, because the energy stored will be used in the same plant.

There are two different configurations for sensible thermal storage, the Active storage and the Passive storage. Thermal energy is recovered or transmitted by heat thermal fluid (HTF) to a fluid medium in the first configuration and to a solid medium in the second one.

This analysis is focused on the Passive storage, using a packed bed medium of gravel, because it represents high reduction in cost.

Before starting the discussion of the main topics of this work, a briefly literature review of the state of art of LAES and Cold Energy Storage technology was reported.

In the ***Chapter 3***, a parametrical evaluation of the Cold Energy Storage model was performed, including thermodynamic and design variables, to determine the best configuration to obtain the highest round-trip efficiency (RTE). The input variable of the system evaluated are:

- Inlet pressure (bar),
- Particle diameter of the gravel (mm),
- Insulation thermal conductivity (W/mK),
- Slenderness (H/D ratio of the storage vessel),
- Number of layers in series (-)
- Pressure Ratio X (-)

The Pressure Ratio parameter is an indicator that represents the choice which consists in adopting a theoretical model, obtained by Ergun equation (25), or an experimental model based on laboratory experiments performed by IRSTEA, with the purpose of estimate of the pressure drop of a quartzite packed bed

After the presentation of a detailed analytical model, a further analysis was necessary, with the goal of finding a univocal method to describe the system efficiency in a faster and simpler way, without using the whole analytical process.

This was operated in two different approach: the first determines the empirical coefficients of a sixth-grade polynomial approximation with a multiple regression method, that describes the efficiency of the Cold Energy Storage in function of the input parameter introduced before. To explain the second method, it was necessary to consider a certain database of simulation, that express the value of efficiency in function of the inputs: this approach proposes a numerical model that predict the value of a function at given point, by computing a weighted average of the know values of the function in the neighbourhood of the point (efficiency). This method is called Kriging or Gaussian process regression (26): in this way the efficiency of any CES could be predicted with any combination of the input parameters discussed in this study. Each method guarantees an estimated error of approximation. Furthermore, it was proposed a combination of the two methods described.

It's immediately seemed fundamental the importance of the right estimation of the pressure losses inside the storage: in the ***Chapter 4***, it was conducted an experimental evaluation of the pressure losses in a packed bed spheres, evaluating the performances of different Heat storage materials.

In ***Chapter 5***, it was proposed a study to analyse the thermal resistance of different Heat storage material. It was developed a simulated model to recreate the realistic heat transfer mechanism between the packed bed spheres and the heat transfer fluid (Liquid Air or Nitrogen) and it was performed an accelerated thermal stress to verify their integrity for the whole plant lifetime.

2 Cryogenic energy storage: Literature Review

In this section will be presented a literature review of the cryogenic energy storage technology, to recall its evolution across the last decades and to compare the existing models developed by different companies in terms of efficiency and reliability.

2.1 Technologies associated with the liquefaction cycle

To understand the development of the idea of cryogenic energy storage, it is important to introduce the historical evolution of its main component: the liquefaction cycle.

In 1895, Linde and Hampson independently developed the first industrial air liquefier: the Linde-Hampson cycle works with a Joule-Thompson effect, liquefying the fluid with an isenthalpic throttling valve, coupled with heat exchangers and a compressor (27).

This is considered the simplest approach to liquefy gases but involves at very high pressure (20 MPa) to operate, with the very low liquid yields of almost 6.5% (28).

To increase the liquid production of the liquefier, the temperature of the valve inlet needs to be smallest possible. Figure 2.1 shows the basic principle of the cycle, with a heat exchanger interposed between the compressor and the valve as a cooling source, exploiting the cold air coming from the liquid tank, after the separation from its liquid fraction.

The advantages of this cycle are presented by the structure simplicity and by no moving parts at the cold end. The poor performances of this cycle are due from the throttling valve, that presents very high irreversibility in terms of exergy losses, and from the heat exchanger, that shows an incorrect and inefficient match between the fluids temperature profile (29).

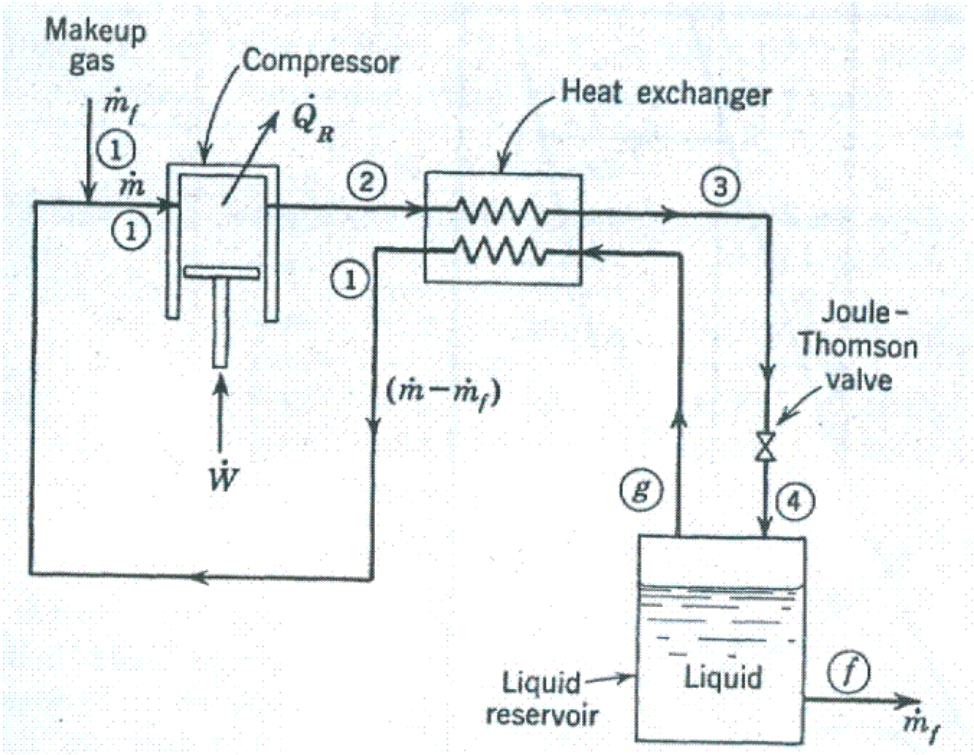

Figure 2-1:Layout of a Linde-Hampson cycle

The industrial production of liquid nitrogen began in 1902 (28), when Georges Claude proposed a system combining a throttling valve with a turbo-expander, in which an isentropic expansion increased the efficiency of the whole system. The working pressure in this configuration became lower (4 MPa) than J-T cycle and the problem due to the presence of vapour in the heat exchanger is eliminated, because all the cycle fluid is maintained as liquid phase. To ensure the highest thermal recovery between hot and cold fluxes and the best integration of the turbine, three heat exchangers are needed. At the outlet of the first HX, a large amount of the hot compressed air is splitted and drove to the expander: this step is fundamental because the cold low-pressure air at the outlet is coupled in the second heat exchanger with the hot fluid, providing a further cooling. This reduces its heat capacity and increase the efficiency of the recuperator (the third heat exchanger), making a closer profile between hot and cold flux and lowering the pinch point. The consequences of the adoption of the Claude cycle are an increasing of the liquid yield (14.5%) (28) of the system and a power production from the expander, improving the overall efficiency (30).

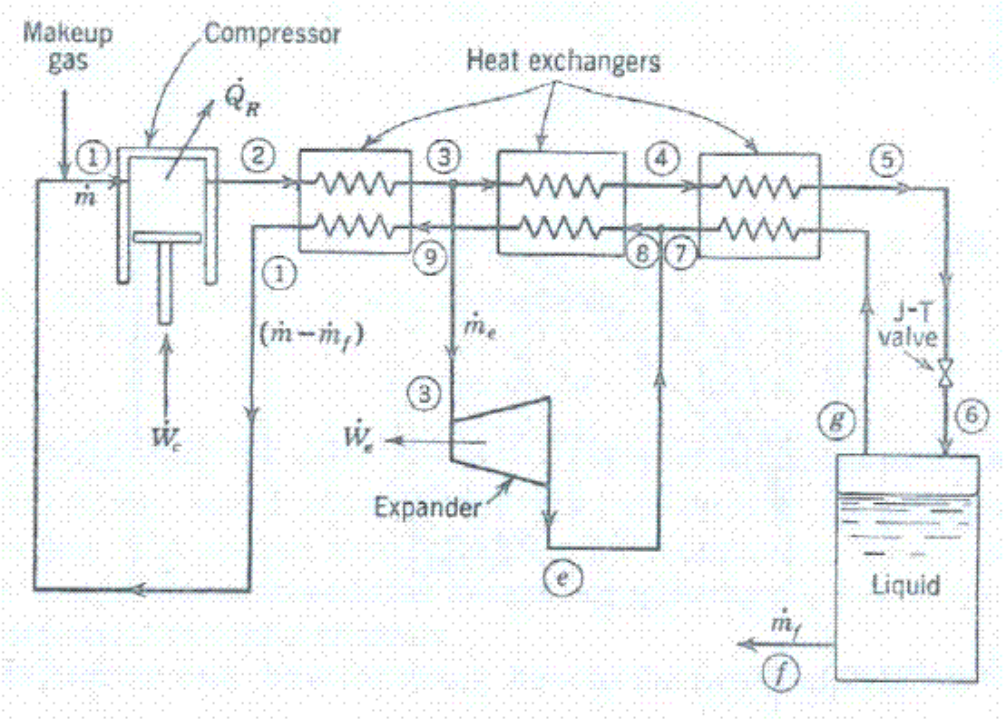

Figure 2-2:Layout of a Claude cycle

The most famous configuration to generate liquid air is the Collins cycle, which uses the same approach of Claude, inserting more turbines in parallel, to increase the performances. Using this cycle, the operational pressure could be lower with respect to previous design and the liquid yield could be higher.

Claude cycle and Collins cycle are very similar from both design and performances point of view and Abdo (28) underlined the uselessness of the more turbines, that will have the only effect of an increasing in terms of economical investments, promoting the Claude cycle the best option to liquefaction systems.

2.2 Technologies associated with the cryogenic energy extraction

"Four main methods have been proposed to extract the cold exergy from cryogen for power generation" (29). Cryogens contain a high grade cold thermal energy in the form of sensible and latent heat: to optimize their exergetic value, it is necessary to understand the best way to use them.

The first is called direct expansion method: the liquid air is pumped and heated up through a heat exchanger with ambient air o waste heat from industries and it expands directly in the turbine, producing power. In this situation the thermal energy is partially transformed in pressure energy, pumping the cryogen to high pressure.

The second configuration provides an exploitation of the cryogen to condensate the working fluid of a Rankine cycle. The optimize the system, it should be chosen a working fluid with a liquefaction point slightly higher than the cryogen. This application could find also available with the Liquefied Natural Gas (LNG) at industrial scale. The efficiency of this cycle will be improved with the use a cascading configuration.

The third technology consist of precooling the inlet of a gas compressor of a Brayton cycle with the liquid cryogen, to increase the efficiency of the cycle of almost 8% in a model demonstration performed for a combined cycle power plant coupled with LNG (31). Another work demonstrates that the efficiency of a Brayton could be improved between 7-25% using three-stage cryogenic intercooling at the output of a multi-stage turbine. This method to directly recover the cryogenic energy is not very performant because the cooling of a gas requires only sensible heat.

The fourth technology comprehends all the possible combination of the previous technology, converting part of the thermal exergy in pressure exergy. In the *figure 2.3* from Li. (29) are showed the different configuration: the *figure 2.3(a)* presents a direct-expansion-Rankine hybrid cycle, where first the cryogen condenses the working fluid of the Rankine cycle and then expands directly in a turbine. A pilot plant was developed in Japan with this method in 1970 (32).

The *figure 2.3(b)* represents a direct-expansion-Brayton cycle, where the cryogen is first exploited to cool down the working fluid at the inlet of the compressor before expanding in turbine. This configuration reached an overall exergy efficiency of 46% in a combined cycle with liquid nitrogen (33).

In *figure 2.3(c)* the liquid cryogen is pumped to supercritical pressure and temperature and used to cool down the low-pressure inlet working fluid at the compressor inlet of a turbo-gas system. Later, the low-grade cold is used to condense the working fluid of a Rankine cycle. This configuration could be very interesting if applied in a combined cycle with the oxy-fuel combustion of LNG.

The *figure 2.3(d)* shows an implementation of the previous configuration, considering a direct expansion of the cryogen in an intermediate phase, to improve the whole efficiency. Bai and Mang investigated this method with the use of nitrogen as Brayton cycle working fluid and ammonia-water as Rankine cycle working fluid (34).

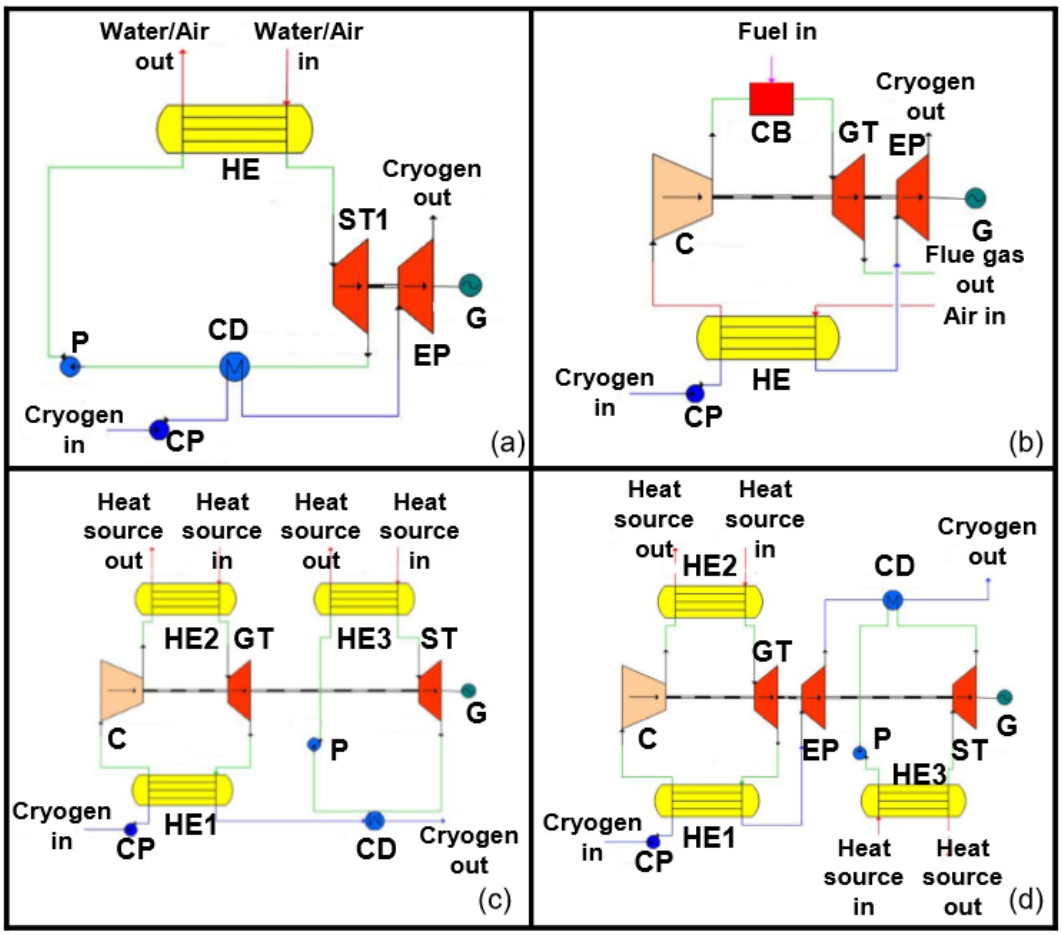

Figure 2-3:Combination of cryogenic energy extraction technologies

The cryogenic exergy efficiency of the systems assumes values varying from 20-60% in the configuration *a* and *c*, while reaches value higher than 60% in the others (29). These values of performances are related only with the energy extraction from the cryogen, so not considering the efficiency of the liquefaction process, where take place the highest irreversibility.

2.3 Simulated model and Pilot plants

The first demonstrator plant was built in 1998 by Mitsubishi Heavy Industries, Ltd. The liquid air discharge is pumped to 150 bar, evaporated by environmental air and superheated by the exhaust of the turbine. It expands, from 130 bar to 80, in a turbine on the same shaft of the turbopump, to drive it. Then passed through a combustion chamber and expand in a gas turbine to generate power. The efficiency recorded was almost 77% (35), without considering the power needed for the liquefaction process, whose operation parameters are not declared in the paper. Other important parameters as the starting time and the response at the load fluctuations were tested, with excellent results: all problems founded were basically solvable.

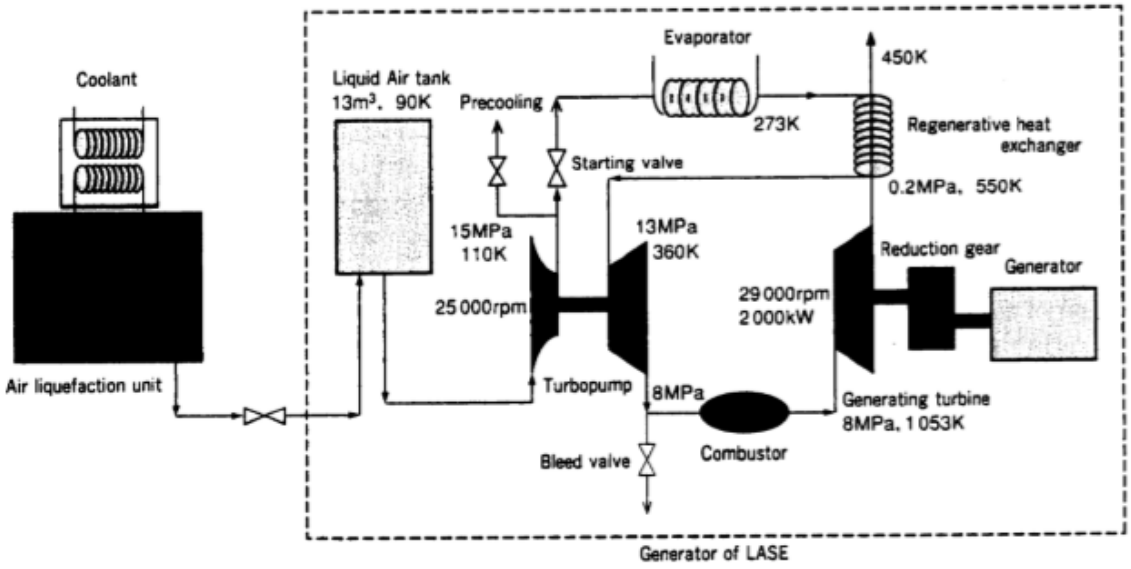

Figure 2-4:Mitsubishi demonstrator plant layout

In the following part of this section, are presented some investigated model and demonstrator systems where cryogenic energy storage is integrated in other systems and the relative parameter of system performance is related with the overall efficiency of the plants, from the production of liquefied cryogen to the power production unit.

The second attempt was performed by Hitachi Ltd. (36) in 2005 after the work of Wakana: he proposed a generation plant as a combination of a liquid air storage tank with a combustor and a gas turbine driven by the exhaust gas. The compressed air is first cooled down by LNG stored in liquid phase and then stored in a liquid air storage, that is arranged inside the cold energy regenerator, to minimize the thermal losses. With the insertion of a cold energy regenerator,

was claimed an increase from 20% to 80% of the liquid yield. The liquid LNG is then vaporized and heated up by some heat exchangers represented by the sea water. Finally, they never built a real demonstrator.

In *figure 2.5* is represented the work of Ameel (37), that describes a combined Rankine cycle with a Linde-Hampson liquefaction system, choice due to the simplicity of this configuration.

Liquid air is withdrawn from the storage to be pressurized, evaporated, expanded over a turbine and released in the environment. The difference with a real cycle is the absence of the condenser, due to the discharge of the air at the end of each cycle. This cycle needs an external heat supply to work, provided by environment or industrial waste heat. With the hypothesis of the temperature of 300 K heat supply, the overall plant efficiency is 43% in ideal conditions, but the value decreases to 22% (37) if the turbine and the compressor are not considered isentropic and if there are considered the exergy losses in the heat exchanger.

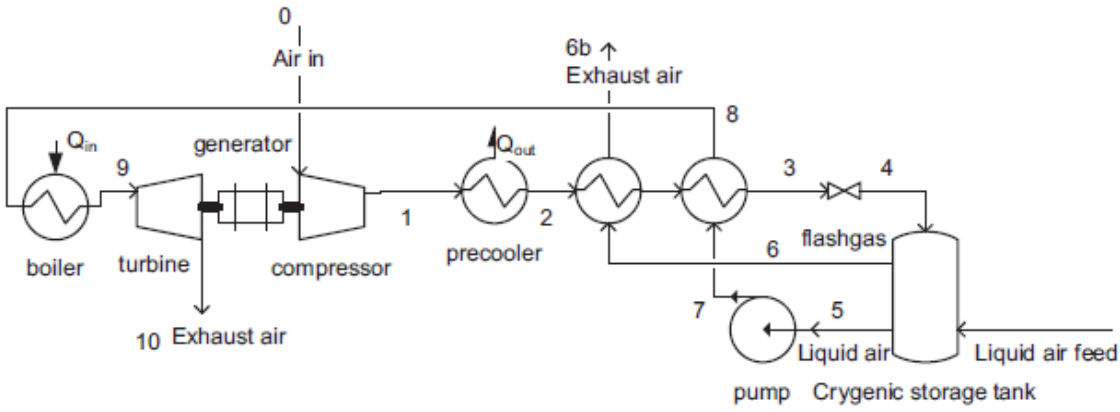

Figure 2-5:Combined Rankine - Linde-Thompson cycle

The research promoted by Morgan (38), showed a liquid air energy storage (LAES) system with the integration of the cold storage. The cycle efficiency could be incredibly increased with the 'cold recycle', by recovering the cold thermal energy in the discharge phase, when the liquid air passes through the evaporator and cool down the air during the liquefaction process. In this model is considered a Claude cycle, composed by a chain of three cold turbine to increase the cold recycle amount and the round-trip efficiency. With the hypothesis of 20 MW power recovery system and a 12 h recharge time, this system reaches an overall efficiency of 57% in a realistic configuration. Based on this study, Highview Power Storage, with the collaboration of the University of Birmingham, built the first fully integrated liquid air energy storage system

with a rated power of 350 kW and a rated capacity of 2.5MWh (39), that was connected to the grid from 2011 to 2014. The liquefaction unit, composed by a compressor and a booster driven by a cryogenic turbine, is small compared to the commercial size, therefore the efficiency is not optimized (17% instead a proved value of 70%). In this plant the hot thermal storage is charged through the steam supplied by the combined cycle power plant near the university. The plant showed an excellent response time during ramp down and during modulation of the power. The round-trip efficiency of a real plant with a power rate of 10MW is estimated around 60%.

Abdo (28) analyses the possibility to build a cryogenic energy storage plant with both cold and hot energy storage. In *figure 2.6* is presented a solution with the integration of a thermal solar system (SH). The dashed line represents the control volume of the Claude liquefaction process used. The hot flux from the compressors in the liquefaction process is stored in a sensible heat storage with Therminol or through a phase change material (PCM) and used after to superheat the air before the inlet of the turbine. The value of round-trip efficiency reached with this configuration is almost 63%.

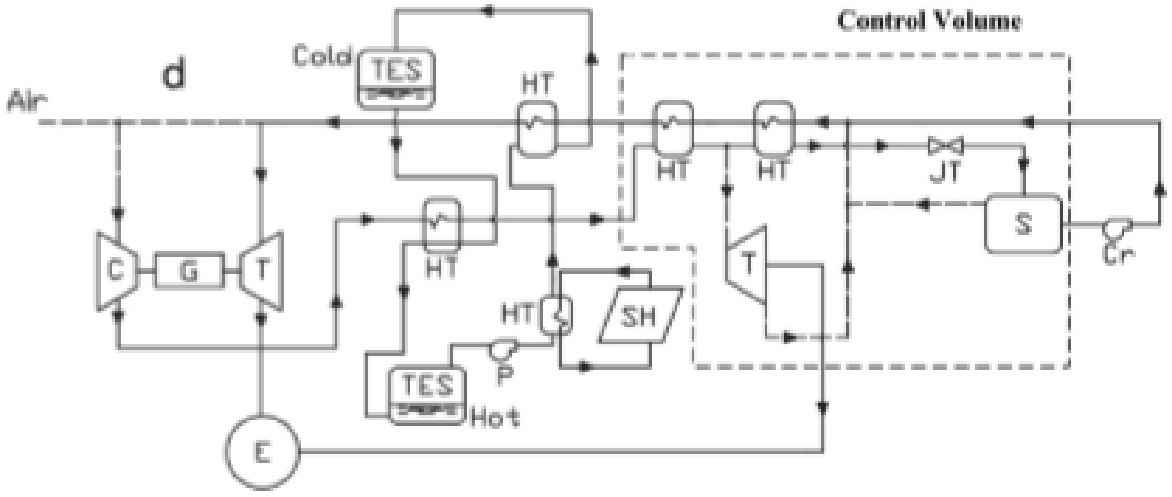

Figure 2-6:Integration of hot and cold energy storage in CES system with a thermal solar system

Guzzi evaluated the performances of a stand-alone LAES system (40), based on the same layout introduced before, using another type of thermal oil (Essotherm 650) for the heat recovery circuit and a mix of propane and methanol for the cold section: their high heat capacity reduces the storage volume required. The power section is composed by three stage turbines with inter-heating. The plant layout is very similar with respect to Abdo model evaluated before. In this

work is evaluated the relation between the compression ratio in the liquefaction cycle and the performances of the system: higher ratio means more liquid yield and lower slope of the curve corresponding to the cold air in the heat exchanger, lowering the pinch point and increasing the efficiency. With the best value of compression ratio (179.2), the round-trip efficiency found is 54.4%.

One of the most recent study in cryogenic energy storage application was performed by Sciacovelli (22), that proved an increasing of the LAES system overall efficiency of almost 50% due to the storage of cold thermal energy through packed beds. Another important point is represented by the importance of the dynamics of the modelling, that cause a 25% increase of the energy expenditure on liquefaction cycle. Also, in this case with the optimal condition of a charging pressure of 185 bar the round-trip efficiency reaches the value of 50%.

Chronologically, the last innovation for CES technology is Cryohub (41): it is a European project funded by the European Union's Horizon 2020 Research and Innovation Programme, with the collaboration of 14 industrial and academical partners. The innovative idea of Fikiin is the coupling of cryogenic energy storage technology with refrigerated warehouses, with the purpose to exploit their ideal profile: they are large electricity consumers and they need consistent quantity of cold. Furthermore, industrial environments produce a big amount of heat waste and are often available for installation of renewable sources, like photovoltaic panels or wind turbine. The *figure 2.7* shows how the high grade cold energy, contained in liquid cryogens, flows to the refrigerated facilities and evaporates, before expanding in turbine. Claude expander is the most efficient choice for the liquefaction process in this plant. The hot storage inputs are represented by the compressor heat and from the industrial waste heat, while a rocks packed bed is adopted for the cold storage.

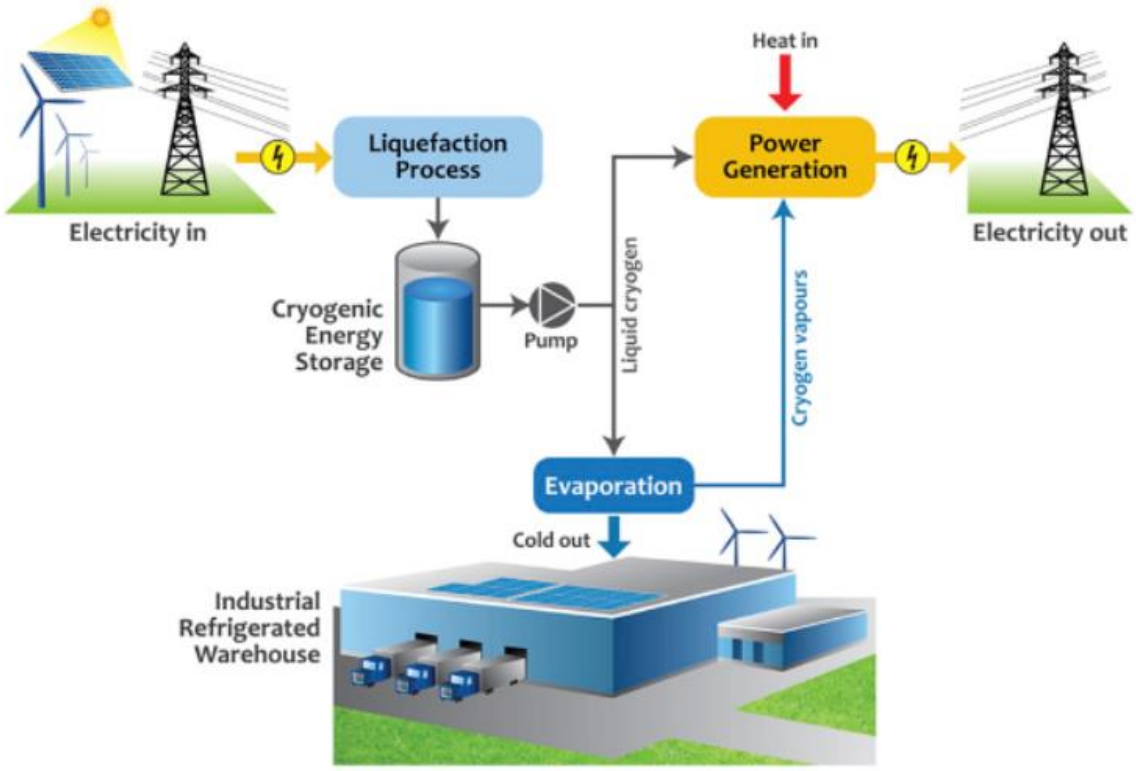

Figure 2-7:Cryohub concept configuration

This concept points out the synergistic use of CES and RES: the overall efficiency of the plant is enhanced, and some preliminary study estimates an annual reduction of 9 Mt of CO_2, if this configuration were applied at almost 10% of large refrigerated facilities in EU.

Name of the system/ designer	Technology and Innovations	Round-trip efficiency (%)	Demonstrator/ Pilot plant
Mitsubishi	Rankine and Brayton combined	77*	X
Hitachi (Wakana)	Brayton cycle/ LNG pre-cooling of air and liquid air storage inside regenerator	N.A.	X
Ameel	Rankine cycle and Linde liquefier	43	
Highview Power (Morgan)	Rankine cycle and Claude liquefier/Cold storage	60	X
Abdo	Rankine cycle and Claude liquefier/ Hot and cold storage and solar system	63	
Guizzi	Rankine cycle and Claude liquefier/standalone plant	55	
Sciacovelli	Rankine cycle and Claude liquefier plus JT valve/ Cold energy storage with quartzite packed bed	50	
Cryohub (Fikiin)	Rankine cycle with modified Claude cycle/ refrigerated warehouses	N.A.	

Table 2-1:Cryogenic energy storage technology comparison

*liquefaction efficiency not accounted

2.4 Cold Energy Storage technologies

From the previous study, it is possible to underline the key role of the high grade cold storage in a cryogenic energy storage system, to improve significantly the round-trip efficiency. This necessity emerges from the discrepancy of high demand of cold during the liquefaction process and the high production during the air evaporation. Among the solutions regarding cold energy storage described in the literature, the most considered are represented by packed bed of solid mineral material, as gravel and sand.

In the study presented by Krawczyk (42), is proposed another type of storage, based on active sensible heat storage. A different liquid fluid works as heat or cold carrier, charging a cold energy storage in the discharge phase of the system and charging a hot energy storage in the charge phase. Instead of a single fluid, two different liquids are selected, to obtain an efficient recovery at very different temperature: the problem is to find two liquids without a phase change temperature in the range of their work: the only substance available are hydrocarbons. The *figure 2.8* shows the roles of the storage in the system layout: when the power is required, there are two different warm heat carriers that transfer heat to the liquid air, the first is cooled down by -60°C to 185°C and the second from 25°C to -60°C. In this way the liquid air is evaporated and superheated, before expanding in a gas turbine.

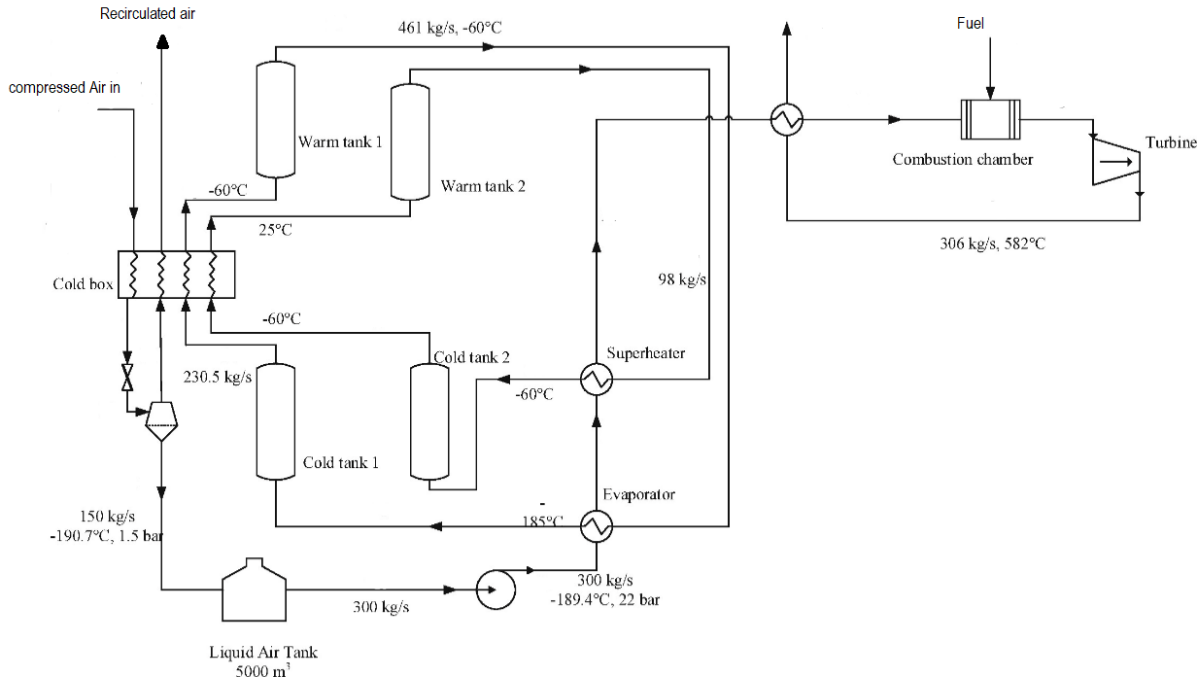

Figure 2-8:System layout

The fluids selected are liquid propane for the first stage and liquid methanol for the second one and their properties are shown in the *table 2.2*. With this configuration the round-trip efficiency of the plant is around 55.2%, considering also the chemical exergy of the fuel in the combustion chamber.

Substances	Boiling Point (°C)	Freezing Point (°C)
Liquid propane (R290)	-42	-189
Liquid methanol	65	-97.6

Table 2-2: Properties of selected heat transfer substances

The study performed by Huttermann (43) investigated and the most efficient materials for a packed bed cold storage (PBCS), that consists on a single cylinder with a packed bed of storage material. In this work, he considers the influence of the solid heat capacity for the estimation of the efficiency and identifies the importance of the outlet temperature during the discharge process and the pressure losses along the bed. The thermodynamic analysis shows an increasing of the efficiency at decreasing volumetric heat capacity and when its variation is small with the temperature (the results show a linear dependence). The material with the best performance (47.53%) is lead, with an averaged volumetric heat capacity $c_{vol,ave}$ =1.42 MJ/m^{3}K and a ratio between minimum and maximum heat capacity π = 0.93 (in the investigated temperature range). Unfortunately, the lead is dangerous and very expensive: the best trade-off is represented by quartz or other rock material, with a PBCS efficiency of 34.34% (43) or by some plastic material: polypropylene and hd-polyehtylene. They could reach higher efficiency (39.61% and 38.4%) and due to their small density, they could ensure low weight for the system and economic advantages.

Another analysis based on the packed bed cold storage technology was developed by Morgan (44). He concluded that, for the material selection, the most important issues are the resistance at cryogenic temperature, the tolerance to thermal cycling and the cost. It was developed an important issue, in contrast with the Huttermann's analysis: for the reduction of the storage size, high density and high specific heat capacity are desired. Subsequently, it is also necessary a good trade-off for the evaluation of the thermal conductivity: high value is necessary to avoid thermal gradients across the particles of the bed and low value is desirable to minimize the conductive losses and the self-discharged of the system. After these consideration, the authors' choice was a low thermal conductivity material, with a small particle size, to reduce as much as possible the thermal gradient within the particles: gravel or glass are the more feasible, while metallic materials were discarded.

The function of the external shell of the storage are the structural support, the insulation for the thermal losses and the pressure containment. The authors made some consideration about this point, underlining the mechanical problem due to high pressure of the working fluid inside the container (190 bar during discharge) (44). In this case the thickness of the shield is supposed to be very large and unfeasible: a solution proposed that high pressure working fluid passed through pipes embedded in the packed bed material. This solution appears immediately inefficient and another approach suggests using a secondary working fluid with a lower pressure, to avoid pressure restrictions inside the storage. This method requires an additional heat exchanger, followed by additional irreversibilities, that could be minimized optimizing the heat exchanger design.

The most performant shape of the cold storage was investigated: assuming L the store length and D the diameter, for lower pressure losses it is more suitable a short and wide configuration (low L/D ratio), while for low thermal losses is better a high L/D ratio. To find the best trade-off, it is important to consider the behaviour of the storage: this device works when power is needed and when electricity production is in excess, so thermal energy transfer rate to and from the store is different during various cycles, generating fluctuations in the mass flow rate. Referring to the *figure 2.9* , the authors propose a "multi-cells storage concept" (44), where individual storage cells work in parallel, in series or isolates, to reach the perfect configuration: when the fluid flows is high, it is suggested to arrange the cells in parallel to minimize the pressure drop, while the series configuration is more productive when the flow is low and the thermal losses have to be minimizing. This configuration guarantees an improvement of 4.8%.

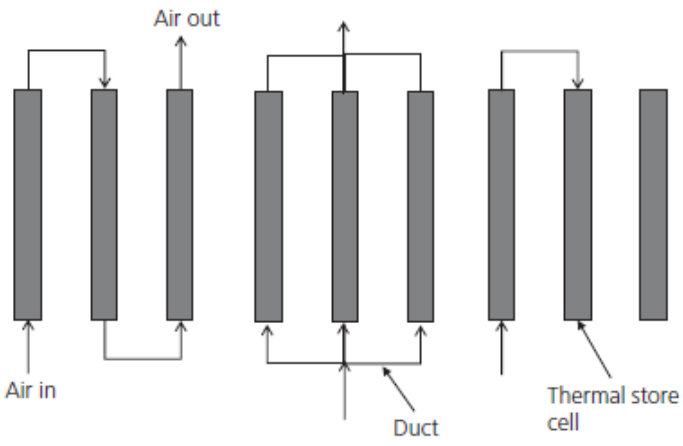

Figure 2.9: Multi-cell storage concept: Series, parallel and isolated configuration

3 Parametric study of Cold Energy Storage efficiency

In the previous chapter, it appears clear the importance of the cold energy storage, to solve the problem of asynchrony between the cold energy demand in liquefaction process in charge phase and the high grade cold energy supply in the discharge phase of the plant. There were reported a lot of different configuration for the choice of the material or for the store design.

In this chapter will be reported a parametrical analysis of the cold energy storage, in terms of thermodynamic and layout aspects with a Microsoft Excel model, performing several simulations to obtain the most efficient configuration and evaluating the different causes for the main losses in terms of performances.

3.1 Model definition

In order to define the model of the system investigated, it is necessary to start with the basic assumption: the cold energy storage is composed by a stainless steel external shell, with a packed bed quartzite as heat storage medium (HSM). The design of the shell and the configuration of the packed bed are parameters evaluated into the analysis. The heat transfer fluid (HTF) adopted in this study is pure nitrogen (N_2): to avoid the problem about the high pressure in the cold storage discussed in the *chapter 2.4*, there is an additional heat exchanger (HX) that couples the liquid air pumped at high pressure and the nitrogen at low pressure.

The fluid thermos-physical and thermodynamic properties are obtained by the software REFPROP 9.1 (NIST, 2017) ®.

3.1.1 Assumptions list

The proposed model is performed with the assumption of stationary condition, fixing some parameters, according to the preliminary Cryohub project (45)

Operational assumptions:

- Charge and discharge time are fixed at 2,5 hours

- The pressure drop in the HX is 0.5% of the pressure in nitrogen side
- The pressure of Liquid Air storage is 15 bar
- The mass flow of the liquid air is 0.4 kg/s
- The max. temperature of the Nitrogen (HTF) is -48°C and the min. is -170.8°C
- The temperature of Liquid air at the HX inlet and outlet are corresponding -172.8 and -50°C

Layout assumptions:

- Insulation thickness is 0.25 m
- Cold storage internal diameter is 1.68 m.

Fixed external conditions:

- Ambient temperature is 15°C
- External heat transfer coefficient h is 20 W/m^2K.

Properties of Quartzite:

- Density $\rho = 1800$ kg/m^3
- Thermal conductivity k = 2.5 W/mK.

The approach used for the evaluation of the efficiency of the system started from the available energy from the cold flux transferred from the liquid air evaporation to the nitrogen in the HX. In the *figure 3.1* it is possible to evaluate the role of the heat exchanger in the discharge phase of the system: the liquid air is evaporated and heated up by a warm flux of nitrogen, that charges the storage with high grade cold. The liquid air mass flow is supposed to be 0.4 m/s for a discharge time of 2.5 hours, for a total mass of 3600 kg.

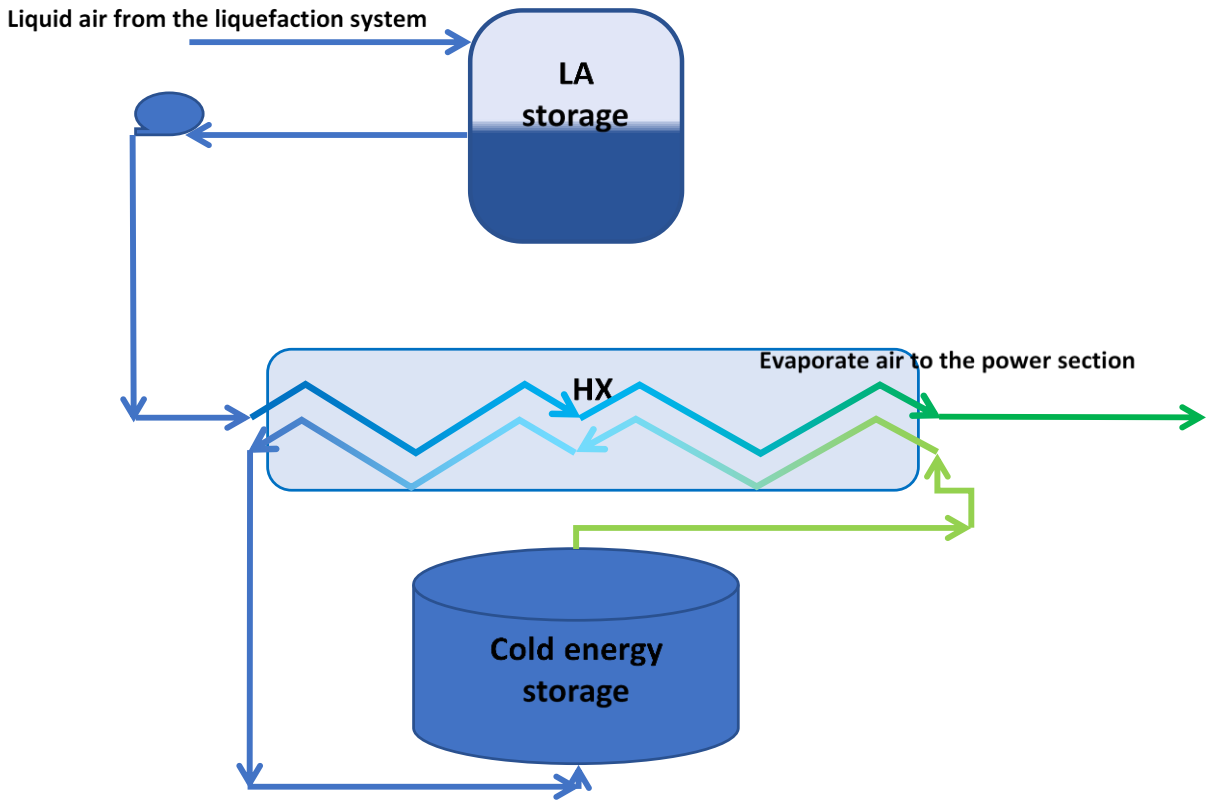

Figure 3-1:System layout in discharge phase

The liquid air input temperature in HX is supposed to be -173.68 °C, that represents the saturation temperature at the pressure of 15 bar for the air and at the output reaches the temperature of -50°C. The enthalpy change corresponding is 297.88 kJ/kg, obtained with REFPROP 9.1 (NIST, 2017) ®.

The energy stored in the Cold energy storage, that is equal to the energy transferred from the liquid air to the nitrogen, is obtained with:

$$E_{stored} = m_{liq.air} \cdot \Delta h_{liq.air} = 297.9\ kWh \qquad (3.1)$$

Where:

E_{stored} is the energy that could be stored in the vessel (kWh)

$m_{liq.air}$ is the total mass of liquid air that evaporate for each cycle (kg)

$\Delta h_{liq.air}$ is the difference of enthalpy of the liquid air between the HX inlet and outlet (kJ/kg)

Considering the nitrogen side, with the minimum and maximum temperature supposition described above, it is possible to estimate the mass flow needed:

$$\dot{m}_{nitrogen} = {}^{E_{stored}}\Big/_{\Delta h_{nitrogen} \cdot t_{discharge}} = 0.9065\ \frac{kg}{s} \qquad (3.2)$$

Where:

$\dot{m}_{nitrogen}$ is the nitrogen mass flow that pass through the HX (kg/s)

E_{stored} is the energy that could be stored in the vessel (kWh)

$t_{discharge}$ is the discharge time of each cycle (h)

$\Delta h_{nitrogen}$ is the difference of enthalpy of the nitrogen between the HX inlet and outlet (kJ/kg)

The average heat capacity (C_p), of the quartzite is obtained by Cryogenic Material Properties Database (46), in function of the temperature with a sixth-order polynomial approximation.

Knowing the energy stored in the material, the interval of storage temperature and the C_p, it is possible to evaluate the mass of the HSM needed.

$$m_{quartzite} = {}^{E_{stored}}\Big/_{\Delta T_{max-min,q} \cdot c_{p,q}} = 450.97\ kg \qquad (3.3)$$

Where:

$m_{quartzite}$ is the total mass of HSM needed in the Cold Energy Storage (kg)

E_{stored} is the energy that could be stored in the vessel (kWh)

$\Delta T_{max-min,q}$ is the maximum temperature difference of the quartzite (K)

$c_{p,q}$ is the average heat capacity of the quartzite (kJ/kgK)

Considering the assumption value of the quartzite density value and the cold storage internal diameter, it is easy to establish the cross-sectional area, the total volume and the corresponding height of the packed bed:

$$A_{storage,section} = 2.14\ m^2$$

$$V_{packed\ bed} = 10.75\ m^3$$

$$h_{packed\ bed} = 5.03\ m$$

3.1.2 Heat transfer model adopted

The thermodynamic characteristics of the heat transfer fluid (HTF) at the inlet of the control volume, that corresponds to the cold storage, are generally calculated at the average between the inlet and outlet conditions, considering a linear approximation. In the discharge phase, the inlet temperature of the HTF is -170.8 °C and at the outlet is -48°C. The maximum temperature of the HSM is -46°C and the minimum temperature estimated is -169°C, considering a non-ideal heat exchanger, with the assumption of 2°C of difference between cold HTF temperature and the warm HSM.

From the software REFPROP 9.1 (NIST, 2017) ® are evaluated the inlet and the outlet parameters of the HTF such as density ρ, viscosity μ, heat capacity c_p and thermal conductivity k. The following step concerns the calculations of the most important indexes to evaluate the heat transfer between the fluid and the medium:

- HTF Speed:

$$u = \frac{\dot{m}_{HTF}}{\rho_{HTF} \cdot A_{Storage,section}} \left[\frac{m}{s}\right] \quad (3.4)$$

Where:

u is the HTF speed (m/s)

$\dot{m}_{HTF}$ is the HTF mass flow rate (kg/s)

ρ_{HTF} is the HTF density (kg/m^3)

$A_{Storage,section}$ is the section of the Cold Energy Storage (m^2)

- HTF Prandtl Number:

$$Pr = \frac{\mu_{HTF} \cdot c_{p,HTF}}{k_{HTF}} \ [-] \tag{3.5}$$

Where:

Pr is the Prandtl number associated at the HTF (-)

μ_{HTF} is the HTF viscosity (Pa·s)

$c_{p,HTF}$ is the HTF heat capacity (kJ/kgK)

k_{HTF} is the HTF thermal conductivity (W/mK)

- HTF Reynolds Number:

$$Re = \frac{\rho_{HTF} \cdot u \cdot d_{ave,q}}{\mu_{HTF}} \ [-] \tag{3.6}$$

Where:

Re is the Reynolds number associated at the HTF (-)

μ_{HTF} is the HTF viscosity (Pa·s)

ρ_{HTF} is the HTF density (kg/m^3)

u is the HTF speed (m/s)

$d_{ave,q}$ is the average diameter of the quartzite (m)

To evaluate the heat transfer coefficient h between the HTF and the HSM, the Nusselt number is obtained from the Ranz and Marshall correlation, for flow around stationary particles (47):

$$Nu = \frac{h \cdot d_{ave,q}}{k_{HTF}} = 2 + 0.6 \cdot Re^{\frac{1}{2}} \cdot Pr^{\frac{1}{3}} \ [-] \tag{3.7}$$

Where:

Re is the Reynolds number associated at the HTF (-)

h is the heat transfer coefficient (W/m^{2}K)

Nu is the Nusselt number associated at the HTF (-)

k_{HTF} is the HTF thermal conductivity (W/mK)

Pr is the Prandtl number associated at the HTF (-)

$d_{ave,q}$ is the average diameter of the quartzite (m)

This correlation allows to estimate the Biot number, a non-dimensional number defined as the ratio between the convective and conductive heat transfer mechanism:

$$Bi = \frac{h * L}{k_{HSM}} \tag{3.8}$$

Where:

L is characteristic length, defined as the ratio between particle volume and surface (m)

h is the heat transfer coefficient (W/m2K)

Bi is the Biot number (-)

k_{HSM} is the HSM thermal conductivity (W/mK)

Low Biot number (<0.1) means uniform temperature inside the particles and simpler evaluation of the model: conduction inside the body is much faster than the heat convection on his surface.

3.1.3 Definition of the model input variables

In this study were performed numerous calculations to value the effect, in terms of cold energy storage efficiency, of varying input parameters. They could be both of thermodynamic or related to the store design. Previous studies achieved in Cryohub project by the university involved, determined a starting point for this analysis, fixing some important physical, operational and structural references, discussed in the *section 3.1.1*.

The input variable considered in this study are the inlet pressure of the HTF in the storage, the diameter of the HSM material and its configuration (layers in series), the storage external design expressed in terms of L/D ratio, the thermal conductivity of the insulation and the Pressure drop factor (*X*). The last parameter is an operational variable and depends from the designer choice: choosing the pressure drop factor equal 0 means to adopt a storage material perfectly shaped, while a value equal 1 means to use the quartzite gravel. The consequences of using a HSM non-

perfectly spherical, correspond to a value adopted between 0 and 1. The pressure drop factor is used in the pressure drop estimation in the *equation 3.29.*

Input variable parameters	**Symbol**	**Type**	**Range**
HTF pressure inlet	*P* (bar)	Thermodynamic	1 to 4
Average quartzite diameter	*D* (mm)	Design	2 to 7
Storage slenderness (L/D ratio)	*SL* (-)	Design	1 to 4
# HSM layers in series	# (-)	Design	1 to 4
Insultation Thermal conductivity	*k* (W/mK)	Operational	0.01 to 0.1
Pressure drop factor	*X* (-)	Operational	0 to 1

Table 3-1:Input variable parameters

The effect on the total efficiency for the operational input parameters appears obvious: the best scenario is related with the smallest value proposed for the Insulation thermal conductivity, which presupposes the higher thermal resistance and the lowest thermal leaks. The same consideration is valid for the Pressure drop factor: choosing a *X*=0 means a perfect sphericity, with lower porosity and lower pressure losses. On the contrary, the other parameters in the first approximation could have a best efficient point inside the proposed range.

3.2 Analytical evaluation of the Cold Energy Storage Efficiency

The Cold energy storage efficiency is defined by:

$$\eta_{Cold\ Energy\ Storage} = \frac{E_{stored} - E_{losses}}{E_{stored}} \cdot \epsilon_{Cold\ Energy\ Quality} \qquad (3.9)$$

Where:

$\eta_{Cold\ Energy\ Storage}$ is the round-trip efficiency of the Cold Energy Storage (-)

$\epsilon_{Cold\ Energy\ Quality}$ is the efficiency of the heat transfer from the liquid air to the HSM, through the nitrogen (-)

E_{stored} is the energy stored in the Cold Energy Storage (kWh)

E_{losses} is the total amount of energy lost during the storage (kWh)

The efficiency of the cold energy quality is defined as:

$$\epsilon_{Cold\ Energy\ Quality} = \left(\frac{T_{min,HSM} - T_{max,HTF}}{T_{min,liq.air} - T_{max,liq.air}}\right)^2 \quad (3.10)$$

Where:

$\epsilon_{Cold\ Energy\ Quality}$ is the efficiency of the heat transfer from the liquid air to the HSM, through the nitrogen (-)

$T_{min,HSM}$ is the minimum temperature of the quartzite during the operation (K)

$T_{max,HTF}$ is the maximum temperature of the nitrogen during the operation (K)

$T_{min,liq.air}$ is the minimum temperature of the liquid air during the operation (K)

$T_{max,liq.air}$ is the maximum temperature of the liquid air during the operation (K)

The E_{losses} represents all the terms of losses in the cold energy storage system: the main contributions are due to the pressure losses of the nitrogen across the storage (energy consumed to supply fans), to the heat leaks through the insulation layers and to the thermocline thickness:

$$E_{losses} = E_{fan} + E_{heat\ leaks} + E_{thermocline} \quad (3.11)$$

Where:

E_{losses} is the total amount of energy lost during the storage (kWh)

E_{fan} is the energy needed to feed the fan (kWh)

$E_{heat\ leaks}$ is the energy lost for the heat leaks (kWh)

$E_{thermocline}$ is the energy dissipated in the thermocline region (kWh)

In the following sub-sections, all the terms relative to the system inefficiency will be investigated. The efficiency of the system is evaluated in terms of energy, considering the operation time of the system of 1 day. For each term, is therefore applied a peculiar assumption: it is considered the sum of discharge and charge time (5h) for the consumption of the fan and 24h for the heat leaks and the energy losses due to the presence of the thermocline.

3.2.1 Fan Energy consumption

This parameter is mainly influenced by the design of the storage and by the diameter of the HSM material. A larger and short configuration, with low slenderness (L/D ratio), means lower pressure losses, due to the shorter distance covered from the heat transfer fluid (HTF) at the same volume of storage material. They are linearly dependent with the HSM thickness and could be reduced using different layers in series connected by some valves, that allow to bypass the layers that don't need to be charged or discharged in that period. A larger diameter of the storage material means lower pressure drop and consequently lower fan energy consumption.

The expression of the fan Energy consumption is expressed by:

$$E_{fan} = P_{fan} \cdot 2 \cdot \Delta t_{discharge} \tag{3.12}$$

Where:

E_{fan} is the energy needed to feed the fan (kWh)

P_{fan} is the fan power (W)

$\Delta t_{discharge}$ is the discharge time of the cryogenic cycle (s)

Where the multiplicator factor 2 accounts both the charge and discharge time, that for hypothesis are the same.

The HTF in the cold energy storage circuit flows in a closed loop, through a heat exchanger and the cold storage. To compensate all the pressure losses in this path, an electric fan is needed. Its power is expressed as:

$$P_{fan} = \dot{m} * Cp * T_{in} * \left(\left(\frac{P_{out}}{P_{in}} \right)^{\frac{\gamma-1}{\gamma}} - 1 \right) \Big/ \eta \tag{3.13}$$

Where:

Cp is the heat capacity at constant pressure (J/kgK)

Cv is the heat capacity at constant volume (J/kgK)

$\gamma = \frac{Cp}{Cv}$ is the gas constant (-)

T_{in} is the gas inlet temperature (K)

$\dot{m}$ is the mass flowrate (kg/s)

P_{in} is the gas total inlet pressure (Pa)

P_{out} is the gas total outlet pressure (Pa)

η is the fan Efficiency (-)

This work, expressed in Watt, is proportional with the mass flowrate of the nitrogen, its heat capacity and it is strictly dependent on the overall pressure drop, accounted on the ratio $\left(\frac{P_{out}}{P_{in}}\right)$, that is strictly greater than 1.

The pressure at the outlet represents the pressure drop across the cold storage, the pressure losses distributed in the heat exchanger and along the pipes:

$$p_{out} = p_{in} + \Delta p_{tot} = p_{in} + \Delta p_{storage} + \Delta p_{HX} + \Delta p_{pipes} \tag{3.14}$$

Where:

$$\Delta p_{storage} = \frac{{}^{\Delta P}/_{l} \cdot h_{packed\ bed}}{\#_{HSM\ series\ layers}} \text{ (Pa)}$$

Δp_{HX} corresponds at 0.5% of p_{in} (Pa)

Δp_{pipes} is evaluated considering the distributed pressure losses along the pipes, considering the total length, the diameter, the HTF speed and the friction factor

To evaluate the pressure drops in the cold storage, in the following part of this section are presented three different approach, one theoretical, one experimental and the last is a combination of the previous ones.

3.2.1.1 Theoretical approach

The first is provided by a correlation from the literature that determines the pressure drop across a packed bed of spheres, from the extension of Ergun equation for fluidized beds discussed by Akgiray and Saatçı in 2001:

$$\Delta P_{ERGUN}/_{l} = 150 \cdot \frac{\left(1-\varepsilon_{part}\right)^2}{\varepsilon_{part}^3} \cdot \frac{\mu}{d_{part}^2} \cdot u + 1.75 \cdot \frac{1-\varepsilon_{part}}{\varepsilon_{part}^3} \cdot \frac{\rho}{d_{part}} \cdot u^2 \qquad (3.15)$$

Where:

$\Delta P_{ERGUN}/_{l}$ is calculated pressure drops by Ergun's correlation (Pa/m)

l is the packed bed length (m)

ε_{part} is the porosity of the particle (-)

μ is the fluid dynamic viscosity (Pa·s)

ρ is the fluid density (kg/m^3)

d_{part} is the particle diameter (m)

u is the superficial fluid speed (m/s)

This function contains some parameters referred to geometrical characteristics of the material (d, ε) and some related to thermodynamic properties (μ, ρ). This equation is valid for both laminar and turbulent regimes: the first term, linearly proportional with the fluid speed dominates in laminar flow conditions, while the second term, related with the square of the fluid speed, is predominant with a turbulent behaviour (48).

This equation is valid with the ideal assumption of perfectly shaped packed beds, so for the real evaluation of the pressure drop, the second approach consists on the post-processing of the pressure losses experimentally obtained by a study performed by IRSTEA, for keep into account the imperfect shape of the material proposed in this study.

In the next part of this chapter, it was created an analytical model to compute the real value of the pressure drops across the spheres packed bed in function of the fluid speed and in function of particle diameter and porosity, to recreate a law like Ergun's, but based on the experimental value found.

3.2.1.2 Experimental approach

An experimental study performed by IRSTEA, the French National Research Institute of Science and Technology for Environment and Agriculture an accurate study based on experimental data provided for three different size of quartzite samples, each characterized by a porosity value, shown in the table 3.2.

Type/denomination	**Average diameter (*mm*)**	**Porosity (-)**
Small size	2.2	0.39
Medium size	4.7	0.48
Large size	6.5	0.39

Table 3-2:Characteristics of quartzite samples investigated

The same value of porosity for the small and the large size are due to the high heterogeneity of the biggest particles, reason why in this case smaller particles could fill the voids.

These experiments were performed in ambient conditions (p=1 bar and T=25°C) and the HTF used is air mixture.

In the figure 3.2, 3.3 and 3.4 are presented the comparison between the experimental value of pressure losses obtained with the experiment and the value obtained using the Ergun equation for each size.

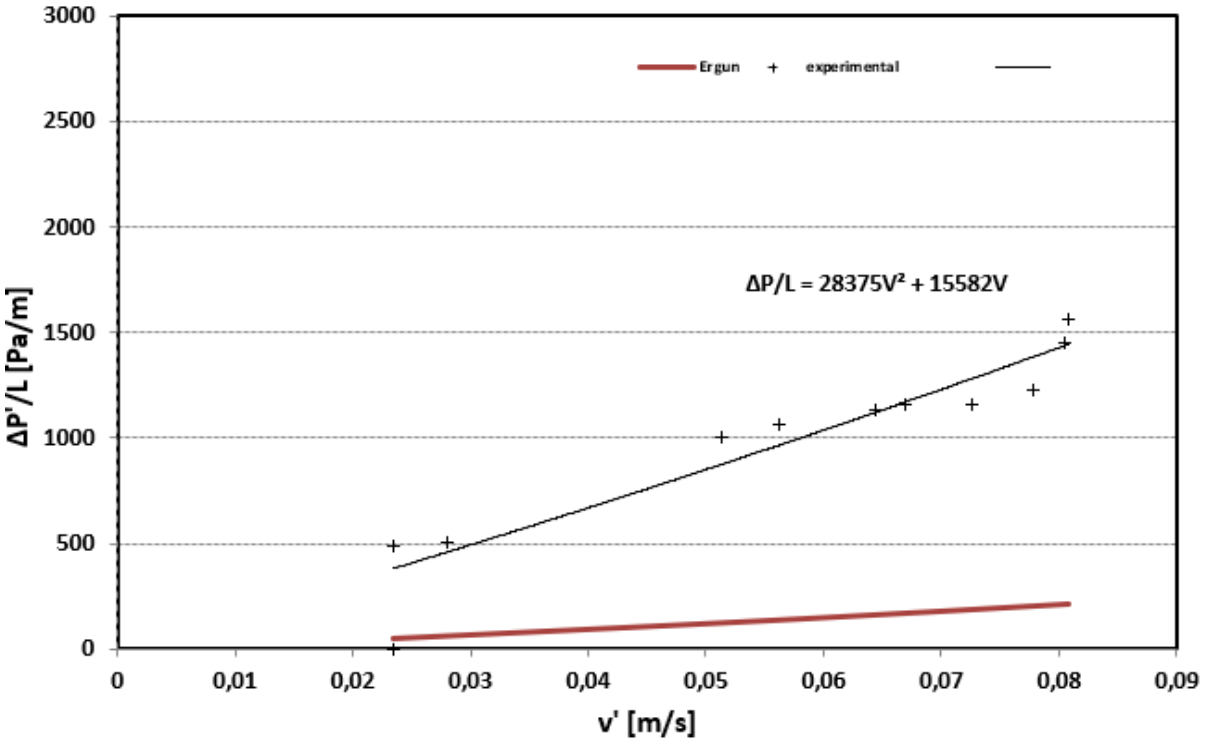

Figure 3-2:Pressure drop Small size

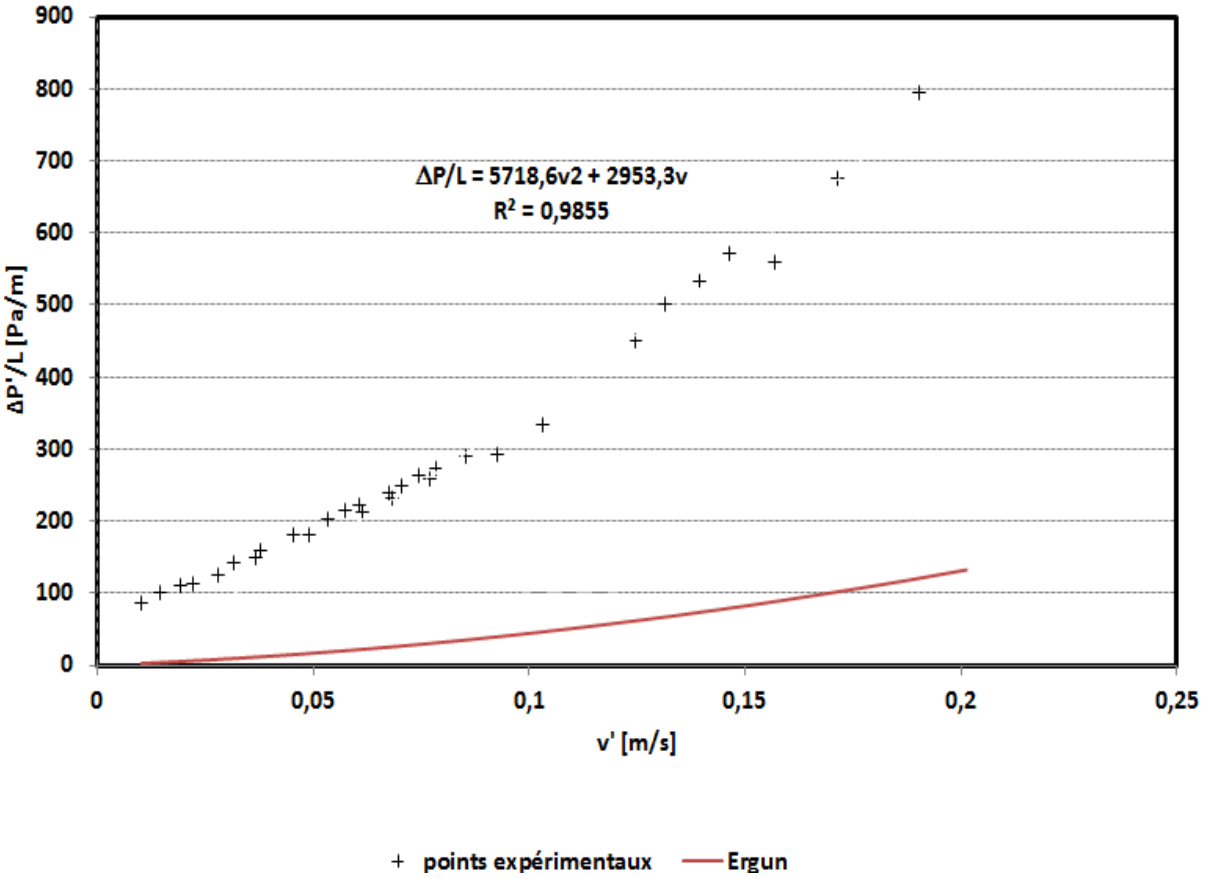

Figure 3-3:Pressure drop Medium size

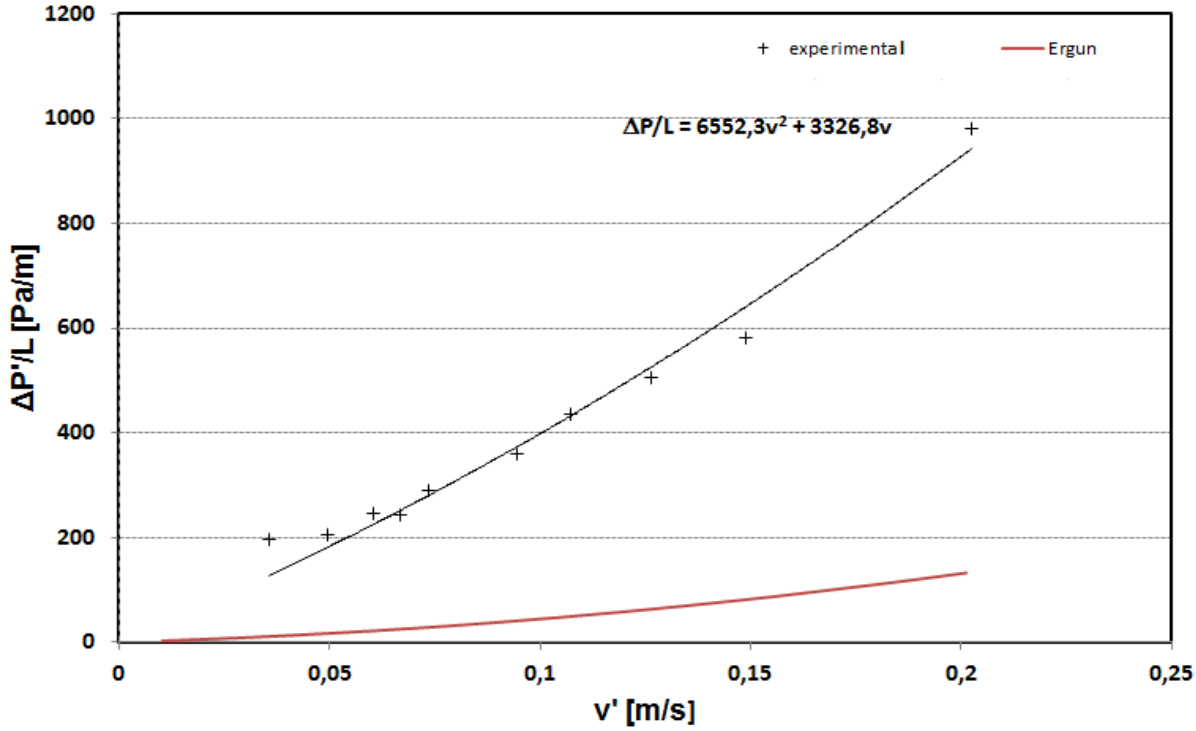

Figure 3-4:Pressure drop Large size

The results obtained are expressed as two empirical coefficients, one is linear function of HTF speed u and the other is related to u^2.

- Small size gravel (2.2 mm):

$$\frac{\Delta P_{exp}}{L}(u) = \ 15582 \cdot u + 28375 \cdot u^2 \quad \left[{}^{Pa}/_{m}\right] \tag{3.16}$$

- Medium size gravel (4.7 mm):

$$\frac{\Delta P_{exp}}{L}(u) = \ 2953.3 \cdot u + 5718.6 \cdot u^2 \quad \left[{}^{Pa}/_{m}\right] \tag{3.17}$$

- Large size gravel (6.5 mm):

$$\frac{\Delta P_{exp}}{L}(u) = \ 3326.8 \cdot u + 6552.3 \cdot u^2 \quad \left[{}^{Pa}/_{m}\right] \tag{3.18}$$

To perform a dynamic simulation, it is necessary to find a unique suitable law for the expression of pressure losses, function of both gravel diameter and porosity.

All previous functions are represented in the form:

$$\frac{\Delta P_{exp}}{L}(u) = \ C_1 \cdot u + C_2 \cdot u^2 \quad \left[{}^{Pa}/_{m}\right] \tag{3.19}$$

It appears immediately no sufficient to express the pressure drops in function of only HTF speed, because the purpose of this study is to find a way to express the pressure drops also in function of particle diameter and porosity.

It was performed an accurate analysis of the relationship between experimental results and Ergun's law, trying to uncouple the parameters in function of thermodynamic conditions (μ, ρ_f) by those in function of only geometrical condition (d, ϵ), always keeping their respective connection to u or u^2.

Remembering the Ergun expression for pressure drops, it was decided to create a set of fitting variables:

$$Z_1 = 150 \cdot \mu$$

$$Z_2 = 1.75 \cdot \rho_f$$

$$X_1 = \frac{1}{d^2} \cdot \frac{(1-\epsilon)^2}{\epsilon^3}$$

$$X_2 = \frac{1}{d} \cdot \frac{(1-\epsilon)}{\epsilon^3}$$

Where the parameters are the same ones that appear on Ergun equation.

Considering the thermos-physical conditions of the experiment, as mentioned above, the corresponding values of dynamic viscosity μ and density ρ for the air are:

$$\mu = 1{,}78E-05 \ \ (Pa \cdot s)$$

$$\rho = 1{,}13E+00 \ \ (kg/m^3)$$

The resulting values relatives to the HTF thermodynamic conditions could be fixed:

$$Z_1 = 2{,}67\,E-03 \ (Pa \cdot s)$$

$$Z_2 = 1{,}98\,E+00 \ \ (kg/m^3)$$

The introduced parameters X_1 and X_2 express the relationship between each gravel average size and its relative porosity and to make this analysis more fluent, two main constants are declared:

$$Y_1 = X_1 \cdot Z_1$$

$$Y_2 = X_2 \cdot Z_2$$

	Diameter [mm]	Porosity [-]	X_1	X_2	Y_1	Y_2
Small size	2,2	0,39	1296046,2	4674,3	3460,7	9256,0
Medium size	4,7	0,48	283968,5	1000,4	758,3	1981,0
Large size	6,5	0,39	148470,1	1582,1	396,4	3132,8

Table 3-3:Parameter for each quartzite size

Now, the expression for pressure losses became:

$$\frac{\Delta P_{exp}}{L}(u) = Y_1 \cdot c_1 \cdot u + Y_2 \cdot c_2 \cdot u^2 \quad \left[{}^{Pa}/_{m}\right] \tag{3.20}$$

and to adapt the expression to the *equation 3.19,* there could be assumed the constant

$$c_1 = {}^{C_1}/_{Y_1}$$

$$c_2 = {}^{C_2}/_{Y_2}$$

In this way, they are obtained a set of parameters of c_1 and c_2 for each gravel diameter value.

Now the total pressure drops were divided in two different members, to reach a more accurate study and to divide the term function of *u* and u^2:

$$\frac{\Delta P_{exp\_1}}{L}(u, Y_1) = Y_1 \cdot c_1 \cdot u \tag{3.21}$$

$$\frac{\Delta P_{exp\_2}}{L}(u, Y_2) = Y_2 \cdot c_2 \cdot u^2 \tag{3.22}$$

Afterwards it was performed, with an Excel regression function (LINEST), a determination of some empirical coefficients to create an exclusive relationship between the pressure drop values of both the members described in the equations 3.21 and 3.22 with the Y variable, keeping constant the HTF speed in each interval, in a range from 0.02 m/s to 0.5 m/s.

There were obtained two analytical functions on this form for a set of HTF speed:

$$\frac{\Delta P_{exp\_1}}{L}(Y) = a_0 + a_1 \cdot Y_1 + a_2 \cdot {Y_1}^2 \tag{3.23}$$

$$\frac{\Delta P_{exp\_2}}{L}(Y) = b_0 + b_1 \cdot Y_2 + b_2 \cdot {Y_2}^2 \tag{3.24}$$

$u\ [m/s]$	a_2	a_1	a_0
0,02	0,0000	-0,0636	85,9151
0,052	0,0001	-0,1655	223,3794
0,084	0,0002	-0,2673	360,8436
0,116	0,0002	-0,3691	498,3078
0,148	0,0003	-0,4710	635,7720
0,18	0,0003	-0,5728	773,2363
0,212	0,0004	-0,6746	910,7005
0,244	0,0005	-0,7765	1048,1647
0,276	0,0005	-0,8783	1185,6289
0,308	0,0006	-0,9801	1323,0932
0,34	0,0006	-1,0820	1460,5574
0,372	0,0007	-1,1838	1598,0216
0,404	0,0008	-1,2856	1735,4858
0,436	0,0008	-1,3875	1872,9501
0,468	0,0009	-1,4893	2010,4143
0,5	0,0009	-1,5911	2147,8785

Table 3-4:Empirical values of the constant a0, a1, a2 for a set of HTF speed

To analyse better the evolution of these coefficients with the increasing of the speed *u*, their trends are displayed in the *figures 3.5-3.10*:

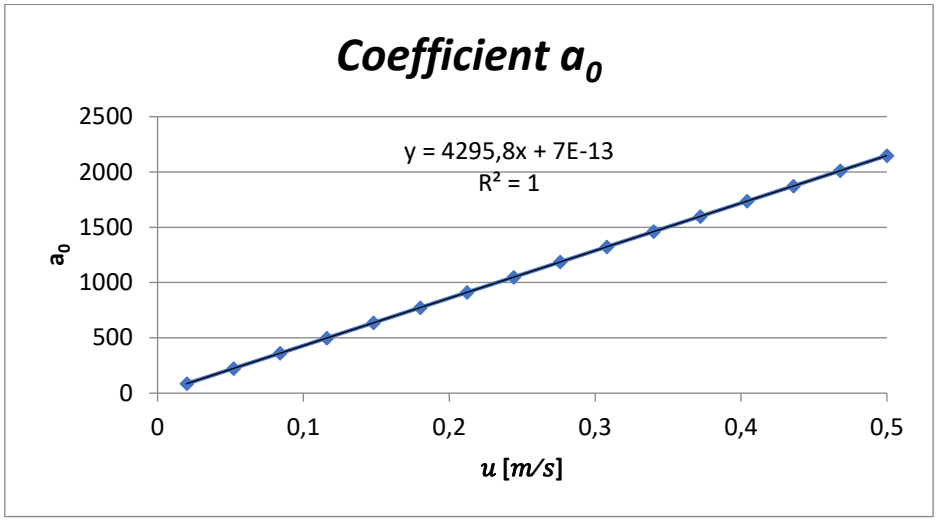

Figure 3-5:Coefficient a0 in function of HTF speed

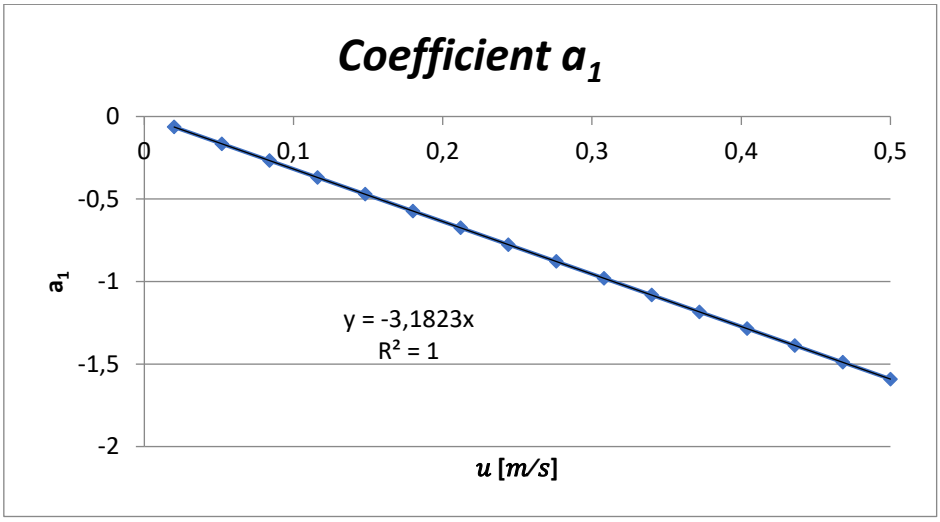

Figure 3-6:Coefficient a1 in function of HTF speed

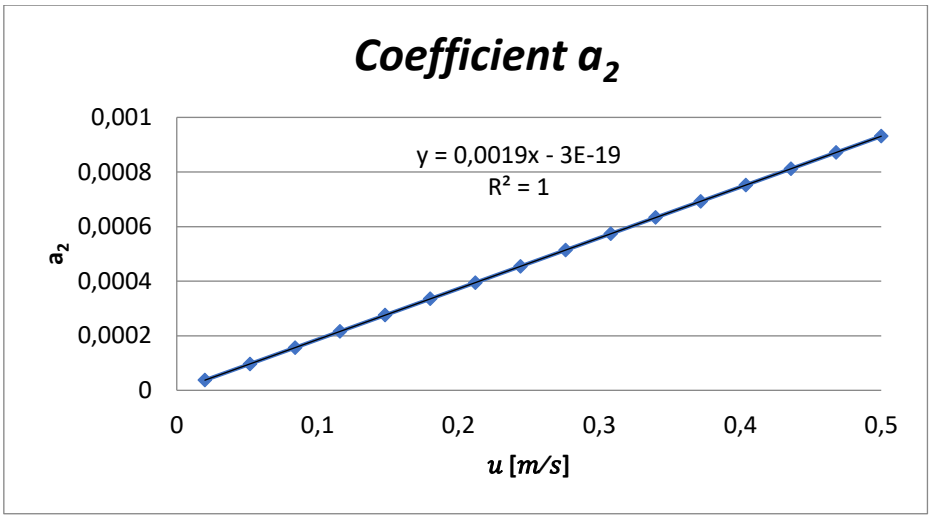

Figure 3-7:Coefficient a2 in function of HTF speed

Although the order of magnitude is not homogeneous between different contributions, due to the different nature of them, the first useful consideration come from the relation between each coefficient with the HTF speed: in first approximation the behaviour could be considered linear, because the first term of the pressure drop equation is related with the first order u.

In the following part it is evaluated the second parameter:

$u\ [^{m}/_{s}]$	b_2	b_1	b_0
0,02	0,0000	-0,0005	2,6830
0,052	0,0000	-0,0034	18,1370
0,084	0,0000	-0,0090	47,3280
0,116	0,0000	-0,0171	90,2559
0,148	0,0000	-0,0279	146,9208
0,18	0,0000	-0,0412	217,3226
0,212	0,0000	-0,0572	301,4613
0,244	0,0000	-0,0758	399,3369
0,276	0,0000	-0,0969	510,9495
0,308	0,0000	-0,1207	636,2990
0,34	0,0000	-0,1471	775,3855
0,372	0,0001	-0,1761	928,2088
0,404	0,0001	-0,2077	1094,7691
0,436	0,0001	-0,2419	1275,0664
0,468	0,0001	-0,2787	1469,1006
0,5	0,0001	-0,3181	1676,8717

Table 3-5:Empirical values of the constant b0, b1, b2 for a set of HTF speed

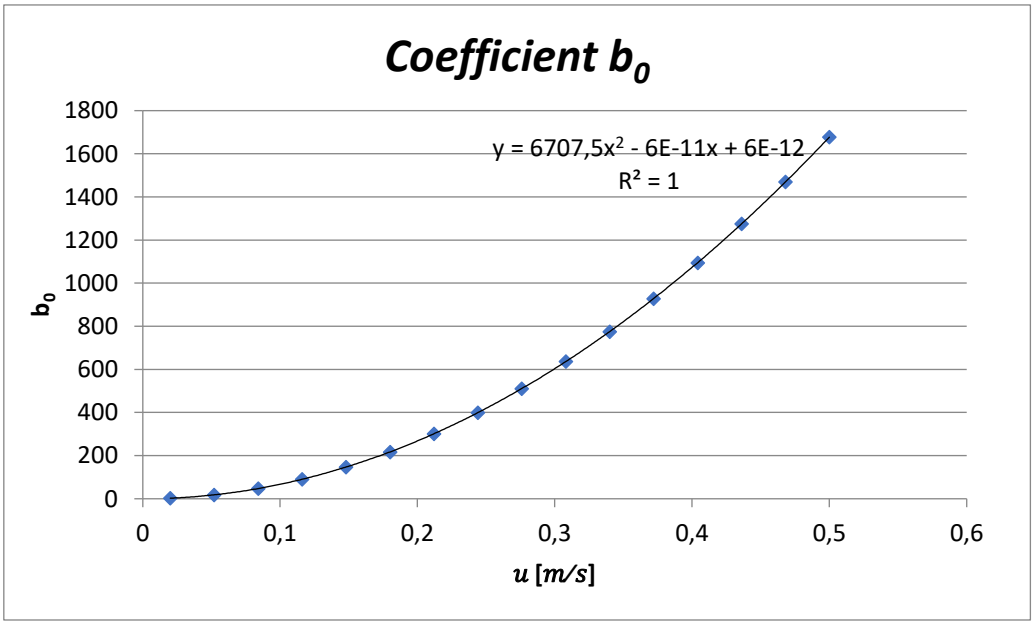

Figure 3-8:Coefficient b0 in function of HTF speed

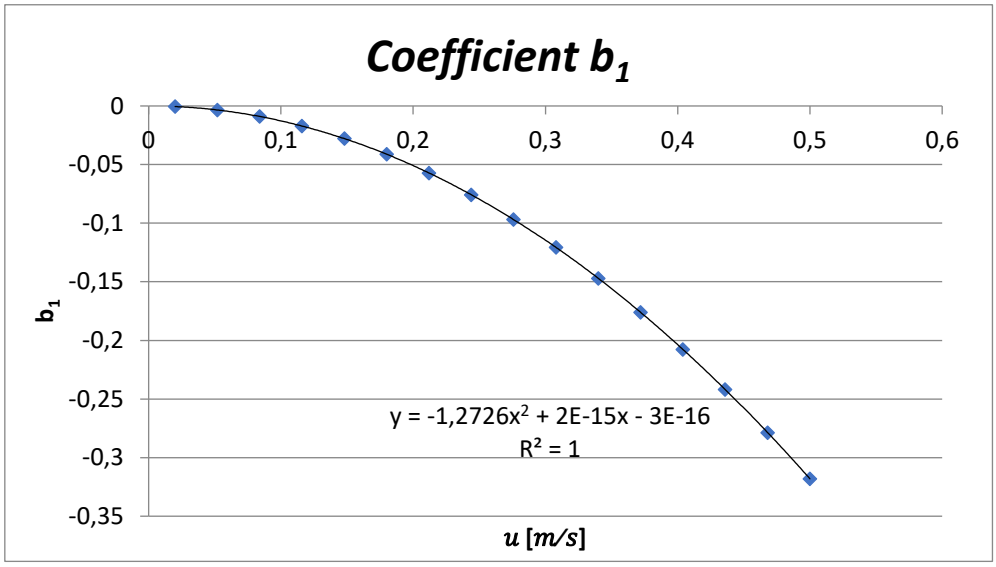

Figure 3-9:Coefficient b1 in function of HTF speed

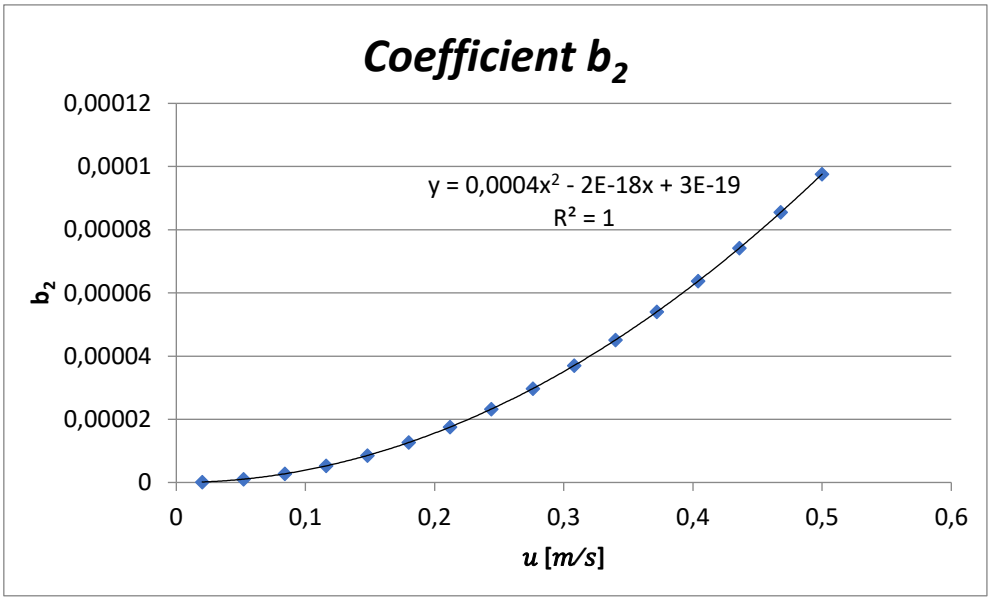

Figure 3-10:Coefficient b2 in function of HTF speed

In this case the order of magnitude is still not homogeneous between different parametrical contributions, but it is easy to find a physic meaning: the parabolic behaviour shows the second order relation of the second term in the pressure drop equation with u.

Once obtained the empirical values a_0, a_1, a_2 in function of the variable Y_1 and the values of b_0, b_1, b_2 in function of the variable Y_2 corresponding to a set of HTF speed, the purpose of the following evaluation consists into find an expression for the pressure drop with a general law, function of u. It was established a general second order equation to express the variation of each

empirical parameter just determined ($a_0, a_1, a_2, b_0, b_1, b_2$) with the speed u, using a regression method.

In that case, two analytical functions on this form were obtained:

$$a_n(u) = f_0 + f_1 \cdot u + f_2 \cdot u^2 \tag{3.24}$$

$$b_n(u) = f_0 + f_1 \cdot u + f_2 \cdot u^2 \tag{3.25}$$

In the *table 3.6* are reported the analytic coefficient f_0, f_1, f_2 founded:

	f_2	f_1	f_0
a_2	9,33E-18	**1,86E-03**	3,59E-19
a_1	-3,51E-14	**-3,18E+00**	-1,64E-15
a_0	2,59E-11	**4,30E+03**	1,10E-12
b_2	**3,90E-04**	-2,07E-19	1,36E-20
b_1	**-1,27E+00**	3,20E-15	-2,36E-16
b_0	**6,71E+03**	-1,00E-11	7,96E-13

Table 3-6:Empirical values of the constant f0, f1, f2 in function of HTF speed

All the terms with a value lower than 1E-10 are considered negligible and in bold are presented the only terms to keep in consideration: for a_n functions is f_1, corresponding with the first order dependence, while for b_n functions is f_2, that exactly corresponds with the expectations.

According to the equations 3.24 and 3.25, the two terms for the pressure drop could be written in function of both the Y and the u:

$$\frac{\Delta P_{exp\_1}}{L}(u, Y_1) = 4{,}30\text{E}+03 \cdot u - 3{,}18E+00 \cdot u \cdot Y_1 + 1{,}86E-03 \cdot u \cdot {Y_1}^2 \tag{3.26}$$

$$\frac{\Delta P_{exp\_2}}{L}(u, Y_2) = 6{,}71E+03 \cdot u^2 - 1{,}27E+00 \cdot u^2 \cdot Y_2 + 3{,}90E-04 \cdot u^2 \cdot {Y_2}^2 \tag{3.27}$$

The total pressure drops are express like the sum of these members expressed in the *equations 3.26-3.27*:

$$\frac{\Delta P_{exp}}{L}(u,Y) = \frac{\Delta P_{exp\_1}}{L}(u,Y_1) + \frac{\Delta P_{exp\_2}}{L}(u,Y_2) \tag{3.28}$$

In this way, based on the experimental information obtained, it is possible to determine the pressure drop for a quartzite gravel of any size and porosity, using the fitting parameters just founded, in any condition of HTF temperature and pressure and at any HTF speed.

The field of application for these parametrical coefficients are valid in a fixed range of HSM porosity (0.38-0.50) and diameter (2-7 mm) and in a range of HTF speed, corresponding with a range of Reynolds. This is because for cryogenic applications, temperature and pressure conditions are completely different with respect to the ambient condition in which the experiment was performed: to understand the range of validity of this method about pressure losses estimation just found, it is important to consider the Reynolds number, that offer more detailed information. Fixed the condition of the HTF in the experiment, the minimum value of Reynolds number is 2.8, considering the lowest particle diameter and the smallest speed, while the maximum value is 206.3.

3.2.1.3 Mixed approach

If the heat storage material, supposed to use for a cold energy storage, is not perfectly spherical or not irregular shaped like the quartzite gravel, it is necessary to create an adapted model. As introduced in the *chapter 3.1.3*, one of the input variable in the parametric analysis is represented by a pressure drop factor *X,* whose value could be chosen in a range from 0 to 1. The *equation 3.42* puts in relation the input *X* with the $\Delta P/_l$, with a model that combines the theoretical and the experimental pressure drops:

$$\frac{\Delta P}{L} = \frac{\Delta P_{Ergun}}{L} \cdot \left(1 + X \cdot \left(\frac{\frac{\Delta P_{Exp}}{L}}{\frac{\Delta P_{Ergun}}{L}} - 1 \right)\right) \tag{3.29}$$

Where:

$\frac{\Delta P}{L}$ is the pressure drop obtained in the mixed approach (Pa/m)

$\frac{\Delta P_{Ergun}}{L}$ is the pressure drop obtained by the theoretical approach (Pa/m)

X is related to the shape of the HSM selected (-)

$\frac{\Delta P_{Exp}}{L}$ is the pressure drop obtained with the experimental approach (Pa/m)

3.2.2 Heat leaks contribution

In the cold energy storage, the heat storage medium is kept at cryogenic temperature and despite the insulation provided in the configuration, the heat leaks to the external environment represents an important energy lost.

Considering an interval of time of 24 hours, the Energy lost due to the heat leaks is expressed in the *equation 3.30,* considering the case of 1-D in cartesian geometry:

$$E_{heat\ leaks} = \frac{1}{\frac{1}{k/s} + \frac{1}{h}} * \left(T_{ext} - T_{HSM,average}\right) * \Delta t_{day} \qquad (3.30)$$

Where:

$E_{heat\ leaks}$ is the energy lost for the heat leaks (kWh)

k is the thermal conductivity of the insulation (W/mK)

s is the insulation thickness (m)

h is the external heat transfer coefficient (W/m^{2}K)

T_{ext} is the external temperature (K)

$T_{HSM,average}$ is the average temperature of the heat storage medium (K)

Δt_{day} is 24 hours

The first term $\frac{1}{\frac{1}{k/s}+\frac{1}{h}}$ represents the inverse of the thermal resistance and combine the convective and conductive mechanism of thermal transfer. For this cryogenic plant, one solution could be the use of vacuum as thermal insulation system and another is the use of a multilayer fiberglass material with an aluminium coating, to reduce the radiative heat transfer. Considering an imperfect level of void in the first case or the aluminium coating for the fiberglass, in this study the radiative term is considered negligible with respect to the conductive and convective contributions. To a lower amount of thermal losses is preferable a shape of the storage with high L/D ratio.

3.2.3 Thermocline losses

For the heat storage application, the thermocline is the layer inside a medium in a storage with a thermal gradient. The layer below and above the thermocline could be considered at constant temperature. Higher is the height of this layer in the storage, lower is the exergetic content of the storage due to temperature mixing phenomena. This concept is very important in a dynamic model because its contribution is more accentuated in the charge or discharge phase.

In this study it is applied the simplified model presented in the *figure 3.11*, with three zones and all the thermal gradient is developed in the Zone 2 (thermocline).

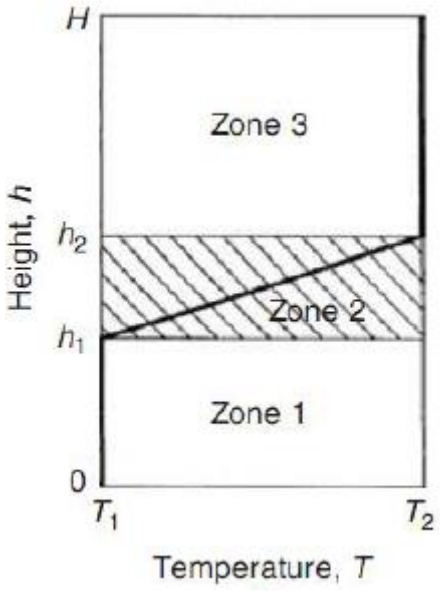

Figure 3-11:Coefficient b2 in function of HTF speed

The energy lost due to the presence of the thermocline is related to the fraction of the energy stored within the thermal gradient:

$$E_{thermocline} = E_{storage} \cdot \frac{\Delta x_{gradient}}{h_{packed\ bed}} \tag{3.31}$$

Where

$E_{thermocline}$ is the energy dissipated in the thermocline region (kWh)

$E_{storage}$ is the total energy contained in the cold storage (kWh)

$\Delta x_{gradient}$ is the thickness of the thermocline inside the storage (m)

$h_{packed\ bed}$ is the height of the heat storage material (m)

The Ranz and Marshall correlation allowed the estimation of the total area needed for the heat exchange at the rate provided by the HX and transferred via HTF to the HSM: it corresponds to the total area of the quartzite particles in the thermocline, as showed in *equation 3.32.* With this consideration is now possible to evaluate the thermal gradient thickness inside the storage, considering that all the heat is exchanged in this zone, for the presence of a thermal gradient.

$$A_{needed} = \frac{P_{exchanged}}{h * \Delta T_{average}} \tag{3.32}$$

Where

$P_{exchanged}$ is the average power exchanged from the HTF to the HSM, considering that the energy stored is discharged in 2.5 hours (W)

A_{needed} is the total area of the storage medium needed (m^2)

h is the heat transfer coefficient (W/m^2K)

$\Delta T_{average}$ is the average of the temperature differences between HTF and HSM (K), expressed in *equation 3.44*

The difference between HTF and the HSM temperature during the discharge or the charge of the system in evaluated splitting them up into subintervals. Keeping into account the energy exchanged in each interval with a certain flowrate and with the associated variation of the heat capacity, the ΔT is expressed in the *equation 3.45* and represented in the *figure 3.12.*

$$\Delta T_i = T_{HSM,i} - T_{HTF,i}(h_{HTF,i}) \tag{3.33}$$

Where

ΔT_i is the temperature difference between the HTF to the HSM (K) in each interval

$T_{HSM,i}$ is the temperature of the storage medium (K)

$T_{HTF,i}(h_{HTF,tot,i})$ is the temperature of the heat transfer fluid, in function of its total enthalpy, obtained in the *equation 3.46*

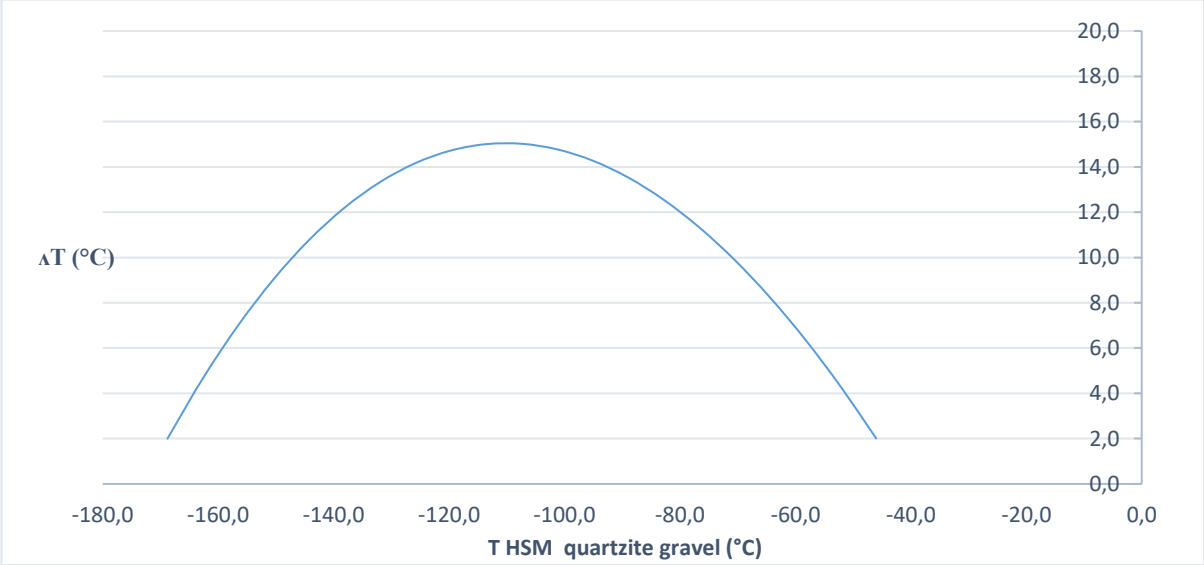

Figure 3-12:ΔT evolution between HTF and HSM

The enthalpy related to the HTF is:

$$h_{HTF,i} = h_{HTF,0} + h_{exchanged,i} \cdot \frac{\dot{m}_{HSM,cooled}}{\dot{m}_{HTF}} \tag{3.34}$$

Where

$h_{HTF,i}$ is the HTF enthalpy in the considered interval (J/kg)

$h_{HTF,0}$ is the HTF enthalpy at the storage inlet conditions, associated with the minimum temperature (J/kg)

$h_{HTF,exchanged,i}$ is the enthalpy exchanged from the HSM to the HTF until the considered interval (J/kg)

$\dot{m}_{HSM,cooled}$ is the mass of storage material cooled for each second (kg/s)

$\dot{m}_{HTF}$ is the mass of heat transfer fluid flowing in the cold energy storage (kg/s)

The total enthalpy exchanged between the HTF and the HSM increased with the increasing of the temperature of the storage material and consequently with time. Its expression is:

$$h_{exchanged,i} = (T_{HSM,i} - T_{HSM,i-1}) * \frac{c_{p\ HSM,i} - c_{p\ HSM,i-1}}{2} + h_{exchanged,i-1} \qquad (3.35)$$

Where

$h_{HTF,i}$ is the HTF enthalpy in the considered interval (J/kg)

$h_{HTF,0}$ is the HTF enthalpy at the storage inlet conditions, associated with the minimum temperature (J/kg)

$h_{HTF,exchanged,i}$ is the enthalpy exchanged from the HSM to the HTF until the considered interval (J/kg)

$\dot{m}_{HSM,cooled}$ is the mass of storage material cooled for each second (kg/s)

$\dot{m}_{HTF}$ is the mass of heat transfer fluid flowing in the cold energy storage (kg/s)

Knowing the area of the storage material needed, the goal of this section is to determine the thermocline thickness, obtained with the *equation 3.36:*

$$\Delta x_{gradient} = \frac{A_{needed}}{A_{HSM\ particle}} \cdot \frac{d_{HSM\ particle}}{\#_{particles\ per\ layer}} \qquad (3.36)$$

Where

$\Delta x_{gradient}$ is the thermocline thickness (m)

A_{needed} is the overall area of storage material needed (m^2)

$A_{HSM\ particle}$ is the area of a single particle of storage material (m^2)

$d_{HSM\ particle}$ is the diameter of a single particle of storage material (m)

$\#_{particles\ per\ layer}$ is the number of particle per each layer of the storage: for definition the height of each layer corresponds to the average diameter of the particle

The first member constituted by the ratio $\frac{A_{needed}}{A_{HSM\ particle}}$ represents the number of storage material particles needed to satisfy the requirement of area needed obtained in the *equation 3.32.*

3.3 Definition of the best Cold Energy Storage layout

The combination of the 6 inlet parameters, introduced in the *chapter 3.1.3*, creates more than 30000 different system configurations, all with a different overall efficiency. There are analysed, through graphical evaluation, with different combinations of parameters, with the purpose to define the best layout in each situation. The best system efficiency is the key criteria evaluated in this work, always in function of 2 variables, while the values of the remaining parameters (4) correspond to the value that could ensure the maximum efficiency.

From the rest of the chapter, the simulation performed with the pressure drop factor (X) equal 0, represented in orange and obtained by Ergun equation, will be called theoretical, while for the situation with pressure drop factor equal 1, they will be called experimental and will be represented in green.

The *figure 3.13* for the theoretical behaviour and the *figure 3.14* for the experimental, show the evaluation of the number of HSM layers in series corresponding to the optimal configuration, varying the HTF inlet pressure and the value of the thermal conductivity of the insulation. High number of layers means taller storage and more thermal dispersions, because the total S/V ratio will be increased. For this reason, the optimal numbers of layers become higher when the insulation is more efficient and consequently the thermal conductivity is lower. Furthermore, a taller storage increases the pressure drops, that depend directly from the HTF density: higher number of layers become more efficient when the value of the inlet pressure is lower.

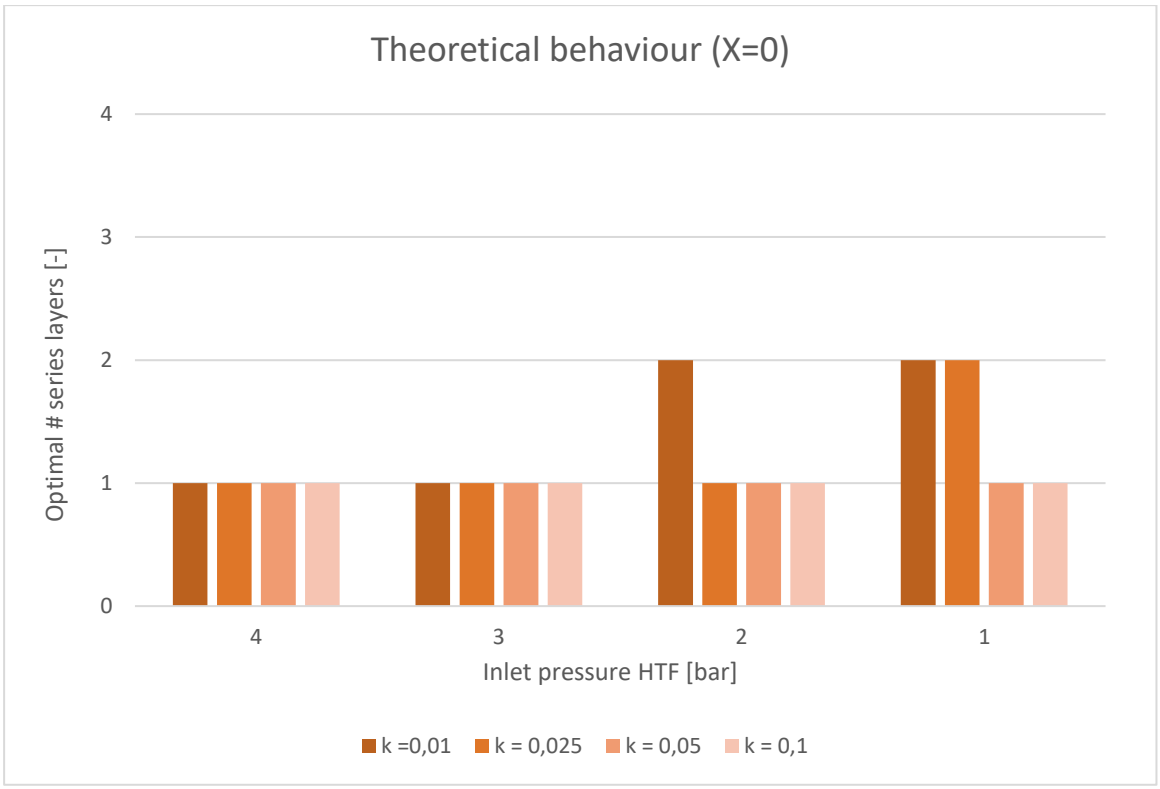

Figure 3-13:Optimal # layers in theoretical behaviour

Figure 3-14: Optimal # layers in experimental behaviour

The trend for the charts represented in *figure 3.13* and in *figure 3.14* is very similar, but the number of optimal series layers increases if the model adopted for the pressure drop evaluation is experimental. This is because more layers represent a possibility to decrease the pressure losses, bypassing some layer of storage material when it is not necessary. With a good insulation and with a low inlet pressure, the more efficient configuration is 2 layers in first case and is 3/4 in the second. In the opposite situation 1 layer is the best option.

In the chart represented in *figure 3.15* is developed a study about system efficiency variation in function of the insulation thermal conductivity and HTF inlet pressure, in the case of theoretical approach. The most critical factor is represented by the insulation thermal conductivity: considering a value of 0.1 W/mK instead 0.01 W/mK, causes an efficiency decrease of almost 20%, both for low and high-pressure inlet. Furthermore, it is possible to notice a general increment of efficiency due to higher pressure inlet: a general high pressure generates slightly more absolute pressure losses for the increase of HTF density, but the pressure ratio defined as $\frac{P_{out}}{P_{in}}$ is substantially lower.

With bad quality insulation the increase of the efficiency due to the HTF pressure inlet is around 3%, while with a good insulation is only 1.5%. Considering that, to ensure a good performance it's more important to invest money on the insulation with respect to keeping the circuit at high pressure.

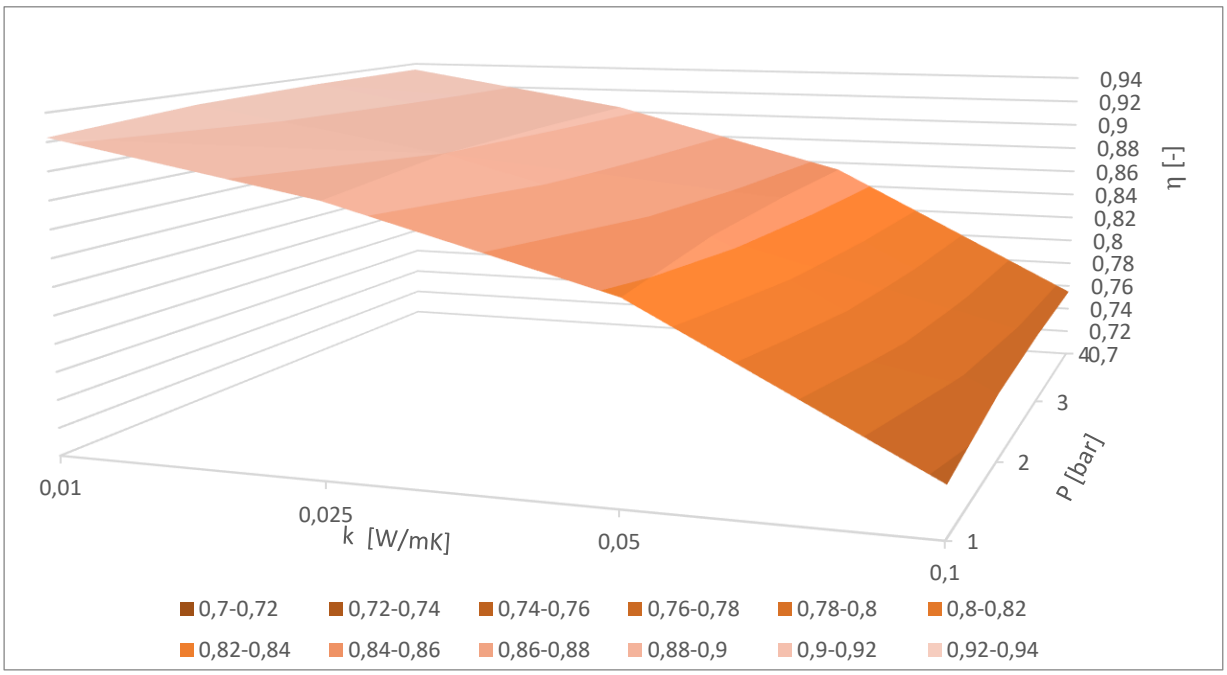

Figure 3-15: Cold energy storage efficiency in function of insulation thermal conductivity and HTF inlet pressure in theoretical approach

The trend with the same conditions, in experimental approach, shows the same behaviour, with a similar slope, with lower efficiency of 1-3%: the maximum efficiency is 93.45% in the first case and 92.51% in the second.

With both theoretical and experimental approach, were performed similar graphical evaluations of the system performances, coupling the variation of insulation thermal conductivity with all the other parameters demonstrate a common behaviour: the variation of the efficiency changing HSM particle diameter, number of layers and slenderness is almost ten times lower than the effect of insulation. The efficiency variation of the system with D is from 2% to 3%, while the influence of # is almost 1.5/4%, and for SL is from 2% to 4%, with always a lower floating value in the case of good insulation quality. One additional study shows the influence of the optimal HSM diameter varying the slenderness for both theoretical and experimental approach: with a small diameter, the best configuration is low slenderness, while for bigger value is better higher one.

The chart in *figure 3.6* establish the relationship between the system performances and the variation of particle diameter and inlet pressure in theoretical approach. The diameter trend highlights a maximum in correspondence to the value of 2/3 mm: with the decreasing of the size, the efficiency rises (almost +4% for all inlet pressure values), showing an elbow at the value 3 mm. A low particle diameter increases the pressure drops significantly however, the primary effect is the growth of the S/V ratio and consequently, the heat transfer mechanism between the HTF and the HSM becomes more powerful. In line with expectations, the system is more productive with high pressure inlet for value of almost 2/3%. With the experimental approach, the trend is exactly the same and the corresponding efficiency is lower of 2% averaged.

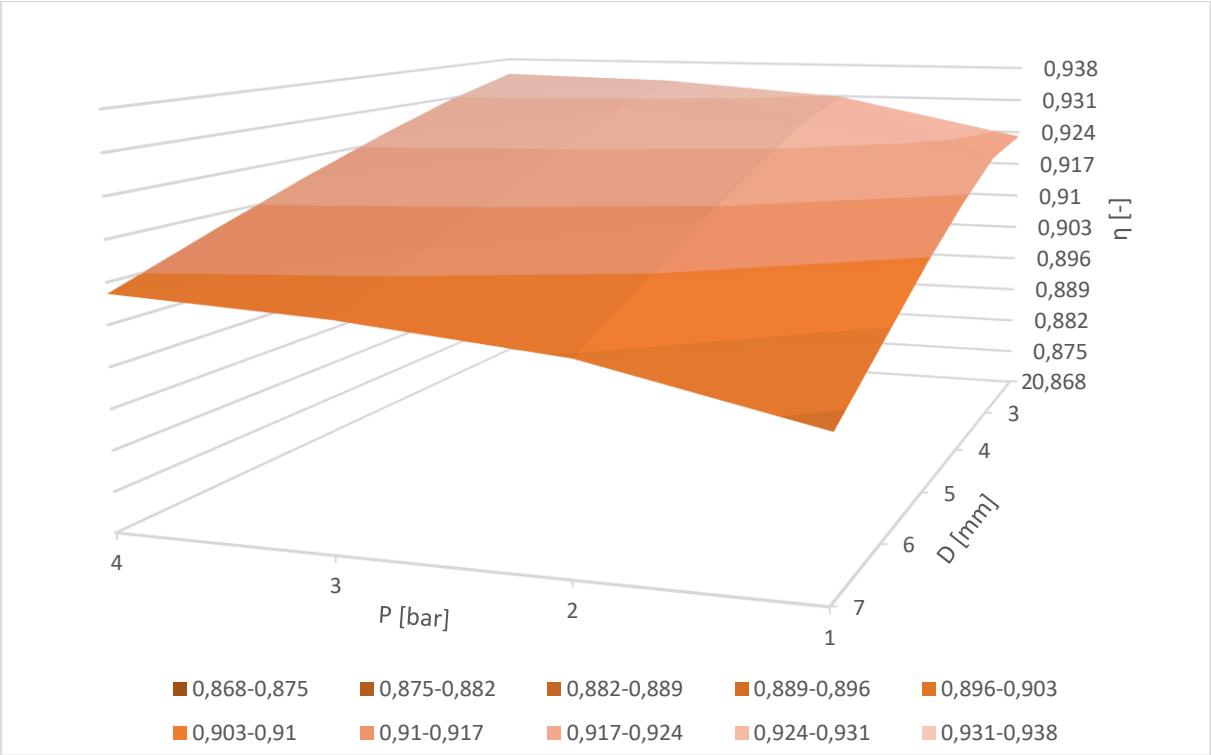

Figure 3-16: Cold energy storage efficiency in function of HSM particle diameter and HTF inlet pressure in theoretical approach

From the previous studies, it is possible to conclude that for some parameters is not too difficult to find a global optimum point: with the lowest insulation thermal conductivity, the lowest diameter and the higher pressure the system efficiency is basically better. The same considerations are not valid for the absolute best choice of slenderness and number of series layers: the last graphical analysis achieved keep in relationship the two parameters that affected only the external design of the storage.

Considering the theoretical approach represented in *figure 3.17,* the optimum point is the combination of 1 layer and slenderness equal 1, but very similar system performances are reached considering 2 layers and slenderness equal 2. Many layers make the storage taller and consequently the slenderness rises. It is possible to observe a sharper decrease of the efficiency when the number of layers or the slenderness become higher than 2. With all the possible configuration in the theoretical approach the highest loss is almost 1%, because the Y-axe is denser compared to what is represented with the experimental approach in the *figure 3.18*, where the decrement between the best and the worst point is almost 4%, mostly due to the increasing the slenderness, that generates great pressure drops. In this case too, the worst

combination is higher slenderness coupled with low number of layers or vice versa but the influence of varying the number of layers is more accentuated for higher slenderness.

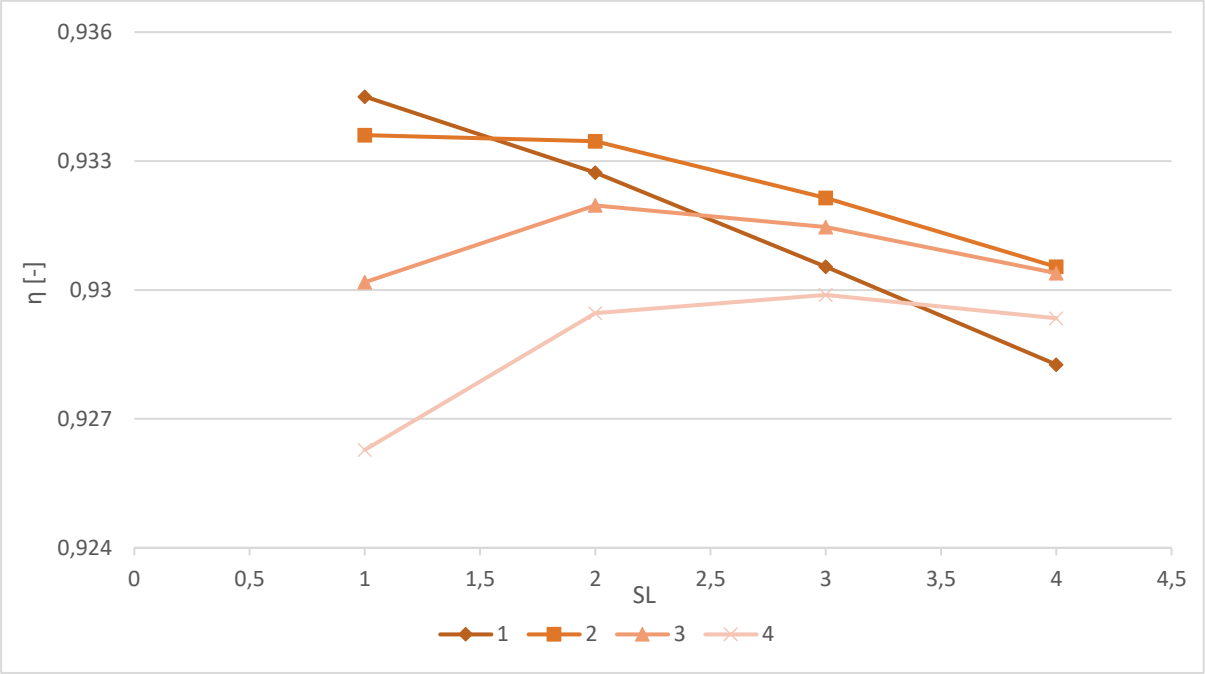

Figure 3-17: Cold energy storage efficiency in function of slenderness and number of layers in theoretical approach

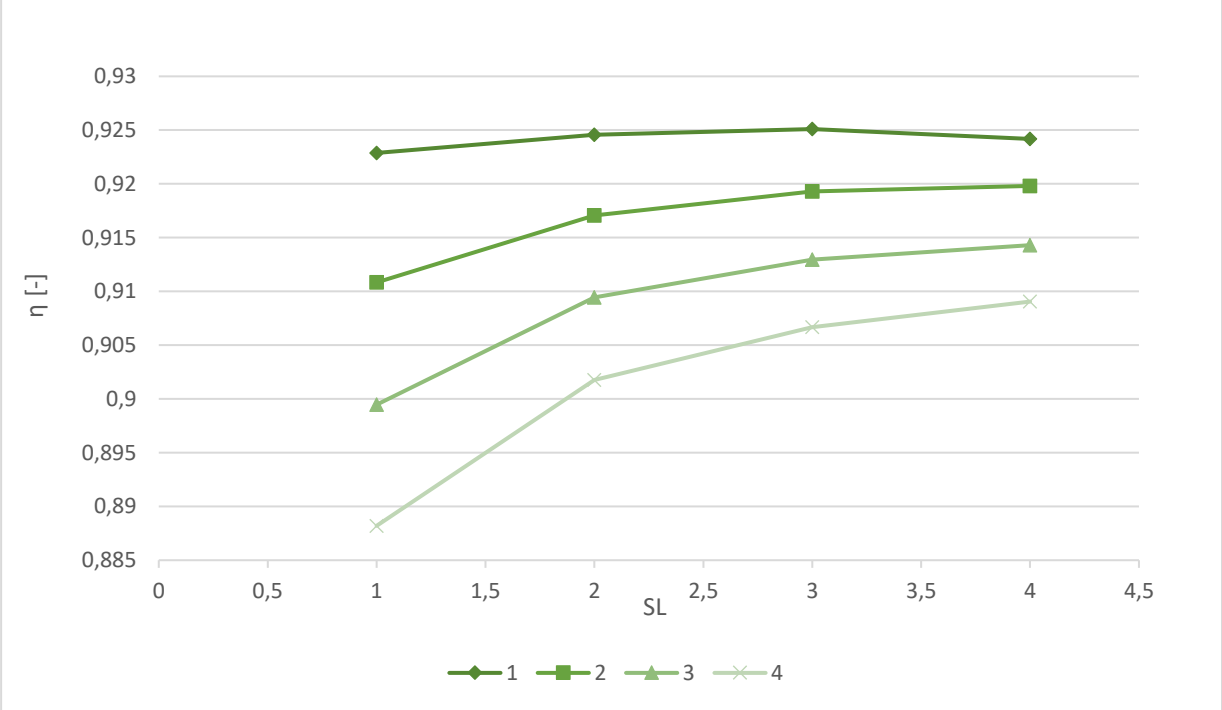

Figure 3-18: Cold energy storage efficiency in function of slenderness and number of layers in experimental approach

From an economical point of view, a multi-layer storage is more expensive for the presence of valves and control system so, in case of equal yield, it is suggested to choose 1 or 2 layers in series, with an adequate slenderness.

3.4 Approximated numerical methods for the evaluation of the Cold Energy Storage Efficiency

In this chapter will be presented different methods to evaluate the efficiency of the system without the whole processes and calculations performed in the *chapters 3.2*. The basic idea is to find out a general law or a method to keep in relationship all the inlet parameters with the round-trip efficiency for a cold energy storage system described in *chapter 3.1*.

Once the over 30000 simulations, that represent all the possible combination of the inlet parameters, were collected in a database, three different analytical methods are developed: a multiple regression method with a sixth-grade polynomial function, a linear and a polynomial approximation found with the Kriging method. All these methods are characterized by an approximation error.

3.4.1 Multiple regression method: polynomial approximation

The multiple regression represents a statistical method of the awaited value estimation, conditioned by one dependent value, considering the value of others independent variables.

Assuming the example of a single-variable regression, where the system efficiency is only function of the particle HSM diameter (D), the *figure 3.19* shows in red the simulated points obtained with the calculations and in a black dashed line the trend of the polynomial approximation up to third grade.

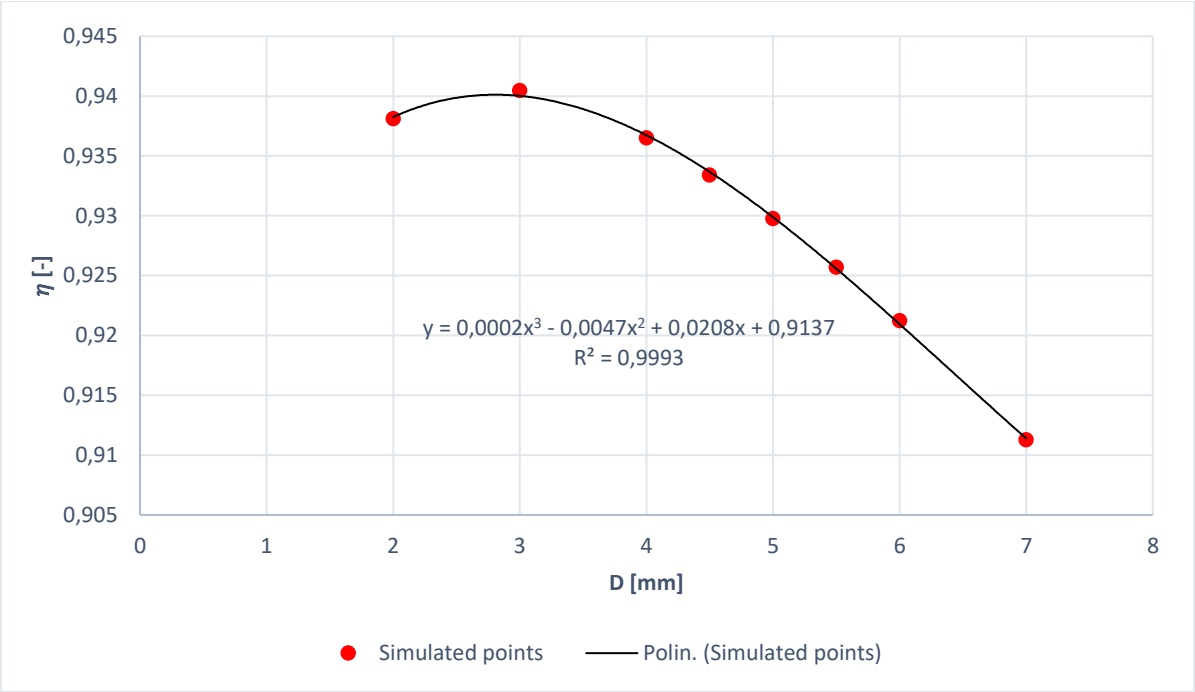

Figure 3-19: Trendline and polynomial approximation with a third-grade polynomial

An important parameter to evaluate the accuracy of the approximation is the R^2, the determination coefficient. It compares the y values estimated with those effectives and its value is include between 0 and 1: higher the value of R^2, better quality for the analytical approximation.

In this work it is considered a multiple dimension domain in space: the efficiency is function of 6 input variables, so the total dimension corresponds to the number of variables plus one and it is expressed in this form:

$$\eta = f(k_{ins}, P, D, \#, SL, X)$$

All the points of efficiency obtained during the previous simulation are considered like experimental points and the purpose is to find a unique and univocal function that describes the behaviour of the efficiency varying the input parameters, with a good approximation. After several attempts, the best choice results a polynomial expression of sixth grade to minimize the errors. It was decided to use only terms with pure coefficients, to avoid making the equation too complicated and for the impossibility to explain the physical meaning of mixed terms. The formulation chosen is the following with the following expression:

$$\eta = \eta_0 + \sum_{n=1}^{6} a_n \cdot {k_{ins}}^n + b_n * P^n + c_n \cdot D^n + d_n \cdot \#^n + e_n \cdot SL^n + f_n \cdot X^n \qquad (3.37)$$

Where:

$D, P, \#, SL, k_{ins}, X$ are the input variable selected in this analysis

$a_n, b_n, c_n, d_n, e_n, f_n$ are the empirical coefficient determined by the multiple regression with the support of the Excel 2016® function LINEST

In the *table 3.7* are displayed all the empirical coefficients obtained from the analysis and to use in the equation 3.37. The value of η_0, corresponding to the value of the Y-intercept, was not fixed equal zero but automatically calculated by the programme algorithm. This solution was adopted because it is in principle with the data used: all the combination of parameters that provides an efficiency below 70% were excluded from that analysis, because they represent less than 5%.

Examining the results, it is possible to notice the absence of the terms higher than third order relative to the k_{ins}, probably due to the high influence of this parameter on the system efficiency. Also, the first two order coefficients relative to the # are null: in first approximation the relevance of the number of layers is negligible.

	a_n	b_n	c_n	d_n	e_n	f_n	η_0
n=1	-2,29E+00	9,28E-02	7,43E-02	0,00E+00	2,44E-02	-3,45E-02	7,36E-01
n=2	-1,21E+00	-3,56E-02	-1,93E-02	0,00E+00	-1,18E-02	2,10E-02	
n=3	4,46E+00	3,56E-04	3,67E-03	1,59E-04	1,11E-02	0,00E+00	
n=4	0,00E+00	2,91E-05	3,19E-04	6,73E-05	1,74E-03	1,82E-02	
n=5	0,00E+00	6,21E-10	5,25E-09	1,35E-07	1,72E-07	3,03E-02	
n=6	0,00E+00	6,93E-08	1,02E-06	1,79E-06	1,79E-05	3,85E-02	

Table 3-7:Empirical coefficients obtained with the multiple regression method with a polynomial approximation of sixth-grade

The determination coefficient R^2 of this approximation is 0.93 and the standard deviation SE is 0.0185: they are considered good indicators, considering the complexity of the analysis for the presence of six variables. Another method to check the quality of the method is due to the evaluation of the relative and absolute errors.

The absolute error expresses the absolute difference, in terms of percentage, between the value calculated and the value obtained with this analytical. The subscript *i* represents all the different combination of the inlet parameters and the formulation is:

$$\epsilon_{abs,i} = abs\left(1 - \frac{\eta_{calc,i}}{\eta_{approx,i}}\right) \tag{3.38}$$

Where:

$\epsilon_{abs,i}$ are the error of the approximation of the multiple regression method

$\eta_{calc,i}$ is the efficiency of the system determined with the analytical method described in chapter 3.1 and *3.2*

$\eta_{approx,i}$ is the efficiency estimated with the multiple regression method

The average of the absolute error $\epsilon_{abs,ave}$ for all possible parametrical combinations was estimated with the value of 1.41%.

3.4.2 Kriging linear

This approach is based on a numerical prevision of the value of a function at given point, by computing a weighted average of the known values of the function in the neighbourhood of the point investigated. It is called Kriging or Gaussian process regression and describe a multi-stage process of interpolation, based on the calculation and the modelling of the experimental variogram (49): it is a discrete function calculated using measure of variability between pairs of points at various distances (50).

The goal of this new method is to estimate the system efficiency with a new set of inlet parameters established by the user, relying only on the values of the function that are already

known: the database of almost 30000 simulations already performed with the calculations in *chapter 3.2.*

The idea was to find a way to determine the total distance $R_{tot,i}$ between the new point selected and all the points in the database with the *equation 3.54* and choose the closest to perform the interpolation. To find the distance identified with each parameter it is necessary to consider each maximum possible value, to estimate a relative distance with the following expressions:

- $R_{k_{ins}} = \frac{k_{ins,i} - k_{ins,unknown}}{k_{ins,max}}$
- $R_P = \frac{P_i - P_{unknown}}{P_{max}}$
- $R_D = \frac{D_i - D_{unknown}}{D_{max}}$.
- $R_{\#} = \frac{\#_i - \#_{unknown}}{\#_{max}}$
- $R_{SL} = \frac{SL_i - SL_{unknown}}{SL_{max}}$
- $R_X = \frac{X_i - X_{unknown}}{X_{max}}$

Where the subscript *i* means each point of the database, subscript *unknown* indicates the parameters values of the unknown point selected and the subscript max represents the maximum value that could assume that parameter in this analysis.

The distance $R_{tot,i}$ is identified with a simplified method, that described the assumption of a linear approximation, as the square root of the sum of the squares of the distance identified with each parameter, also if their modules are not consistent among them.

$$R_{tot,i} = \sqrt{R_{k_{ins}}^2 + R_P^2 + R_D^2 + R_\#^2 + R_{SL}^2 + R_X^2} \tag{3.39}$$

From the database, it was found the point with the maximum distance R_{max} with respect to the new point under evaluation and it was assigned at each point in the database a weight W_i, expressed in the *equation 3.40*:

$$W_i = 1 - \frac{R_{tot,i}}{R_{max}} \tag{3.40}$$

Where:

W_i is the weight assigned to each point in database

$R_{tot,i}$ is the total distance between each point in database and new point under evaluation

R_{max} is the maximum distance found inside the points in database

The weight assumes values included between 0, when is considered the farthest point and 1, if ideally the new point coincides perfectly with one already present in the database used: higher W means higher consideration given to that point.

They must be considered only the *N* points of the database that are the closest to the new point under evaluation: in this study they were performed different simulation with N=10, 20, 50, 75, 100 and the points that are outside the selected neighbourhood are not included in the analysis and their weight considered is 0:

$$W_i = \begin{cases} W_N & if\ R_{tot,i} \leq R^* \\ 0 & if\ R_{tot,i} > R^* \end{cases}$$

Through an iterative algorithm, the N set by the user is translated into the distance of the farthest point that must be included, defined as *R**: if the distance $R_{tot,i}$ of the *i*-th point is bigger than *R*,* that point is excluded.

For the N points is calculate the respective weighted efficiency, that represents as expressed in the *equation 3.41*:

$$\eta_{weighted,N} = \eta_N \cdot W_N \tag{3.41}$$

Where:

$\eta_{weighted,N}$ is the weighted efficiency for each N points in database

η_N is the real efficiency of the N points calculated in database

W_N is the weight assigned to each N points in database

The following step consist into find a univocal value that describes the approximated efficiency of the unknown point in relation of the values of weighted efficiency and weight found for the N points:

$$\eta_{unknown} = \frac{\sum_{j=1}^{N} \eta_{weighted,j}}{\sum_{j=1}^{N} W_j} \tag{3.42}$$

Where:

$\eta_{weighted,N}$ is the weighted efficiency for each N points in database

$\eta_{unknown}$ is the approximated efficiency for the unknown point

The respective efficiency of the unknown points is evaluated also with the analytical method described in *chapter 3.2* and the results are compared with the approximated efficiency estimated with the *equation 3.57,* with the resulting errors:

$$\epsilon_{abs,unknown} = abs\,(1 - \frac{\eta_{unknown\ approx}}{\eta_{unknown,analytic}}\ ) \tag{3.43}$$

Where:

$\epsilon_{abs,unknown}$ is the absolute error in the estimation of the efficiency for the unknown point with the Kriging linear method

$\eta_{unknown\ approx}$ is the approximated efficiency for the unknown point *equation 3.57*

$\eta_{unknown,analytic}$ is the nalytical efficiency for the unknown point from the model described in *chapter 3.2*

To have a proof of consistency and effectiveness of the Kriging linear method adopted, they were performed 1000 simulations with their respective new configuration input parameters, different with respect to the database.

The efficiency of this method could be defined as the average over the 1000 unknown points new configurations considered, and in the *figure 3.20* it is expressed varying the N.

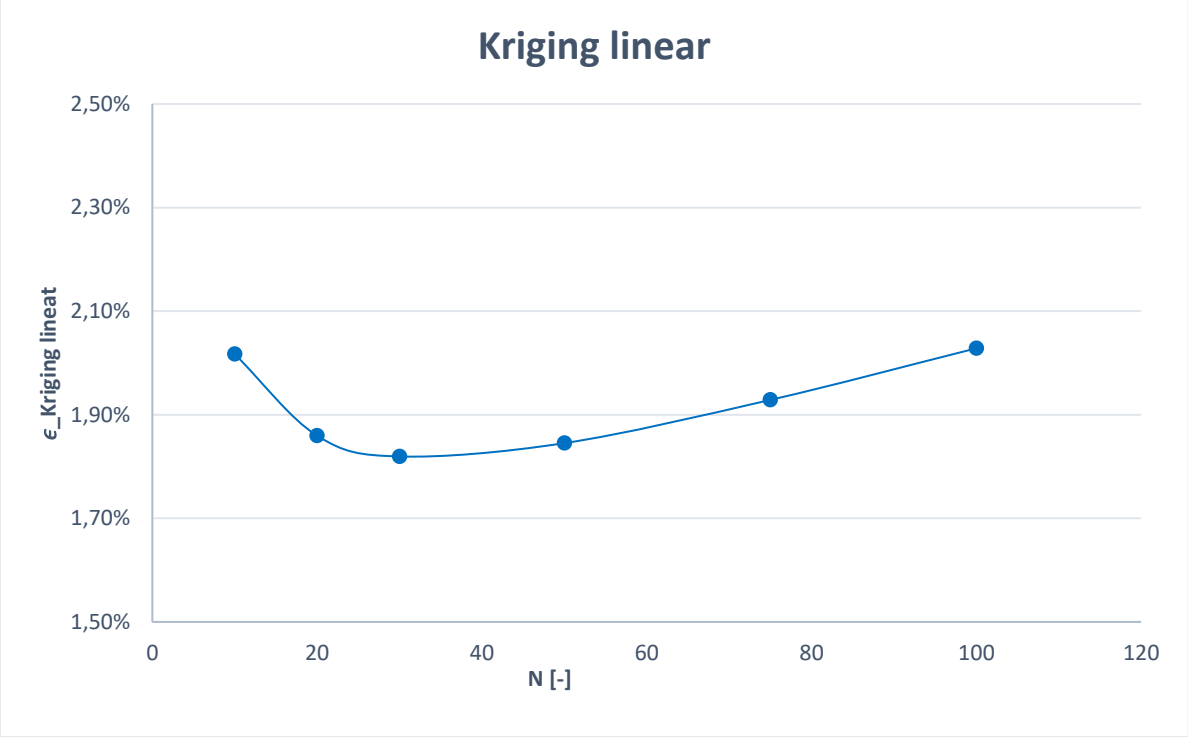

Figure 3-20: Error of the Kriging Linear approximation method

It was selected the lowest value of N=20 to have a minimum significant sample of point to apply effectively the method. Later, was studied the behaviour of the error when N increases and in the figure 3.17 was found immediately an optimal point: setting N=30, the minimum error evaluated for the Kriging linear method is 1.82%. The model analysis was restricted at

N=100 and not over because the trend of the error is evidently increasing: selecting too many points, the interpolation method results less accurate.

3.4.3 Kriging polynomial

The Kriging polynomial is a method proposed to enhance the accuracy of the Kriging linear approach, mixing it with the multiple regression function adopted in the *chapter 3.4.1*. It is based on the Kriging process, in order to estimate the value of a function at given point through an interpolation of the closest known points. The difference between the method performed in the chapter 3.4.2 is the accuracy: in that method it was adopted a linear approximation, while now it was used a polynomial one.

For all the set of the unknown points investigated, the N closest points, found exactly with the same approach used in Kriging linear in *chapter 3.4.2*, are now grouped and used to generate a dynamic sixth-grade polynomial equation that express the system efficiency in function of the inlet parameters, in the form:

$$\eta_{unknown} = \eta_0 + \sum_{n=1}^{6} a_n \cdot {k_{ins}}^n + b_n * P^n + c_n \cdot D^n + d_n \cdot \#^n + e_n \cdot SL^n + f_n \cdot X^n \qquad (3.44)$$

Where:

$D, P, \#, SL, k_{ins}, X$ are the input variable of the unknown points

$a_n, b_n, c_n, d_n, e_n, f_n$ are the empirical coefficient determined by the dynamic multiple regression, obtained with the support of the Excel 2016® function LINEST

The fundamental difference of the equation 3.44 with respect to equation 3.50 is its dynamic nature: the empirical coefficients are found for each unknow point of the set and automatically updated.

The efficiency for the of the unknown points, which are the same that were picked for Kriging linear method, is evaluated also with the analytical method described in *chapter 3.2* and the results are compared with the approximated efficiency estimated with the *equation 3.45,* with the resulting errors:

$$\epsilon_{abs,unknown} = abs\ (1 - \frac{\eta_{unknown\ approx}}{\eta_{unknown,analytic}}\ ) \tag{3.45}$$

Where:

$\epsilon_{abs,unknown}$ is the absolute error in the estimation of the efficiency for the unknown point with the Kriging polynomial method

$\eta_{unknown\ approx}$ is the approximated efficiency for the unknown point found in the *equation 3.59*

$\eta_{unknown,analytic}$ is the analytical efficiency for the unknown point from the model described in *chapter 3.2*

The same set of unknown points (1000) considered in the Kriging linear method was used to validate the efficiency of this new approach. The average value of efficiency found for all the unknown points are showed in the *figure 3.21*, with different values of N selected.

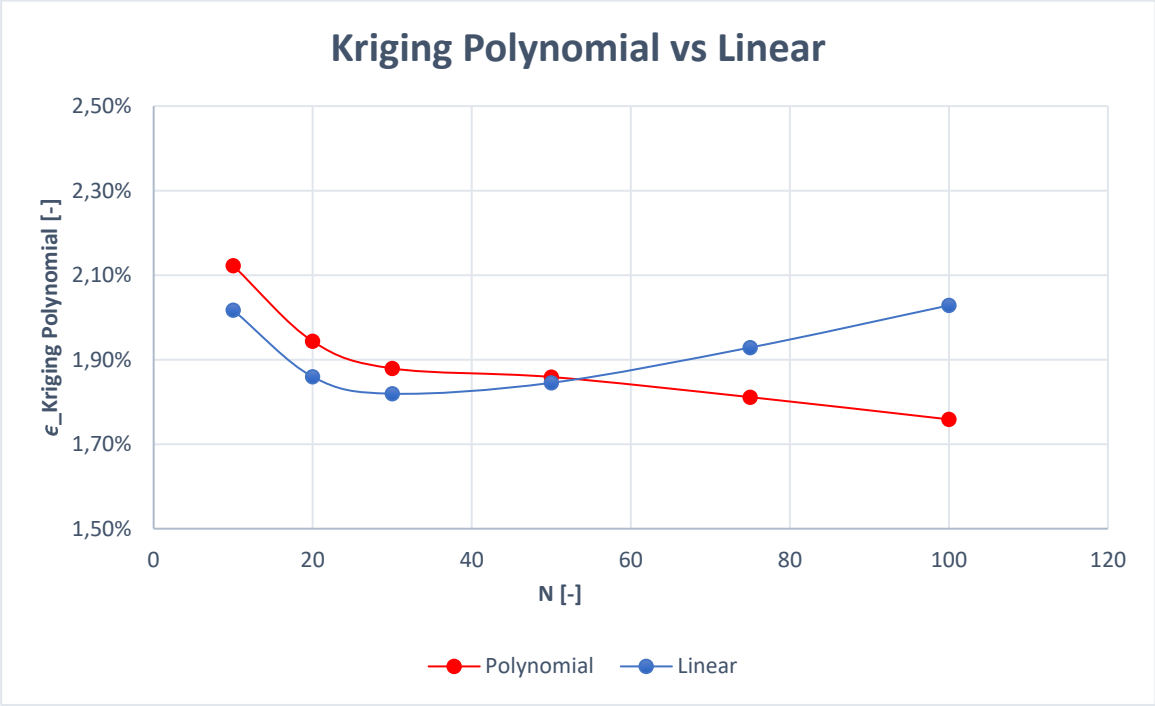

Figure 3-21:Error of the Kriging Polynomial approximation method, compared with the error found in the Kriging Linear method

For lower number of N, the Polynomial method is less efficient than the Linear, but from N higher than 50, its quality increases. For the conformity of the analysis, the range of N assumed

is the same, also if could be interesting an investigation of the performance of the Kriging Polynomial method with higher N, because it does not appear clear the presence of an optimum point, characterized by the minimum error.

4 Performance analysis of the CES with different heat storage materials

The most promising and the most widespread technology for the Cold Energy Storage, in a Cryogenic Energy Storage plant, remains the passive sensible heat storage. The energy, in form of high-grade cold is transferred by a heat transfer fluid to a heat storage material (HSM) and vice versa. In *chapter 2,* the study of existing plants or project about this technology suggest the use of quartzite or gravel material, for the low cost and the good thermal properties.

In this chapter they were taken into consideration different heat storage material and it was analysed the variation of the Cold Energy Storage system performances.

Three different types of HSM were presented, with different size:

- *Quartzite Gravel*: it is hard, metamorphic rock and its properties depends on its formation conditions. The samples used in this work are grouped in two different types, each with a characteristic shade of colours. Inside each type, the distribution of the size is very heterogeneous, and the estimation of the average diameter could be difficult or not precise.

Figure 4-1:Different size quartzite gravel samples. From the left, medium and small size

- *SiLibeads Typ S Glass*: it is a borosilicate, polished glass, made of soda lime glass. Its crushing strength is several times higher than natural quartzite gravel: it is composed of SiO_2 for 65-75%, Na_2O for 12-17% and for less than 10% of CaO, Al_2O_3 and MgO (51). Its external shape is very smooth but non-perfectly spherical, with a roundness of almost 95%.

Figure 4-2:Different size SiLi glass samples. From the left, large and small size

- *Pirex glass*: The Pirex 7740 is a borosilicate glass, used for most laboratory applications, because its high resistance at the change of temperature and at chemicals: has a low expansion coefficient and resists to a great mechanical strength. It is composed 80.6% of SiO_2, 13% of B_2O_3 and less 5% of Na_2O and Al_2O_3 (52). It is perfectly spherical, with a roundness of almost 99% and very smooth and transparent.

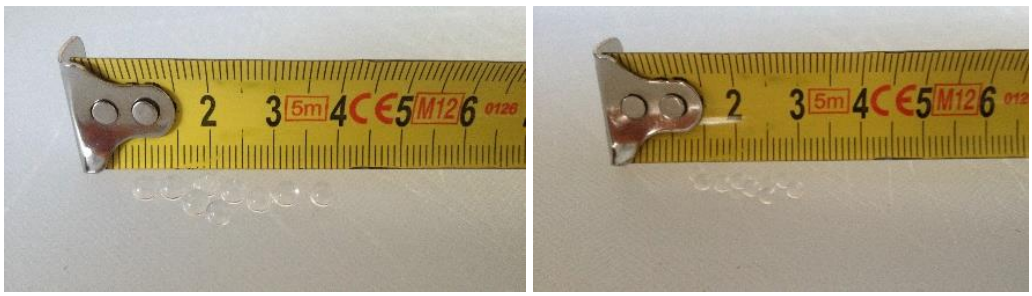

Figure 4-3:Different size PIREX glass samples. From the left, large and small size

The correct choice of the HSM is fundamental to avoid problems of integrity during the operation, to decrease the necessary maintenance and to enhance the system efficiency, considering also the economic aspect.

In the first part of the chapter was performed an experimental estimation of the fundamental characteristics of different material. Later, through some experiments, they were estimated the pressure losses across the HSM packed bed. The results obtained allowed to calculate the performances of the Cold Energy Storage for different HSM, with the analytical model proposed in the *chapter 3*.

4.1 Estimation of samples properties

The purpose of this part consists into find the value of the density, porosity and the average diameter for all different sample with a good approximation, to properly perform the experiments described in *chapter 4.2*.

4.1.1 Density: Experimental estimation

To measure the density of a sample, there were necessary some water, two precision balances and two test tubes: using two different instruments could reduce the error. The first test tube has a capacity of 2000 cm^3, with an accuracy of 20 cm^3, while the second one has a capacity of 50 cm^3 and a related accuracy of 1 cm^3: both are made with PIREX glass. The first precision balance has a maximum weight of 2 kg, while the second one only 1 kg: both have a precision of a tenth of a gram.

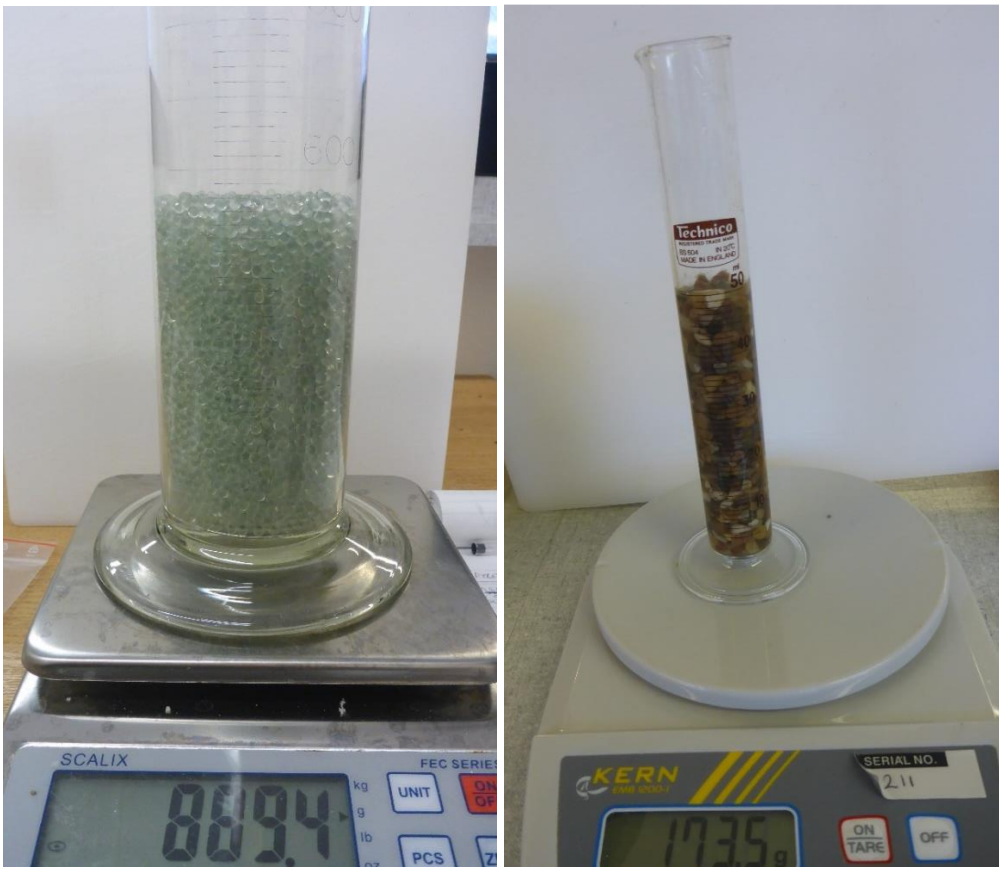

Figure 4-4:On the left: the first test tube and the first precision balance measuring the mass of the SiLi glass, small size. On the right: instruments measuring the mass of the large size quartzite gravel

The analysis is performed in some steps:

- Measure the test tubes tare with the precision balance: $m_{tare,1} = 973.7\ g$ and $m_{tare,2} = 77.9\ g$. From now on, it was assumed the use of only one test tube and one precision balance, to simplify the explanation

- Fill the test tube with the HSM sample analysed until its volume, called V_{tot}, could be easily estimated. The sample HSM mass is obtained from the measure the resulting weight:

$$m_{sample} = m_{tare+sample} - m_{tare} \tag{4.1}$$

- Fill the test tube with water at fixed temperature, until it reaches the level of the sample perfectly. The temperature of the water is important because it is necessary to know its density. Now it is necessary to measure the total weight m_{tot}
- Knowing the total weight, it is obtained the mass of the water (4.2) and knowing its density, it could be calculated also the volume (4.3)

$$m_{water} = m_{tot} - m_{tare+sample} \tag{4.2}$$

$$V_{water} = \frac{m_{water}}{\rho_{water}} \tag{4.3}$$

- Now, knowing the total volume and the mass of the sample estimated in the first step, it is possible to determinate the density of the sample HSM (4.5).

$$V_{sample} = V_{tot} - V_{water} \tag{4.4}$$

$$\rho_{sample,HSM} = \frac{m_{sample}}{V_{sample}} \tag{4.5}$$

The values in the *table 4.1* are the averaged value for the measurements performed with the two different test tubes. The expected density value is the same with the variation of the size for each HSM sample: the density has an error lower than 1%, so the reliability of this method could be confirmed.

Quartzite gravel		*SiLibeads Glass*		*Pyrex Glass*	
Small	Medium	Small	Large	Small	Large
2512,1	2454,5	2373,2	2394,3	2108,5	2126,8

Table 4-1:Density for different HSM samples with different size

4.1.2 Porosity: Experimental estimation

The porosity of a porous medium is defined as the ratio between the void in a fixed volume of HSM material and the same material. In this experiment it was estimated as the volume occupied by the water, as results from the *equation 4.3*:

$$\epsilon_{sample,HSM} = \frac{V_{water}}{V_{tot}} \tag{4.6}$$

It was possible to notice immediately the change of the porosity value related to each sample, by varying the dimension of the test tube: it is called sidewall effect. With a low diameter for the packed bed, the effect of the walls on the porosity could not be neglected. The diameter of the packed bed corresponds exactly with the two test tube, with diameters D_1= 7.67 cm and D_2= 2.39 cm. For the experiment on the pressure losses evaluation performed in the *chapter 4.2,* the packed bed is contained between two pipes, one with D_{est} =6.0 cm and the inner one with D_{int} =1.5 cm.

Considering a cylindrical pipe filled with a packed bed material, the corresponding equation to describe the ratio between its perimeter and its area is:

$$\frac{Perimeter}{Area} = \frac{4}{Diameter} \tag{4.7}$$

For a packed bed contained between two pipes, the equation 4.7 is still valid, but the total perimeter is the sum of the inner and the outer ones, while the total area is the difference between the outer pipe and the inner one. With this assumption, the resulted diameter of the

equivalent packed bed is D_{eq}= 4.51 cm. To adapt the values of porosity found with the test tube to the equivalent diameter, it was performed a linear interpolation and the results for each HSM samples are reported in *table 4.2*.

Quartzite gravel		***SiLibeads Glass***		***Pyrex Glass***	
Small	Medium	Small	Large	Small	Large
0,381	0,409	0,373	0,376	0,374	0,381

Table 4-2:Porosity for different HSM samples with different size, in a test tube of D=4.51 cm

4.1.3 Average diameter: Experimental estimation

To measure the average diameter of the sample used in this discussion, they were taken a sufficient number of particles of each type and, once their total volume is known, with the process described in chapter 4.1.1, they were counted, with the goal to estimate the average volume occupied by a single particle. Knowing the average volume of the single particles, their average diameters were calculated. They were considered more than thousand particles for each material, to have a sufficient number of samples and obtain a good estimation.

Quartzite gravel		***SiLibeads Glass***		***Pyrex Glass***	
Small	Medium	Small	Large	Small	Large
1.94	3.55	2.29	4.22	2.72	4.07

Table 4-3:Average diameters for different HSM samples with different size

For the SiLibeads and for the Pyrex Glass, the resulting average diameter could be considered very accurate, because their size distribution is very constant, while for the quartzite gravel there is a high level of dispersion, that is possible to see in the *figure 4.5*.

Figure 4-5:Different size distribution for the quartzite gravel, small size

4.2 Experimental evaluation of the pressure drops in a packed bed

One of the most critical terms of losses for the Cold Energy Storage system is represented by the pressure drop of the HTF across the HSM packed bed. Each material of different size is characterized by a certain permeability, that represents the capability of the porous media to allows the transit of fluid through it.

In this section they were compared the pressure drops for all the material introduced in the previous chapter. Furthermore, the experimental results were taken in comparison with the correspondent theoretical prevision estimated with the Ergun expression, found in the *equation 3.15*.

4.2.1 Description and physics of the experiment

It was selected a certain amount of material for each sample and packed in a cylindrical container. A water flow, with a certain speed, was passed through the packed bed of material: to measure the pressure drops due to the packed bed, it was sufficient to measure the difference of pressure of the water at the inlet and at the outlet of the bed.

On the system upstream, is placed a water container that ensure the maintenance of a constant hydrostatic head: it supplies the water to the bottom of the cylindrical container, where the inlet pipe is connected to a T-valve. One of the outlet of the valve is open and let the water flows into the container and passes through the HSM packed bed, while the second is connected to another pipe that bypass the packed bed and is not affected from the pressure losses. The top of the container is drilled, to allow the water flows out: both the top of the container and the bypass pipe are free surface points. The pressure difference is evaluated measuring the difference between the water level at the top of the drilled container and the level on the second pipe, as it is possible to notice in the figure 4.6.

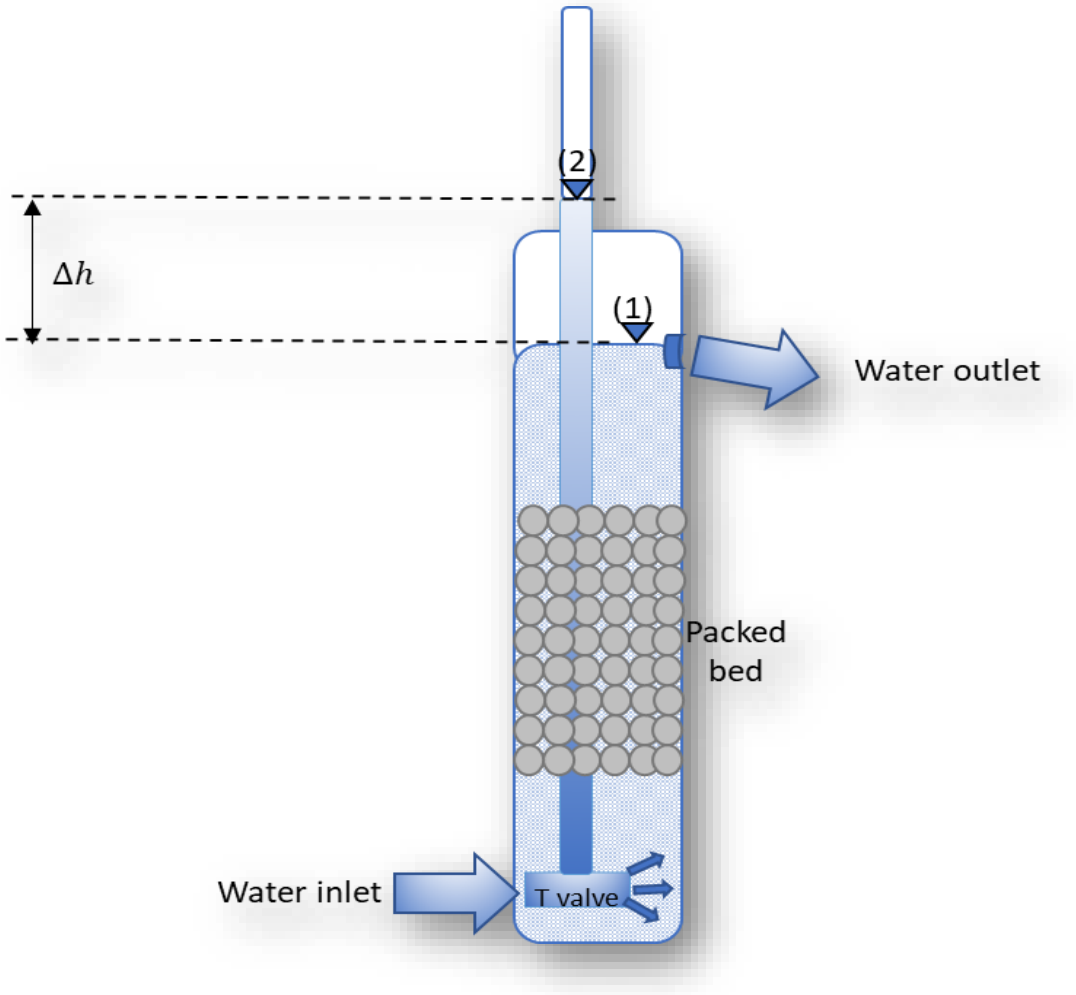

Figure 4-6:Simplified schematic representation of the system to estimate the pressure losses

For the fluid dynamic study of this system, it is necessary to apply the Bernoulli equation, with the hypothesis of uncompressible fluid, steady flow and no friction. In this expression, the term ∂p indicates the presence of pressure losses along the fluids path.

$$p + \rho \cdot g \cdot h + {}^{1}/_{2} \cdot \rho \cdot v^2 + \partial p = const \qquad (4.8)$$

Where

p is the absolute pressure of the fluid (Pa)

ρ is the fluid density (kg/m^3)

g is the universal constant for the acceleration of gravity (m/s^2)

h is the height of the fluid relative to a reference point(m)

v is the absolute speed of the fluid (m/s)

∂p is the pressure difference due to the different fluids paths (Pa)

This equation must be applied between the point (1), that represents the free surface of the water that passed through the bed and (2), which is the free surface of the water that by-passed the bed. The absolute fluid speed in both the points is null: to express directly the relation between their difference of height with their difference of pressure, the *equation 4.8* could be rewritten in:

$$\partial p_{packed\ bed} = \rho \cdot g \cdot \Delta h_{1\rightarrow 2} \qquad (4.9)$$

Where

$\partial p_{packed\ bed}$ is the fluid pressure drop due to the presence of the packed bed (Pa)

$\Delta h_{1\rightarrow 2}$ is the difference of height between the point 1 and 2 (m)

The accuracy of the estimation of the $\Delta h_{1\rightarrow 2}$, measured with a caliber, is considered of 1 mm of water column, that corresponds at 9.8 Pa, taking into consideration the density of the water at 11°C.

To increase the precision of the method used, a transparent plastic pipe is connected directly with the cylinder after the bed through a hole and is coupled with the extension of the pipe that by-passes the bed. The two transparent pipes are bounded to a rigid aluminium rod, inclined with a certain angle ϑ, where the distance $\Delta s_{1\to2}$ between the two levels of water is measured with a caliber. The angles selected in the experiments changed from 5.1° to 33.5°, so the corresponding height of the water column could be express as:

$$\Delta h_{1\to2} = \Delta s_{1\to2} \cdot \sin(\vartheta) \qquad (4.10)$$

Where

$\Delta s_{1\to2}$ is the distance of the water level between the point 1 and 2 (m)

$\Delta h_{1\to2}$ is the difference of height between the point 1 and 2 (m)

ϑ is the angle between the horizontal and the tilted aluminium rod (°)

The only exception is represented by the gravel samples small size: their pressure drops related to high water speed were too high to be evaluated in the actual layout with $\vartheta < 90°$. The ϑ selected in all the case allow an accuracy of the method between 0.85 to 5.4 *Pa.*

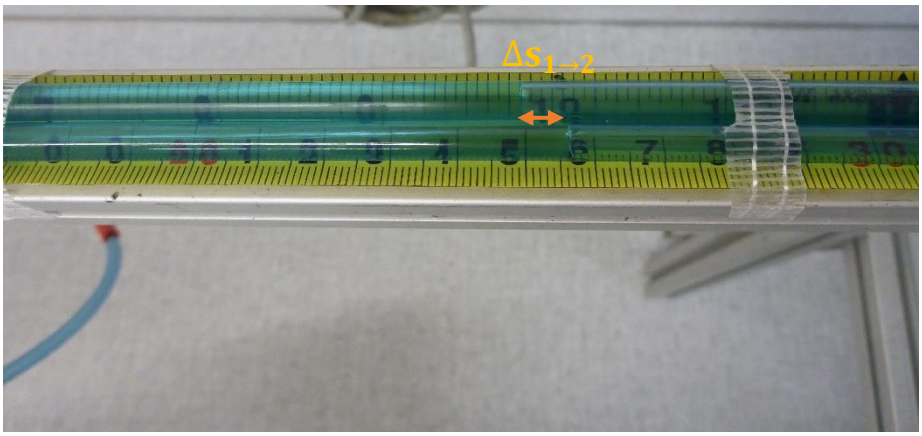

Figure 4-7:Difference of water level between the pipe connected with the cylinder at point 1 and the pipe by-pass of the packed bed, represented by point 2

The goal of the experiment described in this chapter is to investigate the relation between the pressure drops in a packed bed and the fluid velocity. It is possible to modify the fluid speed varying the height of the water container that drives the system, that ensures a constant

hydrostatic head. The fluid speed could be estimated by measuring the mass flowrate of the water that flows from the drilled top of the cylindrical container. The water is conveyed in a plastic container for an established time, that is measured with a chronometer and it is weighted with a precision balance, represented in the *figure 4.8*.

Figure 4-8:On the left: Water contained and precision weight. On the right: Chronometer

The final system layout is shows in the *figure 4.10*, where it was measuring the pressure drop for the medium size quartzite gravel. In this picture the water tank upstream of the plant was not showed but is linked to the system through the yellow rubber pipe lower left. As it is possible to notice, the quartzite gravel packed bed is mechanically sustained by a stainless-steel honeycomb layer at the bottom of the cylindrical container, showed on the left. Its duty is to avoid the medium particles downfall and let the fluid flows across it. Below the honeycomb layer was placed the T-valve, that represents a fundamental component of the system: it allows to divide the flow between the water flow across the bed and the pipe that by-pass it.

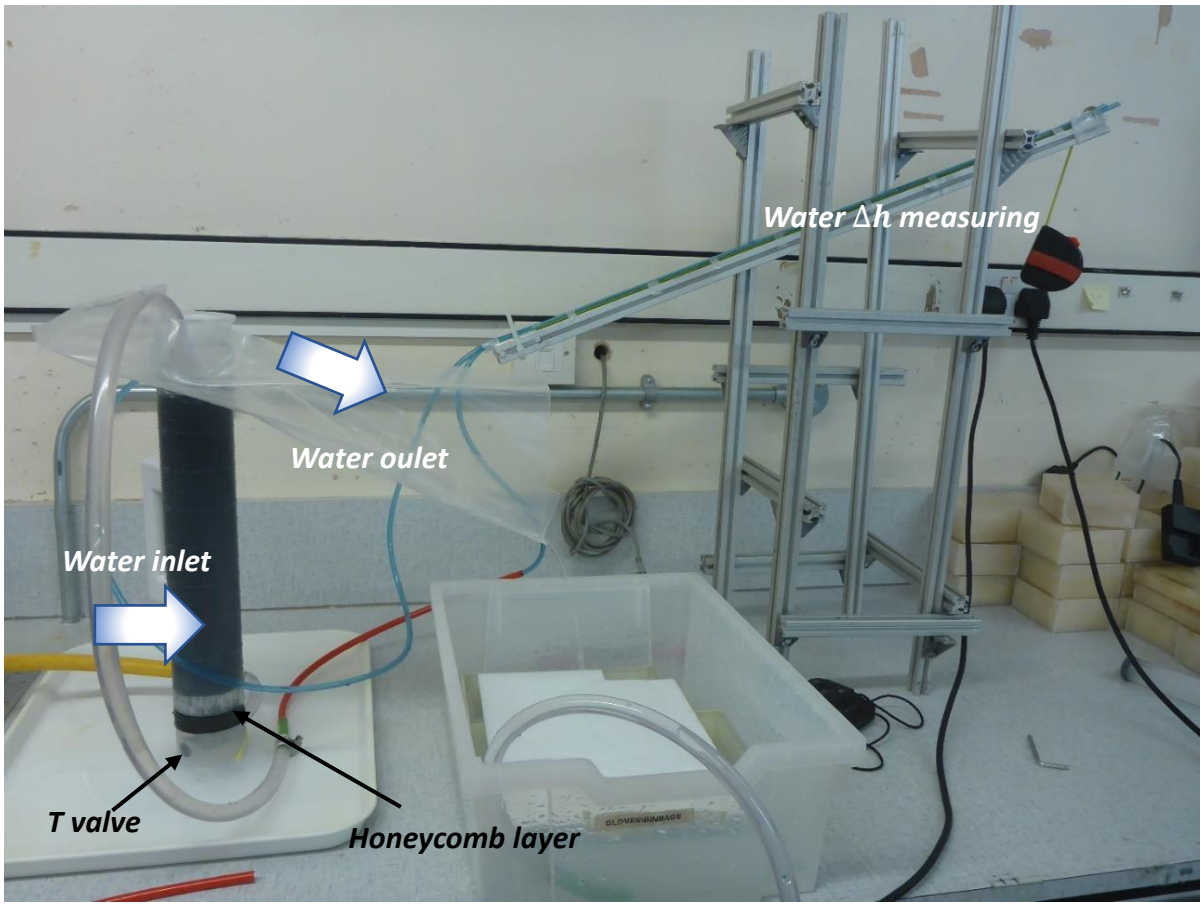

Figure 4-9:General system layout for the evaluation of a packed bed pressure drop

To ensure a sufficient accuracy in the evaluation of the water mass flow, for each pressure drop that corresponds to a specific fluid speed, it was used the average of five different measures. Moreover, the selection criterion for the time choice of each experiment, it was a sufficient mass of water inside the container, to decrease the error below the 5%.

One important point is due to the choice of the water speed range to perform the experiments: it is necessary to examine the conditions of a real cryogenic plant, with the purpose to simulate its physic. Assuming the use of nitrogen as HTF, the speed range, the temperature and pressure conditions discussed in the chapter 3, for this analysis they were considered their average values. The parameter that could be simulated is the Reynold number, because it includes all the parameters discussed. The table 4.4 shows the physical parameters to keep under consideration to evaluate the water speed range to perform the experiments: assuming a constant HSM particle diameter of 4 mm, the Reynolds number obtained is 317.2.

	$T\ (°C)$	$\rho\ (^{kg}/_{m^3})$	$\mu\ (Pa \cdot s)$	$u\ (^{m}/_{s})$
Nitrogen	-110	7.5	1.07E-05	0.050
Water	11	999.0	1.23E-03	0.096

Table 4-4:Physic properties for different HTF: Nitrogen is used in real cryogenic plants, water in this experiment

To simulate the real phenomenon, the average water speed that could be used is 96 mm/s: it was discovered that this value created some problem with the system layout built. For example, with higher water speed, the packed bed of particles tended to move, creating instability and wrong experimental results. It was decided to consider sufficient a water maximum speed of 0.02 m/s to maintain the packed bed fixed. The simulation could be considered still effective and reliable, because the Reynold number in real cryogenic situation has the same order of magnitude with respect to the experimental.

4.2.2 Experimental results

In this section are compared the results of the experiments to evaluate the pressure drops in a packed bed for three different HSM samples: Pyrex glass, SiLibeds and Quartzite gravel. The pressure drops reported are expressed in $^{Pa}/_{m}$, because the length of the packed bed selected is different for each material. For the Silibeds and for the Pyrex glass, the bed length is 21.5 cm, for the medium size quartzite gravel is 26 cm, while for the small and large size is chosen 20.2 cm. This choice was imposed by the system layout and by the availability of material for each sample.

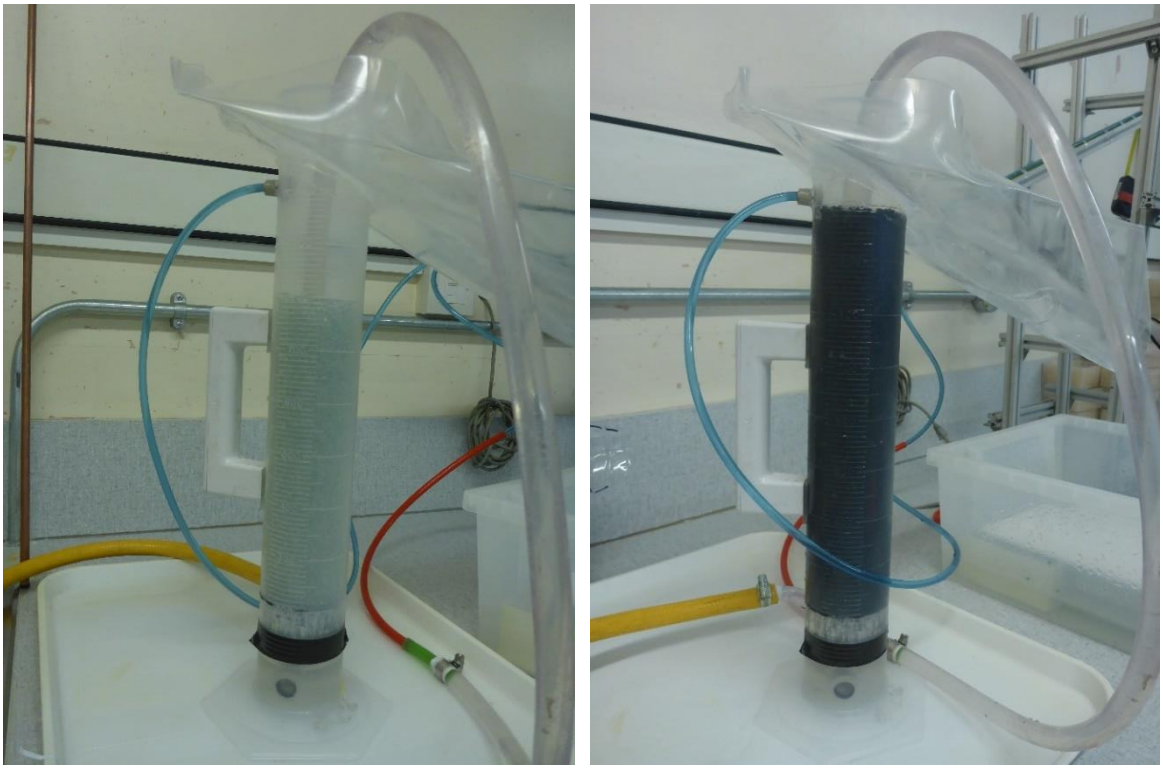

Figure 4-10:Packed bed for SiLibeads on the left, quartzite gravel on the right

In the *figure 4.11* is presented the behaviour of the different material pressure drops, in function of the water speed across the packed bed. According with the Ergun law's, the pressure drops grows in relation with u and u^2: at low regimen it appears more evident a linear behaviour, that became more quadratic with the increasing at low speed, that it becomes more quadratic with the fluid speed increasing. They are reported, with different colours for each type, the experimental point recorded: the different scale of grey represents the quartzite gravel, the greens the Pyrex glass and with different shades of orange is represented the SiLibeds. The first impression highlighted the expectations: the quartzite gravel samples, that represents the roughest and the less rounded material, accounted the highest pressure drops, as opposed to the Pyrex spheres. The samples size is fundamental, mostly for the roughest material: a lower average diameter means lower pressure drops.

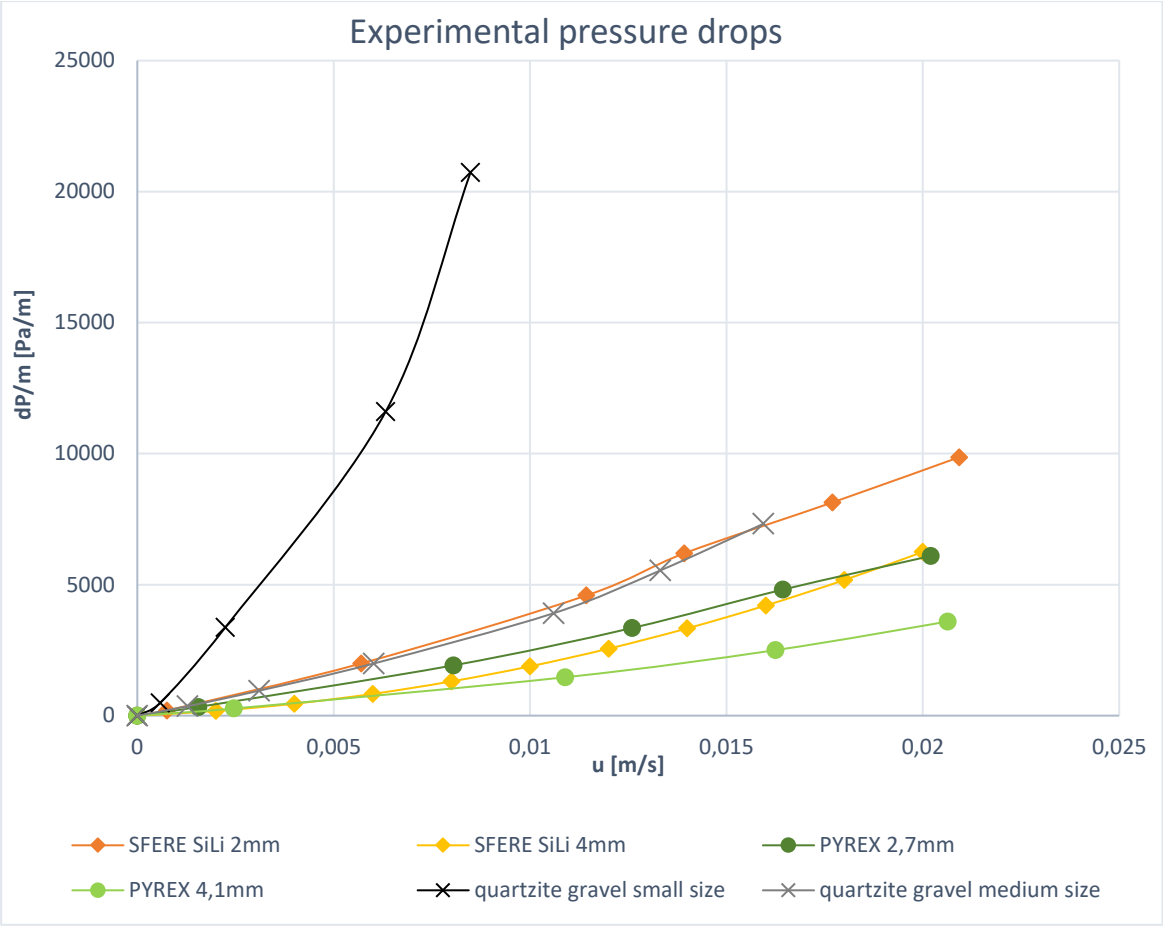

Figure 4-11:Experimental pressure drops for different HSM samples with water as HTF

The experimental results are then compared to the corresponding theoretical behaviour expressed by the Ergun's law, if it were valid the assumption of perfect spherical shape and constant particle diameter. Considering the system layout described in the chapter 4.2.1, it is necessary a setup calibration that involved the estimation of the pressure losses due to the honeycomb layer, represented in the *figure 4.12*. This contribution must be excluded to obtain a more accurate comparison.

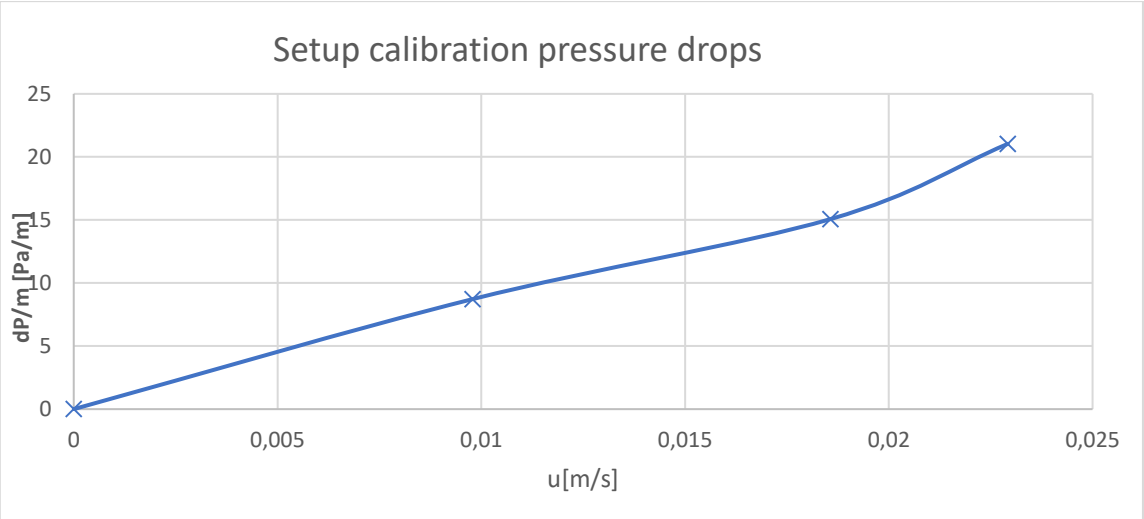

Figure 4-12:Setup calibration: Pressure drops due to the honeycomb layer

With respect to the order of magnitude of the pressure losses due to the packed bed of HSM, the influence of the honeycomb layer is negligible.

From the *figure 4.13* to the *figure 4.19* is presented the behaviour of the water pressure drops across different material packed bed, in function of the fluid velocity. The consistency of the results is demonstrated through the comparison of the experimental data trend with the theoretical pressure losses described by the Ergun's law. The crosses report the specific points recorded through the experiments and their distribution along the speed range selected is not perfectly homogenous for a setup limit: the regulation of the speed through the hydrostatic height variation was not very modular.

In each chart are represented in blue the pressure drops due to the presence of honeycomb layer, in red the analytical trendline for the experimental pressure drops, gross of the setup calibration and in yellow the net ones. The net pressure losses are estimated by the *equation 4.11*:

$$\partial p/_{m_{net}} = \partial p/_{m_{experimental}} - \partial p/_{m_{setup\ configuration}} \qquad (4.11)$$

Where

$\partial p/_{m_{net}}$ is the pressure drops at the net of the honeycomb layer (Pa/m)

$\partial p/_{m_{experimental}}$ is the pressure drops trendline obtained by experimental results (Pa/m)

$\partial p/_{m_{setup\ configuration}}$ is the pressure drop trendline due to the setup configuration (Pa/m)

Figure 4-13:Pressure drops: experimental and theoretical comparison for SiLibeds large size

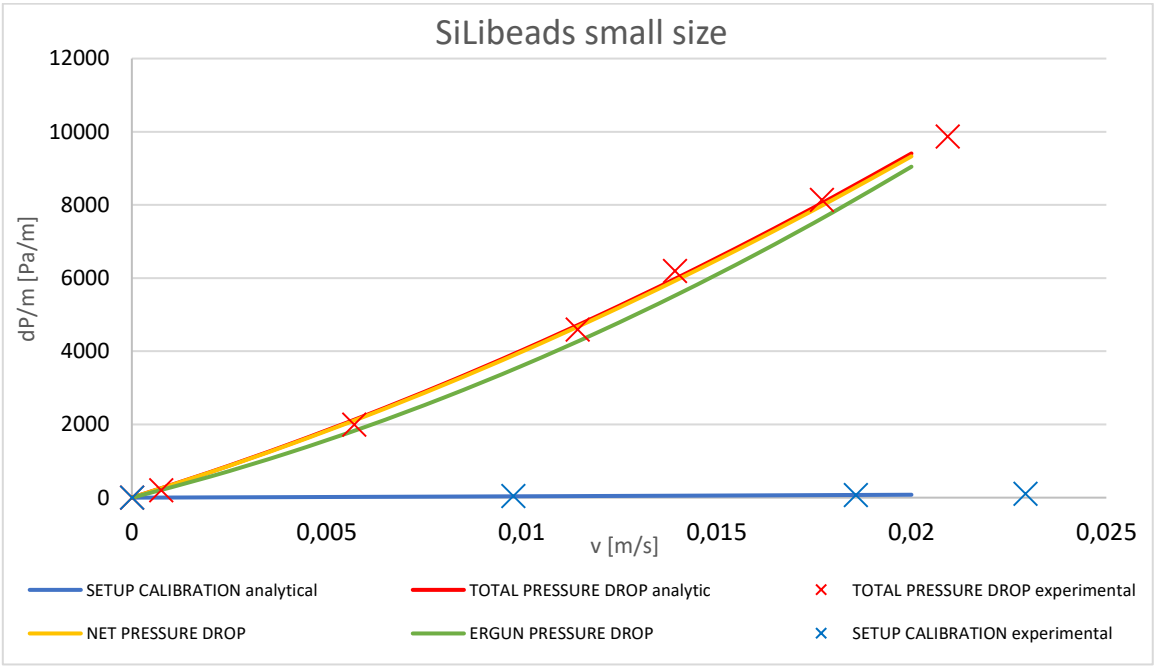

Figure 4-14:Pressure drops: experimental and theoretical comparison for SiLibeds small size

Figure 4-15:Pressure drops: experimental and theoretical comparison for Pyrex glass large size

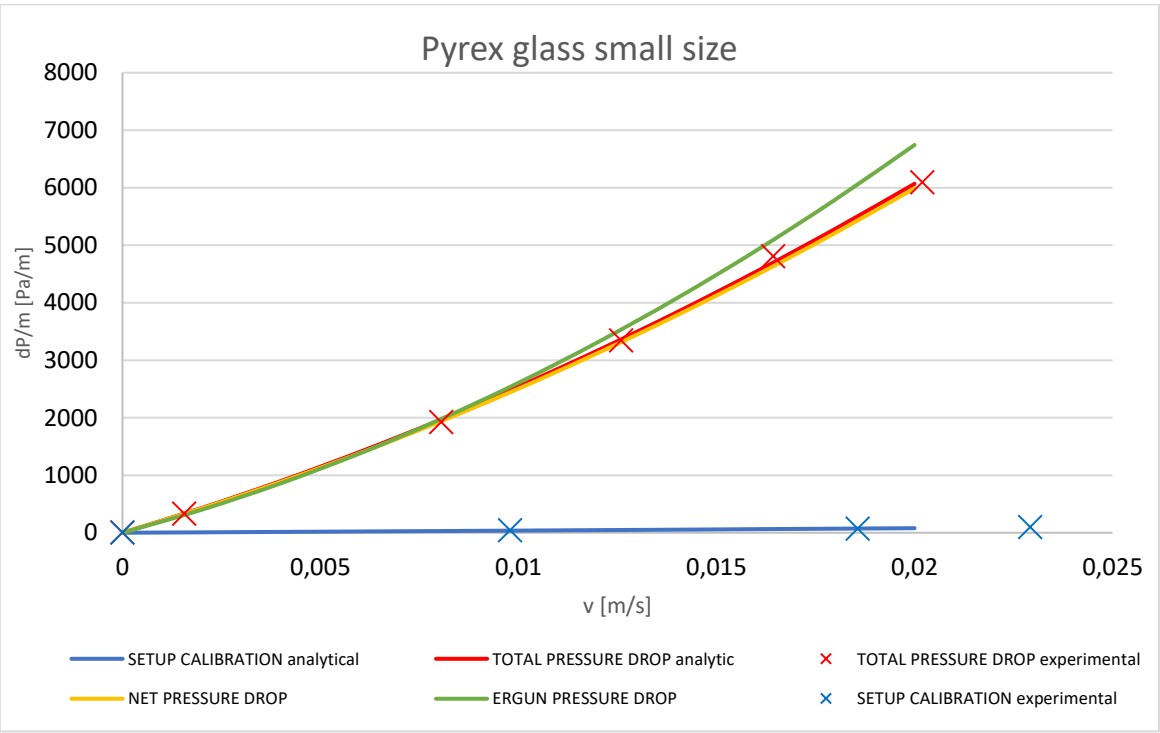

Figure 4-16:Pressure drops: experimental and theoretical comparison for Pyrex glass large size

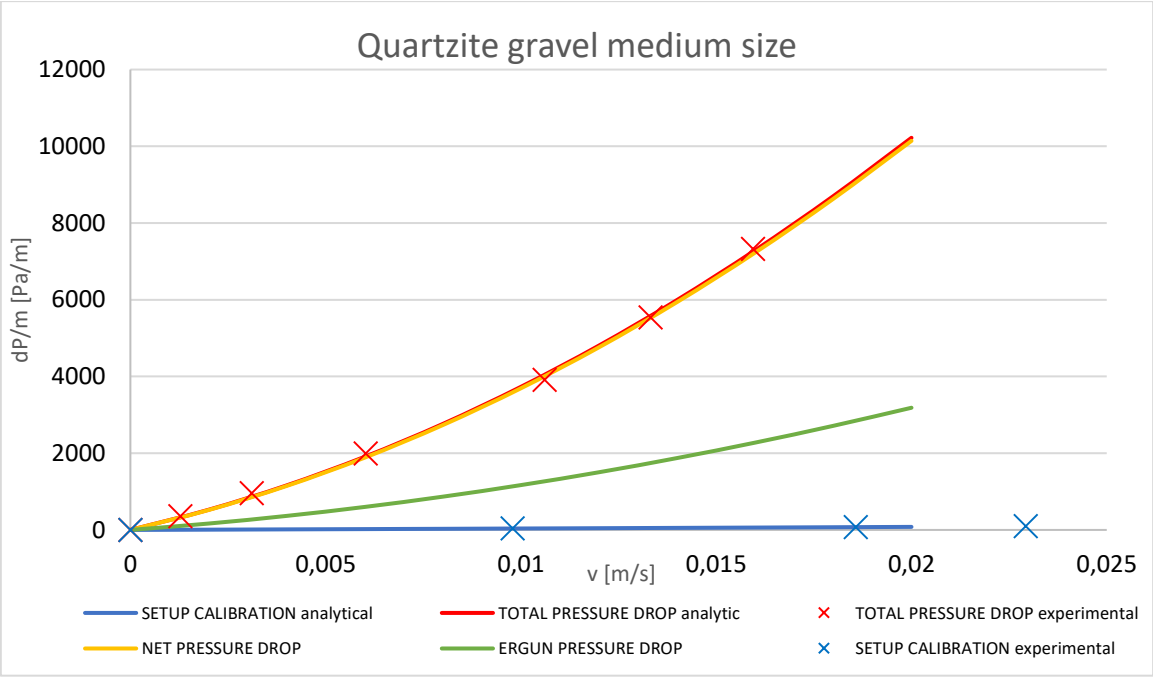

Figure 4-17:Pressure drops: experimental and theoretical comparison for Quartzite gravel medium size

The water speed range in the *figure 4.18* is experimentally limited at 0.01 m/s instead 0.02 m/s, because the stability of the packed bed consisting of quartzite gravel was compromised at higher value.

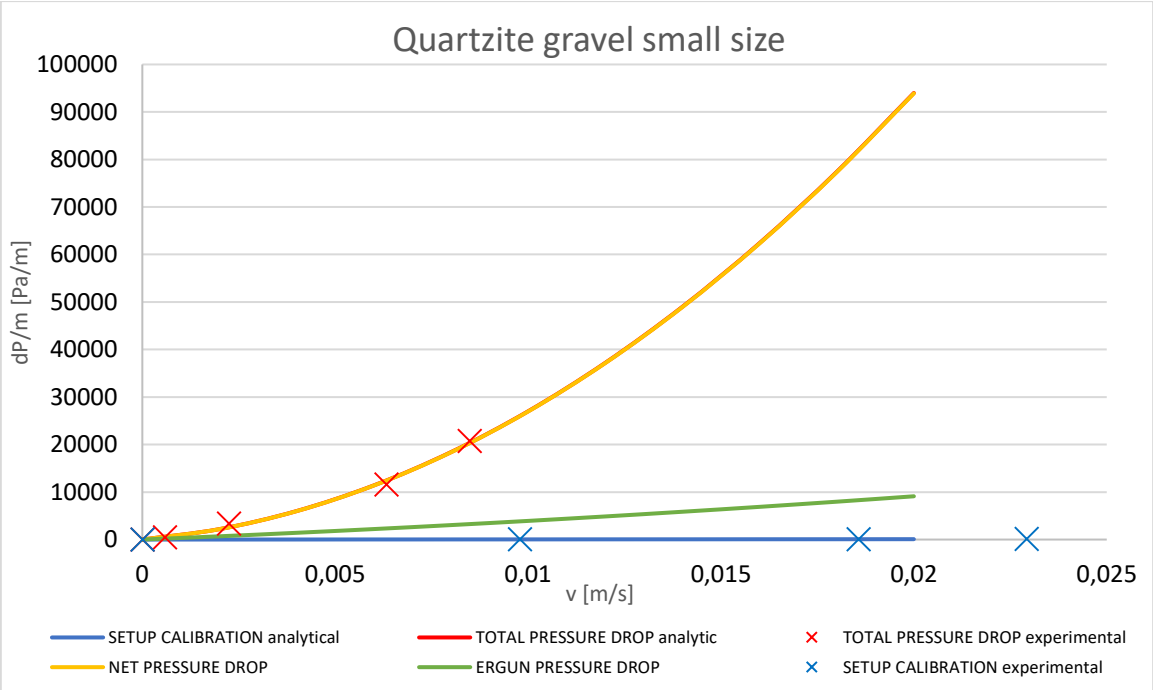

Figure 4-18:Pressure drops: experimental and theoretical comparison for Quartzite gravel small size

To prove the validity of these experimental results, are taking into consideration the values for Pyrex glass packed beds, to compare them with the theoretical results obtained with the Ergun's law, because these particles have a roundness > 99% and their surface is very smooth, so they are very similar to the ideal conditions. The absolute error between the two curves, expressed by the equation 4.5, estimate the goodness of the method used for the experiments: its value is 3.3% for the large size and 6.2% for the small size, that could be considered optimal.

$$\epsilon = abs(1 - \frac{\partial p/_{m_{net}}}{\partial p/_{m_{Ergun}}}) \qquad (4.12)$$

Where

ϵ is the absolute error of the experiment performed (Pa/m)

$\partial p/_{m_{net}}$ is the net pressure drops estimated in the experiment (Pa/m)

$\partial p/_{m_{Ergun}}$ is the pressure drop estimated with the Ergun's law (Pa/m)

The SiLibeads material is characterized by a roundness nominal value 0.95, so its experimental behaviour with respect to the theoretical results for the pressure drops is more different than Pyrex glass: from the *figure 4.13*, the difference between them became more significant with increasing water speed and it is more evident for the large size samples.

For the quartzite gravel samples, smaller the size, higher is the difference of the data recorded respect to the Ergun's law: as was introduced in the *chapter 4.1.3*, the average size distribution and the external shape of the gravel makes impossible a significant comparison.

4.3 Cold Energy Storage system with different HSM

In this section, it was evaluated the Cryogenic Energy Storage system efficiency described in *chapter 3,* varying the HSM according to the experimental results obtained in *chapter 4.2.* It was necessary to find a method to extract the results obtained experimentally, where the HTF

across the HSM packed bed was represented by the water and used them to simulate the process in a realistic configuration with the nitrogen.

4.3.1 Experimental pressure drop estimation: model for a generic HTF

To adapt the experimental pressure drop results for a generic HTF, the analysis started studying the Ergun's law: in the theoretical approach outlined in the *equation 3.15*, it is possible to notice two empirical coefficients, one related linearly with the HTF speed (150) and the other quadratically (1.75). The idea is to extract, for each sample and for each size, these empirical coefficients. With a linear regression, the net pressure drops found through the *equation 4.9,* were expressed in the form:

$$\frac{\Delta P_{exp,net}}{L}(u) = \ C_1 \cdot u + C_2 \cdot u^2 \tag{4.13}$$

Where

$\frac{\Delta P_{exp,net}}{L}$ is the empirical coefficient to be found related linearly with HTF speed (-)

C_1 is an empirical coefficient related linearly with water speed (-)

C_2 is an empirical coefficient related quadratically with water speed (-)

u is the speed of the water in the experiment (m/s)

Comparing that expression with the Ergun's, it was assumed:

$$C_1 = a \ \cdot \frac{(1-\varepsilon)^2}{\varepsilon^3 \cdot d^2} \cdot \mu \tag{4.14}$$

$$C_2 = b \ \cdot \frac{(1-\varepsilon)}{\varepsilon^3 \cdot d} \cdot \rho \tag{4.15}$$

Where

a is the empirical coefficient to be found related linearly with the generic HTF speed (-)

b is the empirical coefficient to be found related quadratically with the generic HTF speed (-)

ε is the porosity of the HSM sample (-)

d is diameter of the HSM sample (m)

μ is the dynamic viscosity of the HTF (Pa·s)

ρ is the density of the HTF (kg/m^3)

Knowing the physical properties of density and dynamic viscosity for the water at the temperature of the experiments and knowing the geometrical properties of average diameter and porosity for each sample, the empirical coefficients *a* and *b* are extracted from the equation 4.7 and 4.8 and listed below:

	a (-)	***b (-)***
Ergun equation 3.15	***150***	***1.75***
Silibeds, small size	185,036	1,283
Silibeds, large size	118,790	4,45
Pyrex glass, small size	161,012	1,109
Pyrex glass, large size	166,727	1,470
Quartzite gravel, small size	306,624	34,723
Quartzite gravel, large size	465,734	5,695

Table 4-5:Empirical coefficients to describe the pressure drops for each sample

The empirical coefficient found reflected the expected trend: for the Pyrex glass, *a* and *b* are very close to the Ergun's and the quartzite gravel showed very higher values: its small size sample show a quadratic component that is one order of magnitude higher than others. These empirical coefficients could be used for any HTF fluid.

4.3.2 Performance analysis in realistic configuration with different HSM

The purpose of this chapter is to estimate the efficiency of the system due to the different HSM proposed in the experimental tests, through the analytical model proposed in the *chapter 3*. The choice of the HSM is fundamental for the efficiency of the Cold Energy storage system: in the first model analysed, the assumption of using a perfectly spherical and smooth material (with the parameter X=0), rather than using the quartzite gravel proposed (with the variable X=1), have a high influence in terms of overall system efficiency, causing a reduction of 5/10% in average. The variables of the system that are not affected from the type or from the dimension of the HSM, were determined with the criteria of the best trade-off between best performances and best feasibility. Through the parametrical analysis, it appears clear an improvement of the system efficiency with the increasing of the inlet HTF pressure and the value chosen was 3 bar, because higher pressure means thicker pipes and vessel. The number of HSM layers in series decided is 2: this ensures low pressure losses than a single one, for the possibility of partial by-pass through a valve and not too high cryogenic vessel, that could cause structural and transportation problems. This definition of number of layer makes the best choice available the slenderness of the vessel around 2.5, as is possible to determine in the *figure 3.14* and *3.15*. The last variable to be fixed in the model is the insulation thermal conductivity: from the parametric analysis it is evident its importance, that justifies high cost to have the better insulation proposed. These parameters are summarized in the *table 4.6.*

Final Cold Energy Storage layout

Inlet HTF pressure (bar)	*Number of HSM layers in series (-)*	*Cryogenic vessel slenderness (-)*	*Insulation thermal conductivity (W/mK)*
3	2	2.5	0.01 (53)

Table 4-6:Final Cold Energy Storage layout

The remaining parameters to be evaluated as variables are the average HSM diameter and the pressure drop associated with each different HSM material proposed in this analysis, that are evaluated from the experimental results, expressed through the empirical coefficients in the *table 4.5.* Using the physical properties of nitrogen as HTF, in the temperature and pressure

condition described on the table 4.4, the resulting trends for the real case of nitrogen is presented in the figure 4.19.

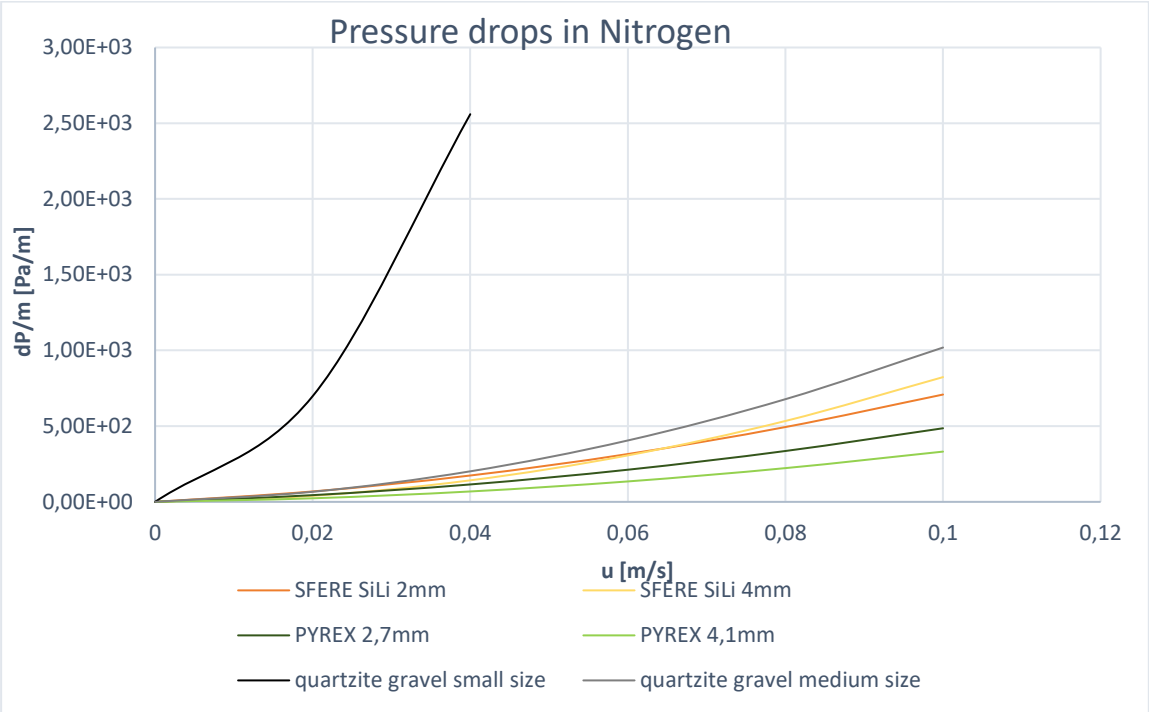

Figure 4-19:Analytical estimation of pressure drop due to different HSM with Nitrogen as HTF from experimental evaluations

The trend of the curves is very similar to the pressure drop evaluated experimentally with the water as HTF, but the nitrogen speed range is different: for the high values, the pressure losses with the Silibeds became more consistent with higher size, because the quadratic coefficient *b* is more influencing. The maximum value investigated of the nitrogen speed is almost the double of the average speed determined in the analytical model, using the inlet HTF pressure declared in the final layout.

Comparing the pressure drops obtained experimentally in this chapter respect to those evaluated analytically with the model described in *chapter 3*, it could be interesting to discover the value of the variable X ratio related to the pressure drops of the different HSM. Extracting the X from the *equation 3.29:*

$$X = \frac{\frac{\Delta P}{L} - \frac{\Delta P_{Ergun}}{L}}{\frac{\Delta P_{Exp}}{L} - \frac{\Delta P_{Ergun}}{L}} \tag{4.16}$$

Where:

$\frac{\Delta P}{L}$ is the pressure drop obtained in the mixed approach (Pa/m)

$\frac{\Delta P_{Ergun}}{L}$ is the pressure drop obtained by the theoretical approach (Pa/m)

X is relate to the shape of the HSM selected (-)

$\frac{\Delta P_{Exp}}{L}$ is the pressure drop obtained with the gravel used in *chapter 3* (Pa/m)

The Pyrex glass behaviour reflects the validity of the Ergun law for a well-rounded HSM: with a roundness of almost 99% the Ergun law it was replicated experimentally with an average error lower than 5%. The negative value of the X parameter assumed for the Pyrex glass have not a physical meaning, but are due to a margin of error of the experimental method

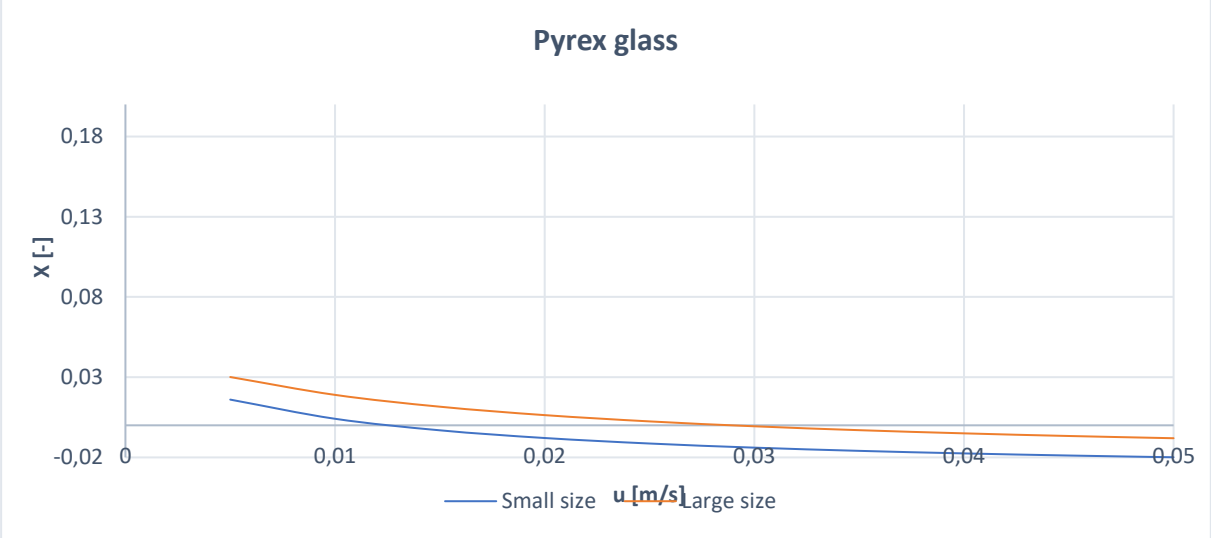

Figure 4-20:X ratio for the Pyrex glass

.

For the SiLibeds glass and for the quartzite samples, the X values achieved became more relevant: they were represented in function only of the HTF speed, in the figure 4.21 and 4.22. As it was possible to expected, the quartzite gravel used in this experimental analysis reached value of X ratio very close to 1, with an average value of 0.67. On the contrary the value of the

X ratio evaluated for the SiLibeds glass was 0.06, confirming its better shape of almost 0.95 of roundness.

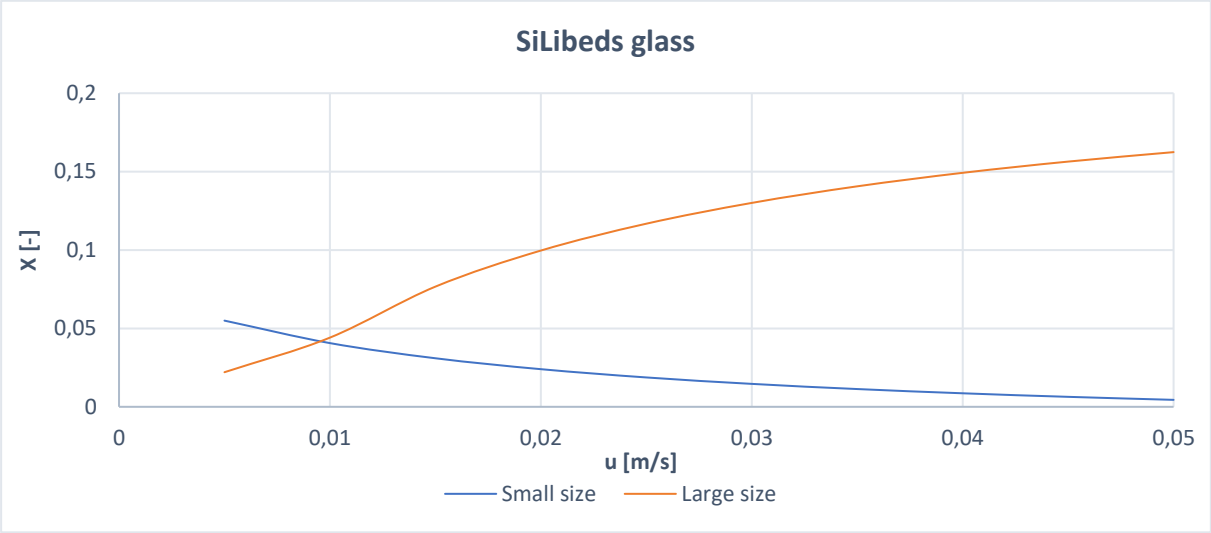

Figure 4-21:X ratio for the SiLibeds glass

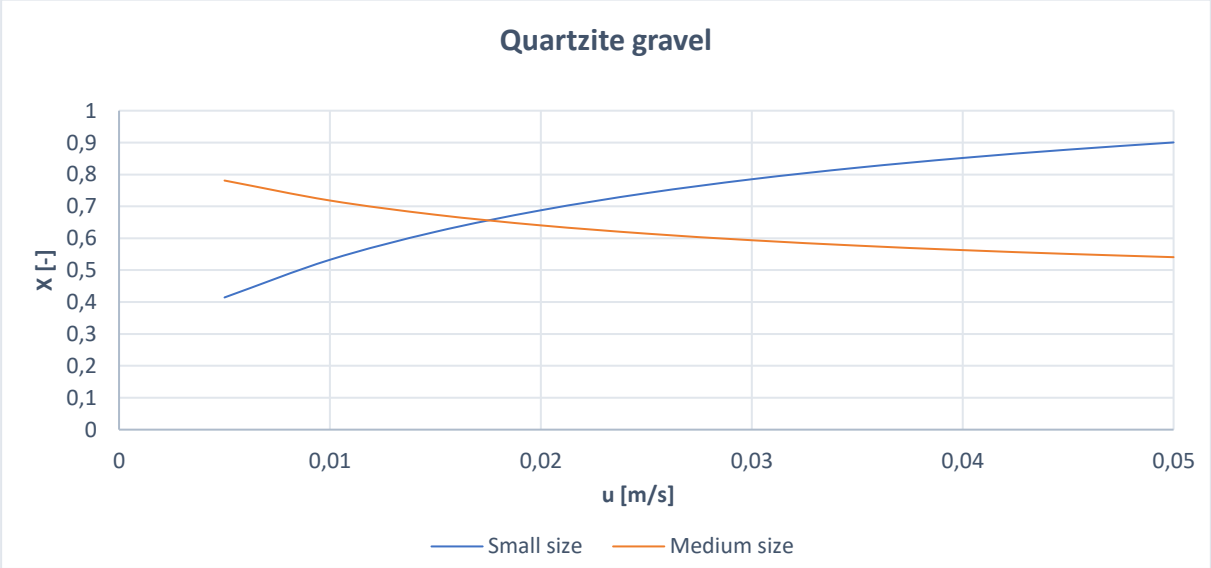

Figure 4-22:X ratio for the Quartzite gravel

Before to compare the efficiency of the Cold Energy Storage system described in the *chapter 3,* with the different HSM, it was necessary to declare their heat capacity, in cryogenic conditions, evaluated at the temperature of 170 K, (54), (55), (56):

Material	*Cp (kJ/kgK)*
Pyrex glass	0.507 (54)
Silibeds glass	0.512 (55)
Quartzite gravel	0.468 (56)

Figure 4-23:Cp of different HSM in cryogenic conditions

For the different HSM proposed in the analysis in the *table 4.7* were defined some fundamental parameters, such as the pressure drop due to the packed bed and the Cold Energy Storage Efficiency, defined according to the equation XX. Furthermore, the first hypothesis for the construction of the real plant was the adoption of the quartzite gravel medium size, so it was evaluated an indicator to compare the improvement reached with the use of others HSM.

Cold Energy Storage Efficiency with different HSM

Material	*Fan Power (W)*	*Comparison of Fan Power* (W)*	*Round-Trip Efficiency (%)*	*Comparison of efficiency* (%)*
Quartzite gravel - Small size	2735.5	+425%	85.74	-6.00%
Quartzite gravel - Medium size	521.5	-	91.22	-
SiLibeads – Small size	483.1	-7%	92.02	+0.88%
SiLibeads – Large size	475.9	-9%	91.14	-0.08%
Pyrex glass – Small size	429.2	-18%	92.00	+0.85%
Pyrex glass – Large size	389.6	-25%	91.44	+0.24%

Table 4-7:Cold Energy Storage Efficiency final layout with different HSM

*comparison with quartzite gravel, medium size

Despite the increase of the pressure drops when the size of the HSM decrease, the efficiency of the system for the glass materials is slightly better at smaller size, because the heat exchange is more effective, and the thermocline is thinner. The quartzite gravel is excluded from this

consideration, because the pressure losses associated to the small size have one order of magnitude more than the others, so that contribution remains the prevailing. Considering purely the performances, between the materials proposed, the best option are the SiLibeds glass with an average diameter of 2.29 mm and Pyrex glass with diameter of 2.72 mm.

It was necessary to explicit some consideration of the economical point of view for the different HSM: the purchasing cost of the Pyrex glass, as reported in the *table 4.8*, represents an enormous drawback, because is one order of magnitude bigger than the other. For this reason, it was necessary to exclude it from a further analysis performed in the chapter 5, considering that its performances are very similar to the Silibeds glass, both in terms of pressure losses and of Round-trip efficiency.

Material	*Price (€/ton)*
Quartzite gravel - Small size	*320* (57)
Quartzite gravel - Medium size	*180* (58)
SiLibeads glass – Small size	*1˙085* (59)
SiLibeads glass – Large size	*1˙195* (59)
Pyrex glass – Small size	*˜25˙000*
Pyrex glass – Large size	*˜25˙000*

Table 4-8:Gross price for different HSM material

5 Thermal resistance for different HSM

A further analysis concerned the different HSM was developed in terms of thermal resistance: in a real cryogenic system, the material particles must be subjected to thermal cycles: 2 times for each day their temperature changes from -50°C (223 K) to -168°C (105 K). The goal of this chapter is to simulate the thermal fatigue to which they are subjected, to understand which material, among which proposed in the *chapter 4,* is more resistant.

After the economic consideration that brought the Pyrex glass out from this analysis, also the small sized Quartzite gravel was excluded, consideration due to its impressive low efficiency showed in the *table 4.7*. From literature, the quartzite is very widely used for cryogenics application: that experimental study wants to compare its effectiveness, in terms of thermal behaviour, with respect to a glass material, represented by the SiLibeds.

The idea is to perform an accelerated thermal stress for each sample: a particle was heated up to a certain temperature and then cooled down, for a N number of times, until it broke. It is supposed that a packed bed of HSM should not break for the entire life of the plant, almost 20 years, so the heat transfer mechanism needs to be enhanced during the experiment.

The parameter chosen to evaluate the entity of the heat transfer mechanism was represented by the $^{dT}/_{t}$, parameter that indicates the instant variation of the particle temperature. The value of this parameter for the real situation is obtained from some considerations: in the real configuration, the average thermocline thickness, obtained from the *equation 3.36,* has a length of 0.16 m, and divides two parts of the storage at different temperature, one side at 105 K and the hot side at 223 K. From the final layout of the Cold Energy Storage presented in *table 4.6,* the average speed for the nitrogen in the packed bed was almost 0.055 m/s: the HSM particles inside the thermocline changed their temperature with a $\frac{dT}{t}_{ave}$ of 42.4 K/s, resulted from the *equation 5.1*:

$$\frac{dT}{t}_{ave} = \frac{dT}{\Delta x_{thermocline}/v_{HTF}} \tag{5.1}$$

Where

$\frac{dT}{t}_{ave}$ is the average particle instant temperature variation (K/s)

dT is the average temperature difference between the hot and the cold side of the storage (K)

$\Delta x_{thermocline}$ is the average thermocline thickness (m)

v_{HTF} is the average HTF speed across the packed bed (m/s)

The purpose of the model presented in this chapter is to evaluate the number of thermal cycles whose samples resist, at different $^{dT}/_{t}$. In the real mechanism, the HTF moves with a certain speed along the packed bed material, while in that experiment the idea is to have a fix fluid bath with a single particle of sample material that moves inside it. In fact, the important parameter to be consistent is represented by the relative speed and the relative acceleration between the fluid and the particle or vice versa.

The model described in *chapter 5.1* was created to simulate the thermodynamic of the heat transfer of a particle sample that moves inside a fluid bath and be cooled down. The results achieved with this study allows to know the $^{dT}/_{t}$ for the particle side that corresponds to each dT between the fluid and the particle itself. Considering the temperature of the fluid bath constant, with this model could be reached the direct correlation between the initial temperature of the particle with the maximum $^{dT}/_{t}$.

5.1 Simulated heat transfer model

To simulate the heat transfer of a fluid in a packed bed of HSM, it was adopted an analytic model that follows the behaviour of a single particle, for each temporal step, when moves in a fixed temperature liquid. The model needs to reproduce the fall of a hot sphere, that is dropped from a certain distance above a bath that contains a cold liquid, enters in it and moves until the bottom. At the beginning the particle is subjected to an acceleration in air, until reaches the surface of the liquid, where it decelerates until reach a stationary speed. The path travelled by the hot particle along the cold bath that contains the liquid is long enough to let the particle reach the stationary speed and temperature conditions.

5.1.1 Definition of the physics

The first part of this model studied involved its dynamic: the material sample is physically represented by a solid sphere, that moving across a medium is subjected to different forces. It was assumed necessary to evaluate the contribution of the gravitational force, related to the gravitational acceleration of a body in the atmosphere, the buoyancy force, exerted from the fluid to the solid and the drag force, that considers the shape of the solid and the viscosity of the fluid.

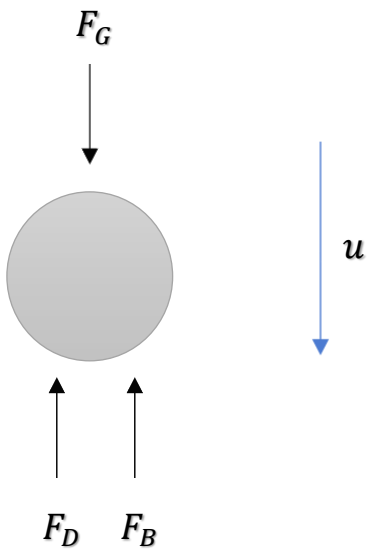

Figure 5-1:Dynamic representation of a particle immersed in a medium

The entity of the forces considered in this analysis are expressed from the *equation 5.2* to the *equation 5.4*.

$$F_G = m_p \cdot g \tag{5.2}$$

Where

F_G is the gravitational force (N)

m_p is the mass of the particle (kg)

g is the gravitational acceleration (m/s^2)

$$F_D = \frac{1}{2} \cdot C_D \cdot \rho_M \cdot A_p \cdot u_p \quad (5.3)$$

Where

F_D is the drag force (N)

C_D is the drag coefficient (-)

ρ_M is the medium density (kg/m^3)

A_p is the cross sectional area of the particle (m^2)

u_p is the particle speed (m/s)

$$F_B = g \cdot \rho_M \cdot V_p \quad (5.4)$$

Where

F_B is the buoyancy force (N)

g is the gravitational acceleration (m/s^2)

ρ_M is the medium density (kg/m^3)

V_p is the volume of the particle immersed inside the medium(m^3)

The sum of the forces that acts to the spheres are related to its acceleration through the *equation 5.5*: the motion became stationary when the forces are perfectly balanced.

$$\sum F = F_G - F_D - F_B = m_p \cdot a_p \quad (5.5)$$

Where

F_B is the buoyancy force (N)

F_D is the drag force (N)

F_G is the gravitational force (N)

m_p is the mass of the particle (kg)

a_p is the acceleration of the particle (m/s^2)

The most critical parameter to estimate is the drag coefficient C_D, parameter that represents the resistance to motion for a solid in a fluid. It is function of the Reynolds number, so it depends indirectly from the characteristics of both fluid, thought its density and its dynamic viscosity, and particle through its diameter and its speed. To evaluate the drag coefficient, it was adopted the correlation for sphere proposed by Morrison (60):

$$C_D = \frac{24}{Re} + \frac{2.4 \cdot \frac{Re}{5.0}}{1 + (\frac{Re}{5.0})^{1.52}} + \frac{0.411 \cdot (\frac{Re}{2.63 \cdot 10^5})^{-7.94}}{1 + (\frac{Re}{2.63 \cdot 10^5})^{-8.00}} + \frac{0.5 \cdot \frac{Re}{10^6}}{1 + \frac{Re}{10^6}} \quad (5.6)$$

Where

C_D is the drag coefficient (-)

Re is the Reynolds number (-)

The *equation 5.6* is considered valid both for the SiLibeds and for the quartzite gravel samples analysed, in a range of Reynolds from 10^0 to 10^6: it is expressed as:

$$Re = \frac{\rho_M \cdot u_p \cdot d_p}{\mu_M} \quad (5.7)$$

Where

ρ_M is the medium density (kg/m^3)

u_p is the particle speed (m/s)

d_p is the particle diameter (m)

μ_M is the medium dynamic viscosity (Pa·s)

For a viscid fluid, another non-dimensional number to keep in consideration to properly evaluate the heat exchange is the Prandtl number, that relates the cinematic viscosity with the thermal viscosity of a medium, express with:

$$Pr = \frac{\mu_M \cdot cp_M}{k_M} \tag{5.8}$$

Where

μ_M is the medium viscosity (Pa·s)

cp_M is the medium heat capacity (J/kgK)

k_M is the medium thermal conductivity (W/mK)

For flow around stationary particles, it was proposed the correlation by Ranz and Marshall (61), where the speed expressed in the Reynolds number is the relative velocity between the particle and the medium:

$$Nu = 2 + 0.6 \cdot Pr^{0.33} + Re^{0.5} \tag{5.9}$$

Where

Nu is the Nusselt number (-)

Pr is the Prandtl number (-)

Re is the Reynolds number (-)

The Nusselt number is the adimensional group that express the ratio between the heat transfer due by convection and the heat transferred by conduction, defined as:

$$Nu = \frac{h \cdot d_p}{k_M} \tag{5.10}$$

Where

h is the heat transfer coefficient (W/m^{2}K)

d_p is the particle diameter (m)

k_M is the medium thermal conductivity (W/mK)

From the *equation 5.10* it was obtained the heat transfer coefficient, that express the energy amount transmitted through convection, from the sphere to the liquid.

The total amount of time which constitutes the heat transfer was divided into infinitesimal timestep, to reach a better estimation of fluid and particle properties, of the non-dimensional numbers investigated and of the energy exchanged for each instant. The timestep length is not constant: when the particle reaches the liquid surface, is subjected to a suddenly deceleration, so the timescale discretization is smaller.

The energy is first transferred from the hot particle to the air and then to the cold fluid, changing its temperature for each subsequent timestep. For each of them, the model plans to estimate the amount of energy lost by the sphere as:

$$E_{tot_{1-2}} = h \cdot A_p \cdot \Delta T_{p-m} \cdot \Delta t_{t_{1-2}} \tag{5.11}$$

Where

$E_{t_{1-2}}$ is the energy lost from the particle between two subsequent timesteps (J)

h is the heat transfer coefficient (W/m^{2}K)

A_p is the particle area (m^2)

$\Delta t_{t_{1-2}}$ is length of the timestep (s)

ΔT_{p-m} is difference of temperature between the particle and the medium (K)

In this analysis, the internal temperature of the sphere was considered constant, consequently the conductive term is negligible, because the Biot number is low. Furthermore, the radiative heat exchange was neglected, because the term is some order of magnitude bigger.

The evaluation of the particle temperature after each timestep comes from the correspondent energy lost, through the equation:

$$\Delta T_{t_{1-2}} = \frac{E_{t_{1-2}}}{m_p \cdot cp_p} \tag{5.12}$$

Where

$\Delta T_{t_{1-2}}$ is the difference of temperature between two subsequent timesteps (K)

$E_{t_{1-2}}$ is the energy lost from the particle between two subsequent timesteps (J)

m_p is the mass of the particle (kg)

cp_p is the heat capacity of the particle material (S)

Finally, the fundamental parameter that represents the purpose of this study is the temperature change rate of the particle:

$$\frac{dT}{t} = \frac{\Delta T_{t_{1-2}}}{\Delta t_{t_{1-2}}} \tag{5.13}$$

5.1.2 Properties of materials

The model described in the *chapter 5.1.1* represents the theoretical support for the experiment performed. First, when the particle is dropped was cooled by air at ambient conditions, then reached the surface of the cold liquid. It is Mono Propylene Glycol (MPG), chosen instead the water for its higher viscosity, that allows a low speed of the particle inside the liquid bath and an easier validation of the model through the experiment described in *chapter 5.1.4.* The sample of particle tested is smaller compared to the one used for the pressure drops experiments performed in the *chapter 4.2*: both the size of SiLibeds glass (small and large), but only the medium size for the quartzite gravel, because the smallest size involved very low efficiency. The Pyrex glass was not tested for economic reasons, explained at the beginning of *chapter 5.*

The estimation of the geometrical properties for the SiLibeds glass and for the Quartzite gravel are listed in the *chapter 4.1.*

The thermal conductivity and the heat capacity for the different HSM are useful for the thermal behaviour of the sample. The range of temperature selected for the particle in the experiments is from T=15° to T=450°, where for both glass and quartzite gravel the thermal conductivity is almost constant, but the heat capacity is subjected to high variation.

	k (W/mK)	***Cp (kJ/kgK)***
SiLibeds glass	1.135 (51)	$0.150 + 2.36E-03 \cdot T - 1.37E-06 \cdot T^2$ (54)
Quartzite gravel	2.0 (62)	$0.844 + 1.04E-03 \cdot T - 5.56E-07 \cdot T^2$ (63)

Table 5-1:Thermal conductivity and heat capacity for Silibeds glass and for quartzite gravel

The temperature is expressed in Celsius. The approximation of the heat capacity of the material is sufficient with a polynomial of second grade, because in both cases the error in the estimation is lower than 2%.

For the lack of a complete datasheet for the MPG, its viscosity was measured experimentally, assuming its temperature constant at 15°C, through the Hagen-Poiseuille equation (64). It relates the fluid viscosity with the pressure drops of an uncompressible fluid that passes along a cylindrical pipe at constant speed with laminar flow:

$$\Delta P = \frac{8 \cdot \mu \cdot L \cdot Q}{\pi \cdot R^4} \tag{5.14}$$

Where

ΔP is the difference of pressure between inlet and outlet of the pipe (Pa)

μ is the viscosity of the medium (Pa·s)

L is the length of the pipe (m)

Q is the volumetric flow rate of the liquid (m^3/s)

R is the radius of the pipe (m)

The pipe must be chosen with a length with higher order of magnitude with respect to its radius: the pipe used has a radius R of 2.5 mm and a length L of 2.53 m.

The pressure drops are measured with a similar procedure respect to that one described in the *chapter 4.2.1:* a hydrostatic head upstream the system lets the MPG flow at constant speed through a pipe. The pressure is measured upstream and downstream through some T-valve, each with 3 ways. As showed in the *figure 5.2* on the left, the valve upstream is connected with the MPG container that represents the hydrostatic head, with the red pipe of radius R and length L, where the glycol flows, and with a transparent pipe, needs to measure the pressure there. The valve downstream, as showed in the *figure 5.2* on the right, had as inlet the red pipe, one outlet pipe that discharge the glycol and a transparent pipe to read the pressure in that point. The pressure was read measuring the difference of level of the MPG in the two different transparent pipes at free surface, showed in the *figure 5.3*.

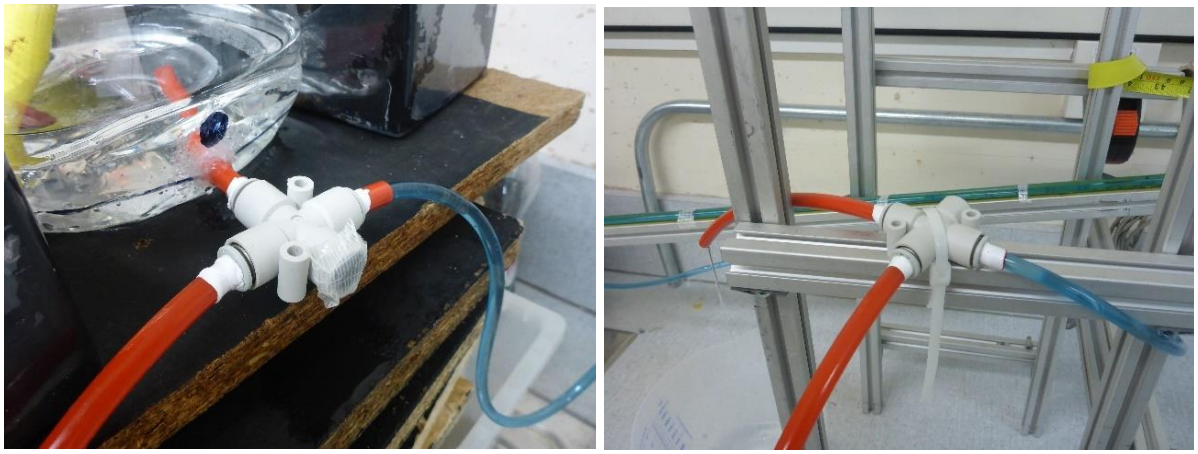

Figure 5-2:On the left: Upstream T-valve. On the right: Downstream T valve

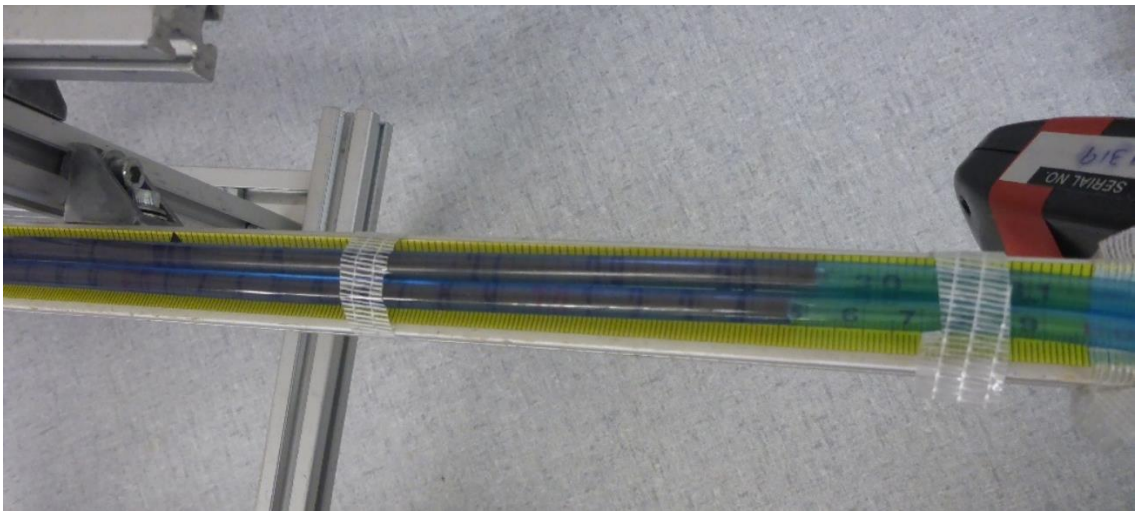

Figure 5-3:Difference of pressure between the two ends of the pipe, measured as the height difference ant free surface

The flowrate and the consequently MPG speed were calculated in the same method used in *chapter 4.2.1*, weighting the mass of glycol that flows in a certain interval of time.

In a cylinder, the flow become turbulent when Re>2300: to ensure a lower possible error in the estimation of the MPG dynamic viscosity, its flowrate and its speed during the experiment is picked lower possible. It was chosen a speed range from 2.6 to almost 10 mm/s, that involved a maximum Re value of 1.16: the hypothesis imposed by Hagen-Poiseuille law was respected.

For each value of speed recorded in the experiment, it was estimate a value of viscosity, with an average value of $0.0434\ Pa \cdot s$. The average error in the estimation was 5.6%.

The temperature assumed for both air and MPG in the experimental evaluations is 15°C, at ambient pressure. The density, the thermal conductivity and the heat capacity for both fluids involved and air viscosity are picked from a database of ASPEN Multiphysics® and are summarized in the *table 5.2*.

	ρ ***(kg/m³)***	***Cp*** ***(J/kgK)***	***k*** ***(W/mK)***	***μ*** ***(Pa· s)***
Glycol	1040	3237.4	0.187	4.34E-02
Air	1.2	1006.2	0.025	1.8E-05

Table 5-2:Thermodynamic properties for MPG and Air from ASPEN Multiphysics database®

5.1.3 Results of the simulated model for different HSM

The analytical model developed in the *chapter 5.1.1* was adopted for the HTM analysed in this section: large and small sized SiLibeds glasses and medium sized Quartzite gravel. The initial difference of temperature between the sample of HSM and the MPG was varied, assuming the values of 450, 400 and 300°C. Obviously, the length of the speed transient changed only between materials with different diameter, density or shape, while the different initial dT influenced the length of the thermal transient, whose behaviour is strictly related also with the dynamic of the system.

In the *figure 5.4* was shown the speed evolution of the different samples of material: they accelerated until they go through the air: at the distance of 0.11 m, they touched the surface of the glycol and immediately decelerate. The space needed to reach a stationary speed is very short, almost 3 cm in average. This value is not exactly the same for the different samples but is similar.

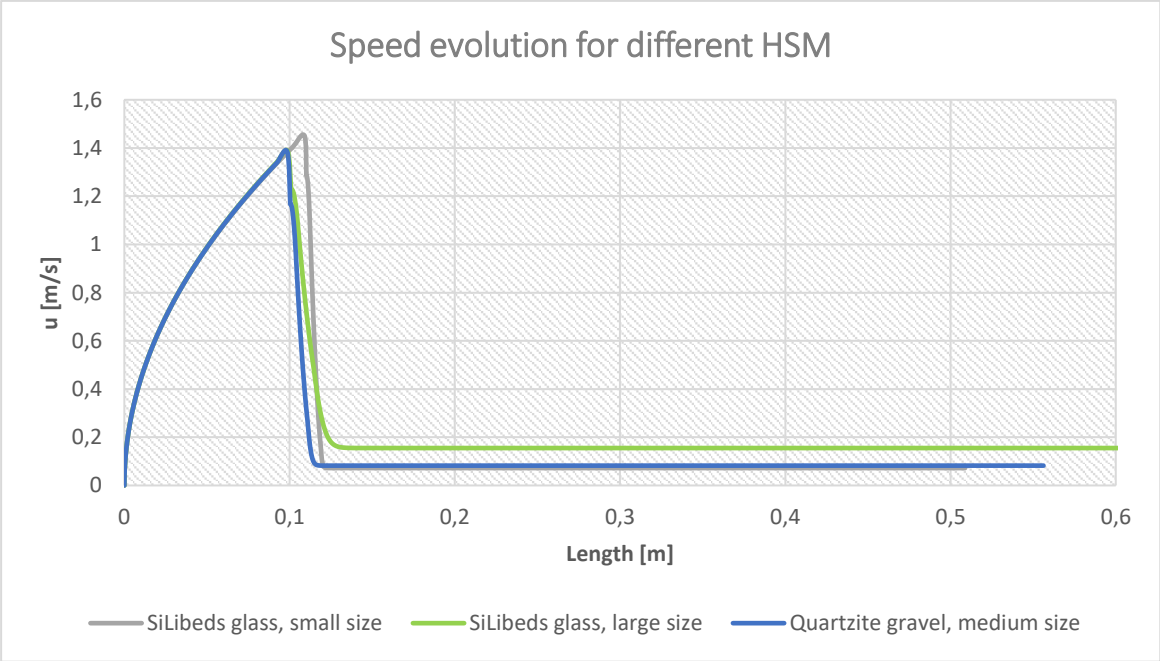

Figure 5-4:Speed evolution for different HSM

The *figure 5.5* represented the temperature evolutions of the samples along the cold bath of MPG, in the case of a ΔT_{MAX} of 450 °C: their behaviours had different shapes, depending principally on their different average diameter. The smallest sized had a thermal transient of

almost 20 cm, very smaller if compared with the largest sized (50 cm), but in any situation the 60 cm deep bath is sufficient.

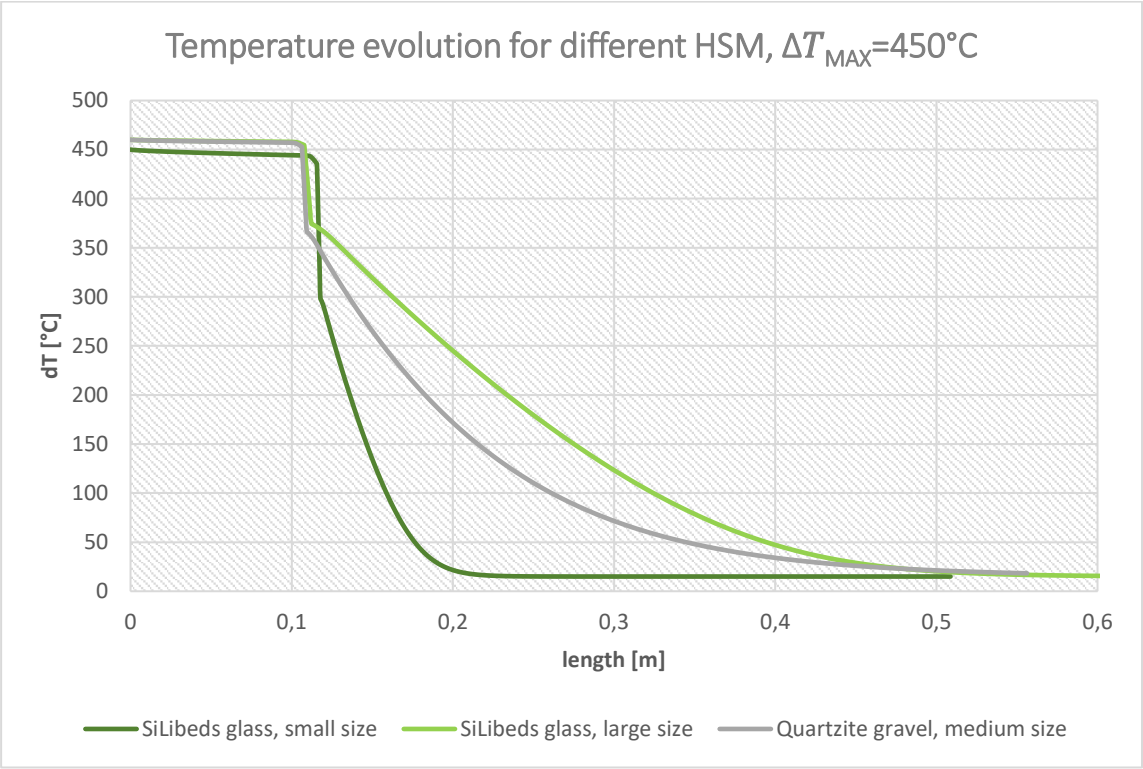

Figure 5-5:Temperature evolution for different HSM, ΔTMAX=450°C

Through the model proposed, it was definitely possible to estimate the relation between the maximum value of $\frac{dT}{t}$ and the corresponding maximum dT, for the different HSM:

	ΔT_{MAX}	$\frac{dT}{t}_{MAX}$
SiLibeds, small size	*450*	*1751.1*
	350	*1608.2*
	300	*1477.3*
SiLibeds, large size	*450*	*708.6*
	350	*624.2*
	300	*584.0*
Quartzite gravel, medium size	*450*	*895.1*
	350	*711.8*
	300	*623.9*

Table 5-3:Maximum difference of temperature and relative maximum dT/t for different samples

5.1.4 Experimental validation of the dynamic part of the heat transfer model

They were performed some experiments with the purpose to validate the results obtained from the model. It appears too complicated to evaluate the thermal transient, that means evaluate the temperature of the particle for a fixed interval of time, but it was propose a method to validate only the dynamics of the motion. The speed of the particle sample that moves across the cold bath of MPG is measured recording a video with a camera and consequently evaluating the space travelled for each photogram. The glycol was chosen as cold liquid instead water because it is more viscous, that means a slower particle and more efficient approximation.

The quartzite gravel particles were not used in that experiment: for their very irregular shape, probably their approximation would have been worse than SiLibeds glass.

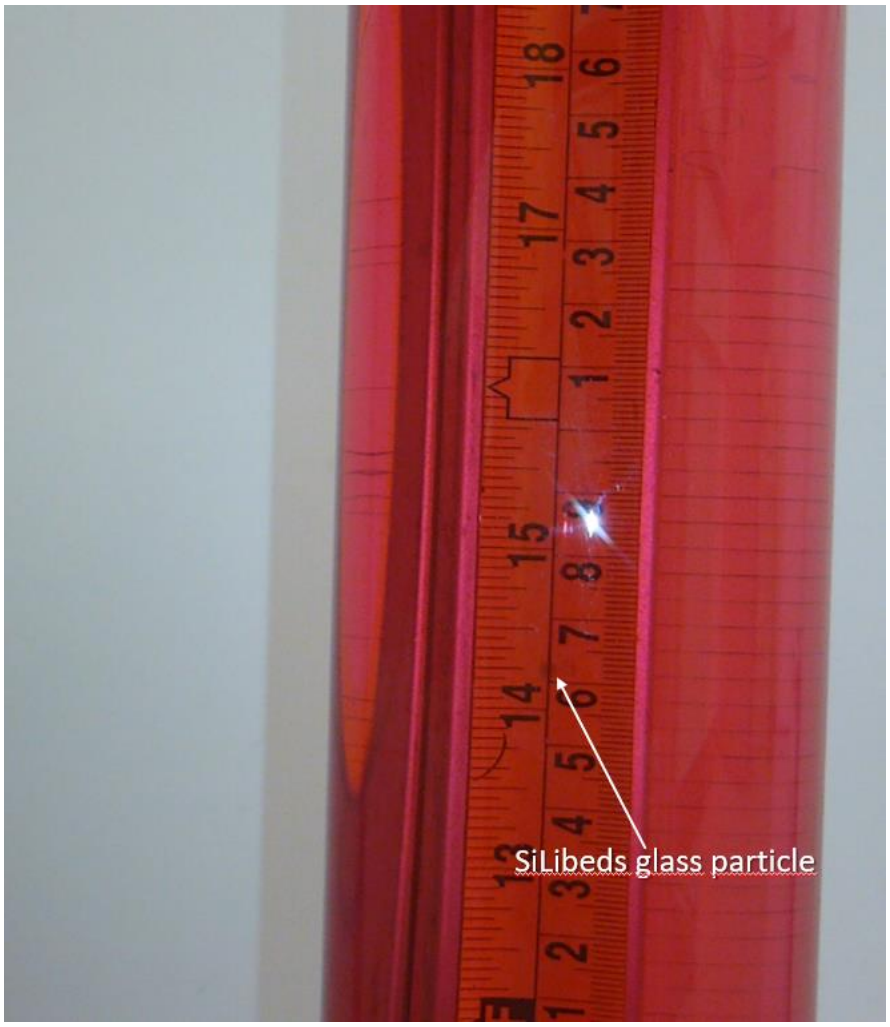

Figure 5-6:A single photogram of a Silibeds glass particle moving down in the MPG bath

The deceleration of the particles is impossible to measure, because it lasts only a small fraction of second, in which the particle travel for some millimetres, so the only part of the model that could be validates is the stationary. To compare the results of the model and the experimental value for the stationary particle speed, the number of experiments performed consists in 20 measures for each sample, 10 for the most regular shaped and 10 for the most irregular shaped selected.

In the *figure 5.7* and *5.8,* they are displayed all the experimental measurements recorded with the method described above: obviously for both the size samples, the most regular shaped particles tend to have a more constant behaviour. For the small size, the dispersion of the experimental results, expressed as the average of the dispersion of each measurement show in the *equation 5.15*, is 5.0% for the regular shaped and 7.8% for the irregular's.

The analysis of the large size particles gave a better uniformity, with a dispersion of 1.5% for regular shaped and 4.8% for the irregular's.

$$\epsilon_{DISP,i} = abs\ (1 - \frac{u_{sample,i}}{u_{average}}\ ) \tag{5.15}$$

Where

$\epsilon_{DISP,i}$ is the difference between the value of each measurement respect to the average value (-)

$u_{sample,i}$ is the speed for each measurement (m/s)

$u_{average}$ is the average speed of all the measurements (m/s)

The difference of uniformity between the different size samples is the average speed: bigger particles mean higher speed and less relative dispersion.

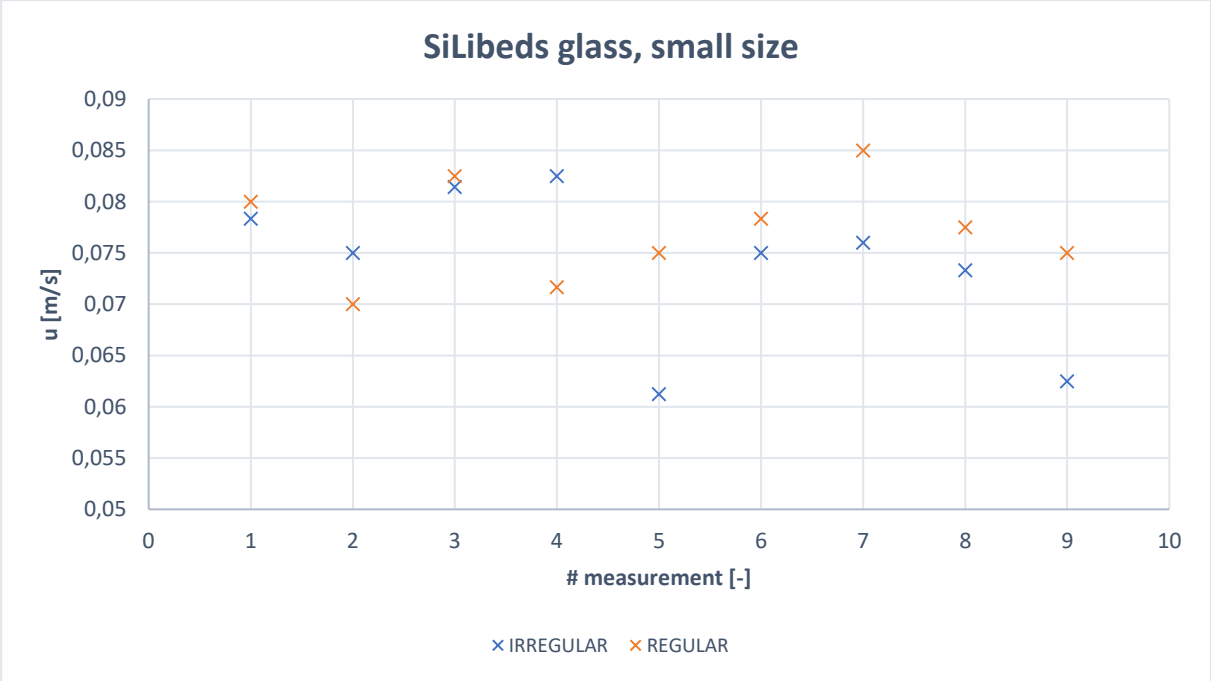

Figure 5-7:Particle speed recorded for different experiments, SiLibeds glass, small size

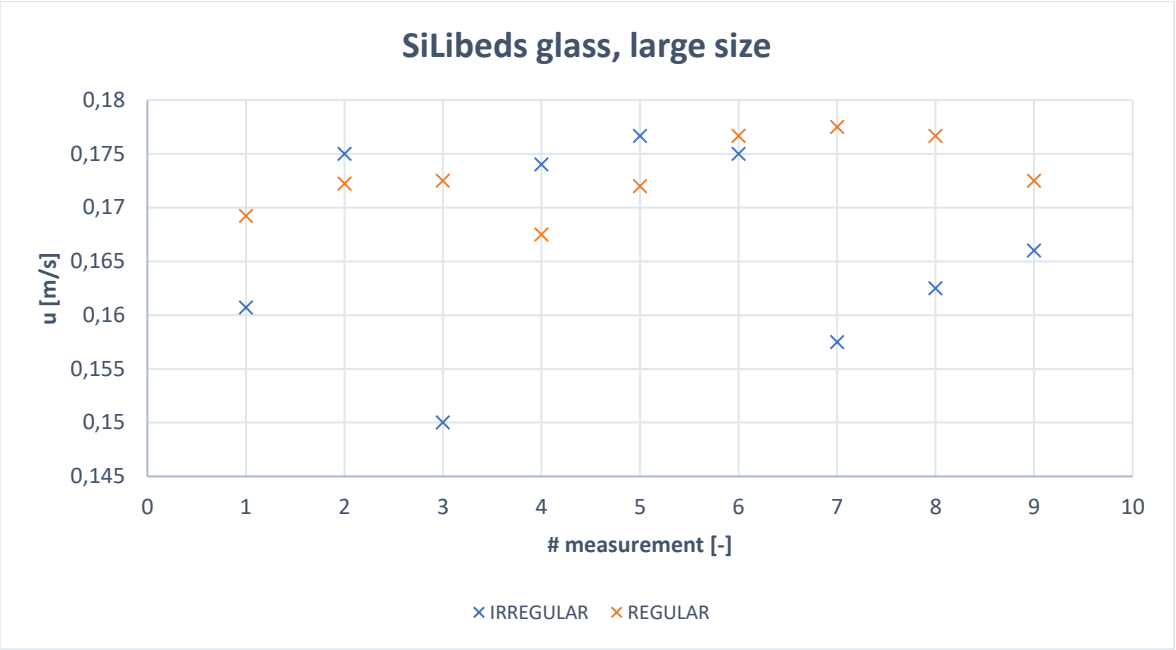

Figure 5-8:Particle speed recorded for different experiments, SiLibeds glass, large size

The purpose of this experiments is to validate the model described in the chapter 4.4.1: the average value of the speeds measured is compared to the stationary speed in the model, for each size of sample, as shown in the *table 5.4*.

	Model stationary speed (m/s)	***Experimental average speed (m/s)***	***Error (%)***
Small size, regular shaped	0.0723	0.0772	6.8
Small size, irregular shaped		0.0739	2.3
Large size, regular shaped	0.1556	0.1730	11.2
Large size, irregular shaped		0.1666	7.1

Table 5-4:Error of the thermodynamic model for the Silibeds glass samples

The total error of the model proposed in the *chapter 5.1,* defined as the average of the errors listed in the *table 5.4* is 6.8%: the model could be considered valid and the error are probably due to the assumption done or in estimating the correct value in the experiments.

5.2 Thermo-mechanical fatigue

It was performed a further experimental study, with the goal of evaluating the qualitative behaviour of different material and size samples if they are subjected at thermo-mechanical fatigue, estimating their resistance and integrity at different $\frac{dT}{t}$. From the model described in the *chapter 5.1*, it is possible to estimate a direct relationship between the maximum $\frac{dT}{t}$ and the corresponding maximum dT between the hot spheres and the cold bath at fixed temperature.

5.2.1 Layout and description of the experiment

The idea is to heat up the spheres particles of Silibeds glass and quartzite gravel until they reach a defined temperature, corresponding of a chosen value of 465, 415 or 365°C. Considering the MPG bath at fixed temperature of 15°C, the maximum dT evaluated are 450, 400 and 350°C, that correspond to the maximum $\frac{dT}{t}$ listed in the *table 5.3.*

A fixed number of spherical particles were heated through a hot air flux, supplied by an air gun, model STEINEL HG3000SLE®, as it possible to see in the *figure 5.9*: the particles are placed in a sieve with a small size mesh, at the outlet of a pipe connected to the gun. The temperature of the air could be set at different level, through a thermos-controller on the gun, in a declared range from 50°C to 650°C, also if realistically the maximum temperature reached was less than 500°C.

Figure 5-9:Layout of the system. On the left: SiLibeds particles are warming up. On the right: MPG cold bath

The temperature was monitored by the thermocouple DIGITRON 2024T®, whose sensor was placed between the spheres. After ensuring that all the particles were at the same temperature, they were picked up one by one with a tweezers and dropped in the cold bath of MPG, from a fixed point at the same height estimated in the model. Considering the thermal transient of the particle along the liquid represented in the *chapter 4.4.3,* when it reached the bottom of the container, it was cooled down until reaches the bath temperature.

All the spheres were recovered and subjected to a mechanical load, to accelerate the test. This was performed inserting each particle between two stainless steel plates, represented in *figure 5.10*: the superior plate was loaded with a increasing weight, from 1 to 11 kg, corresponding to a range of almost 10 to 108 N, recording the number of particle that broke at each weight. Considering the Hertzian contact between a plate and a sphere, for the small size of Silibeds sample the maximum pressure applied could reach 2863 MPa (65).

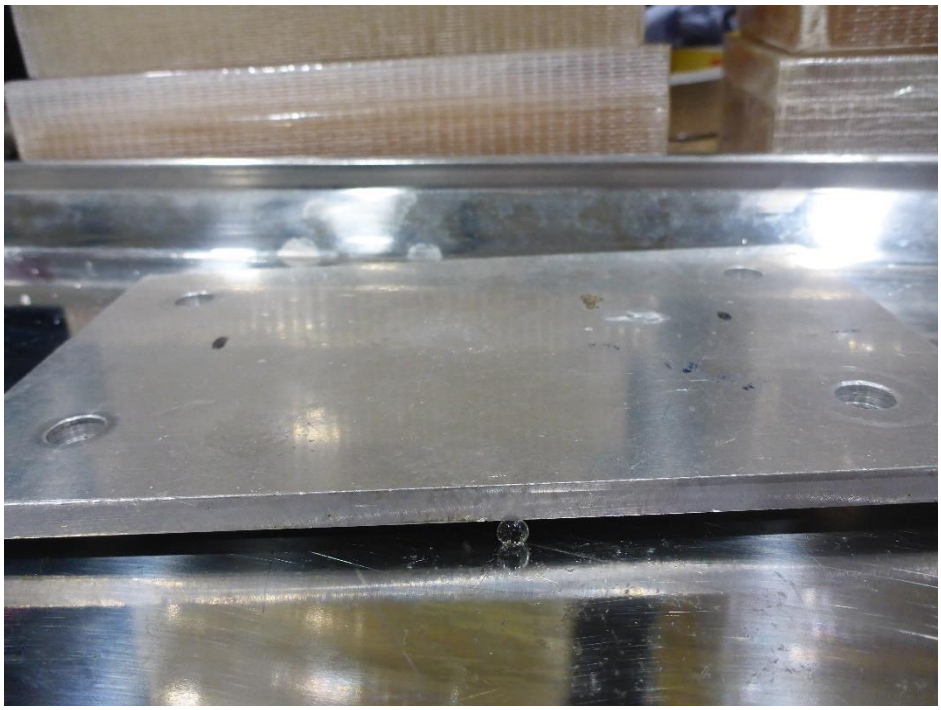

Figure 5-10:Mechanical load: a SiLibed glass sample between two plates

All the samples survived at this procedure, were subjected at another equal heating and cooling process, followed by the same mechanical load procedure. This cycle is repeated until all the particles tested broke. The number of samples used in each experiment was between 25 and 35, considered enough to ensure a good estimation of the different material thermal resistance.

5.2.2 Results and discussions

The results of the experiments for each sample, with the corresponding dT, was gathered and analysed, to observe the rupture trend of the different material samples. From the figure 5.11 to the figure 5.13, it was shown the cumulative of the rupture for each sample at the dT of 300 K, highlighting the rupture weight at each cycle of the thermo-mechanical stress proposed.

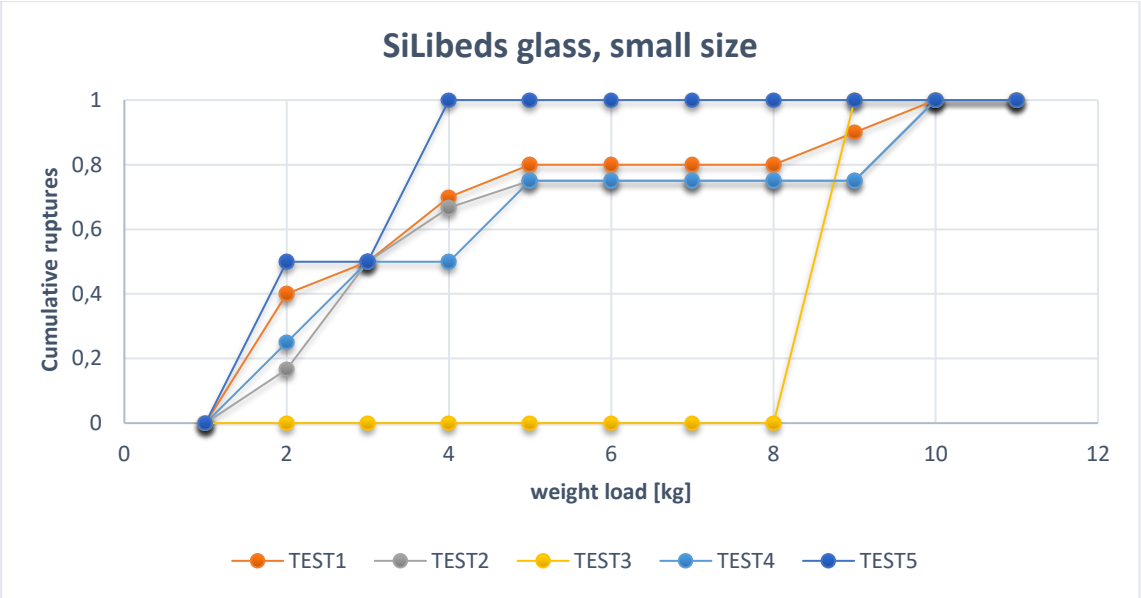

Figure 5-11:Cumulative of the sample's rupture in function of the weight loaded for each thermo-mechanical cycle, SiLibeds small size

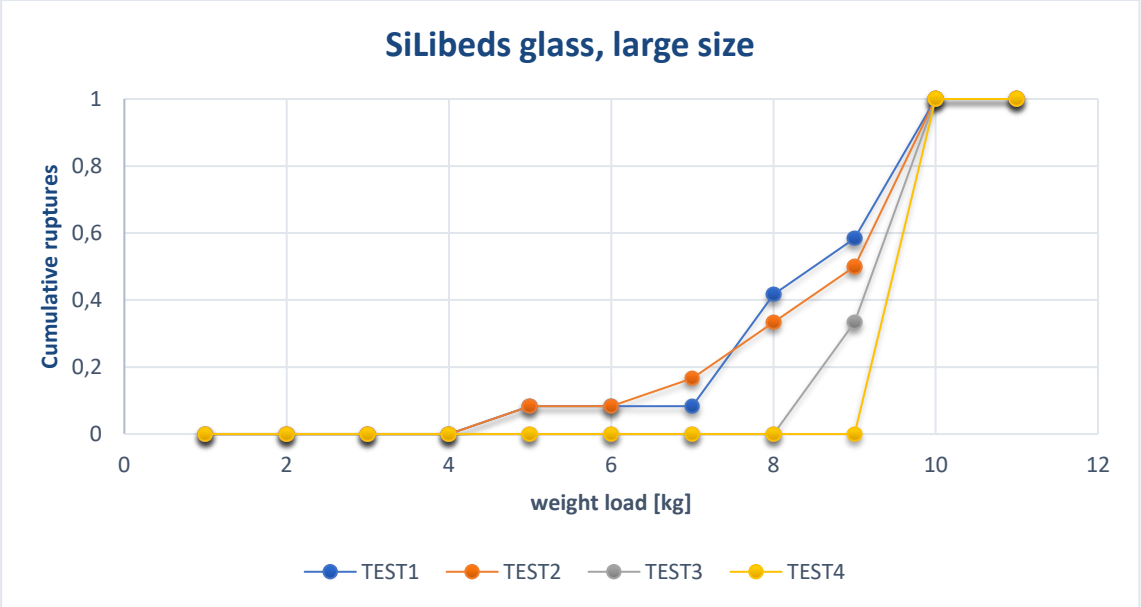

Figure 5-12:Cumulative of the sample's rupture in function of the weight loaded for each thermo-mechanical cycle, SiLibeds large size

From this evaluation it is possible to see a defined shape for the SiLibeds glass, both for the small and the large size: for each number of cycle, the behaviour of the rupture weight is very similar, except the third cycle for the small size samples, that presented only one rupture at 8

kg. From this type of study, it was possible to observe an higher rupture load for the larger samples, that implies higher mechanical resistance.

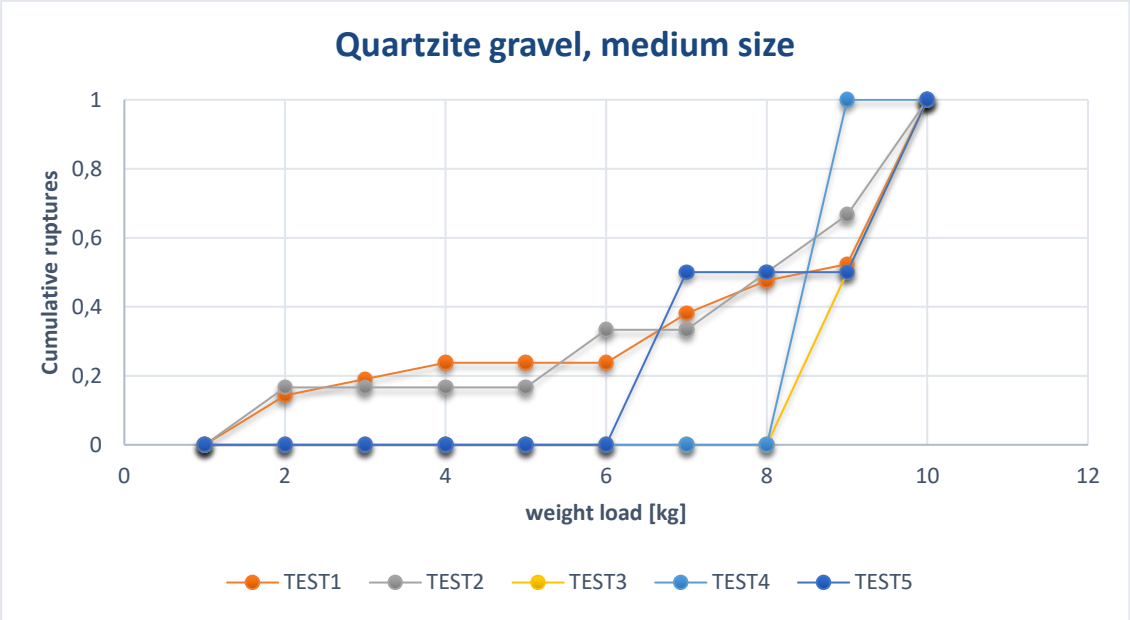

Figure 5-13:Cumulative of the sample's rupture in function of the weight loaded for each thermo-mechanical cycle, Quartzite gravel medium size

More dispersed results were obtained for the quartzite gravel, because the nature of the sample analysed, with this material, was very heterogeneous and it was impossible to establish a correct prediction on the results. Both SiLibeds and quartzite gravel recorded the totality of samples broken after the fifth cycle, that implies a similar resistance at thermos-mechanical fatigue.

A further discussion about the results obtained was performed to establish a relation between the $\frac{dT}{t}$ and the correspondent number of cycle of rupture for the spheres of each material. The procedure adopted consists into estimate an equivalent number of cycle, in which all the particles are broken, varying the difference of temperature of the thermal shock which are subjected to. It was necessary to find a method to consider also the variation of mechanical load. Imposing a different maximum load, that instead 11 kg became for example 3 kg, they were accounted the samples broken for each cycle, considering that a particle that breaks at higher load at *N*-cycle, would break ideally at the *N+1* cycle, at the same imposed maximum weight. Then it was estimated the percentage of the particles broken for each cycle. To calculate the equivalent number of survival cycles for each temperature, the weighted percentages,

obtained multiplying the real percentage with a weighted factor *i,* of each cycle are summed. The factor *i,* is equal at the number of cycle when the sample was broken.

$$\#\ cycles_{eq} = \left(\sum_{i=1}^{N} \%_{rupture,i} \cdot i\right) \tag{5.16}$$

Where

$\#\ cycles_{eq}$ is the estimated equivalent number of cycles of resistance of a specific sample, assuming a specified maximum mechanical load (-)

$\%_{rupture,i}$ is the percentage of the sample broken in the cycle i (-)

i is the weighted factor, correspond at the number of each rupture cycle (-)

In the *table 5.5* it is presented, as an example, the number of equivalent cycles obtained for the SiLibeds glass, small size, with the assumption of the maximum mechanical load of 3 kg, as mentioned before.

dT	$\%_{rupt,1}$	$\%_{rupt,2}$	$\%_{rupt,3}$	$\%_{rupt,4}$	$\%_{rupt,5}$	$\%_{rupt,6}$	$\%_{rupt,7}$	$\#\ cycles_{eq}$
450	73,3%	26,7%	-	-	-	-	-	**1,27**
350	18,8%	71,9%	9,4%	-	-	-	-	**1,91**
300	17,2%	37,9%	20,7%	10,3%	10,3%	3,4%	6,9%	**3,17**

Table 5-5:Percentage of rupture on each thermo-mechanical cycle for Silibeds glass, small size with maximum mechanical load of 3 kg

The same approach was adopted considering also 5 and 7 kg as the maximum mechanical load: for each sample, the corresponding equivalent numbers of cycle obtained are the average of the value obtained with the different assumptions. With this qualitative approach it was possible to consider the influence of the different load of rupture, simplifying the elaboration of the results obtained from the experiments. Finally, it was possible to represents the $\#\ cycles_{eq}$ only in function of the correspondent $\frac{dT}{t}$.

	dT	$\frac{dT}{t}$	$\#\ cycles_{eq}$
SiLibeds, small size	*450*	*1751.1*	*1.11*
	350	*1608.2*	*1.67*
	300	*1477.3*	*3.01*
SiLibeds, large size	*450*	*708.6*	*1.90*
	350	*624.2*	*2.10*
	300	*584.0*	*2.39*
Quartzite gravel, medium size	*450*	*895.1*	*1.64*
	350	*711.8*	*2.07*
	300	*623.9*	*3.32*

Table 5-6:Equivalent number of cycles for each sample analysed, in function of the respective dT/t

To understand better the evolution of the equivalent number of cycle of surviving for the different samples in function of different $\frac{dT}{t}$, their behaviours are represented in the figure 5.14.

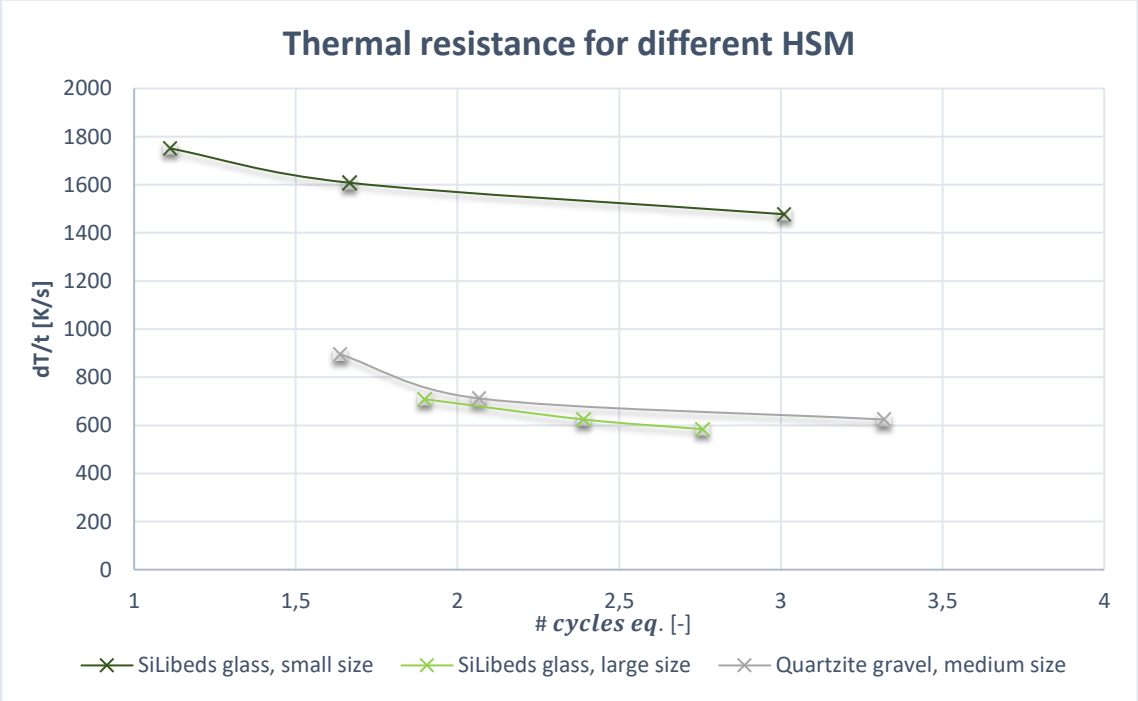

Figure 5-14:Behaviour of the thermal resistance for different HSM

The behaviour of the curves represented in the figure 5.14 demonstrates better thermal performances for the small size of SiLibeds glass. From this analysis, it is evident that the influence of the diameter is bigger than the difference of material. However, with this method it was obtained only a qualitative trend of the thermal resistance of the different material and the data available are not sufficient to predict a precise behaviour for higher number of cycles, maybe equal at the life of the plant.

The thermo-mechanical resistance of the various type of material allows to understand how long they resist without breaking or getting damaged.

To verify the qualitative validity of the thermal model, from the literature (66) it appears a direct empirical relation between the difference of temperature that cause immediate failure for a sphere, knowing its mechanical properties and the Biot number *Bi*.

$$\Delta T_{max} = \frac{2.5 \cdot (2 + Bi) \cdot (1 - \gamma) \cdot \sigma_t}{Bi \cdot \alpha \cdot E} \tag{5.17}$$

Where

ΔT_{max} is the difference of temperature that causes an immediate failure (K)

γ is the Poisson ratio (-)

σ_t is the breaking tensile stress (Pa)

E is the Young's modulus

Bi is the Biot number (-)

α is the coefficient of thermal expansion (1/K)

The model developed in this chapter express a relation between the instant difference of temperature and the number of cycles: through the definition of the Biot number, it was possible to express the heat transfer coefficient *h* in function of $\frac{dT}{t}$, considering both the conductive and the convective mechanism for the heat transfer:

$$Bi = \frac{\frac{dT}{t} \cdot m \cdot c_P}{k \cdot A \cdot \Delta T} \cdot L \tag{5.18}$$

Where

$\frac{dT}{t}$ is the instant difference of temperature between the particle and the fluid (K/s)

m is the mass of the particle (kg)

c_P is heat capacity (J/kgK)

A is external surface of the particle (m^2)

k is thermal conductivity (W/mK)

L is the characteristic length (m)

ΔT is the difference of temperature between the particle and the fluid (K)

Obtaining explicitly the term $\frac{dT}{t}$, by replacing the *equation 5.18* in *5.17*, it was found the expression:

$$\frac{dT}{t}_{max} = 5 \cdot \frac{k \cdot A}{m \cdot c_p \cdot L \cdot \left(\frac{\alpha \cdot E}{(1-\gamma) \cdot \sigma_t} - \frac{2.5}{\Delta T_{max}}\right)} \tag{5.19}$$

Where

$\frac{dT}{t}_{max}$ is the maximum instant difference of temperature between the particle and the fluid, that generates an immediate rupture of the particle (K/s)

m is the mass of the particle (kg)

c_P is heat capacity (J/kgK)

A is external surface of the particle (m^2)

k is thermal conductivity (W/mK)

L is the characteristic length, defined as the ratio between the volume and the external surface (m)

ΔT_{max} is the difference of temperature between the particle and the fluid, obtained with the equation CC1(K)

γ is the Poisson ratio (-)

σ_t is the breaking tensile stress (Pa)

E is the Young's modulus

α is the coefficient of thermal expansion (1/K)

The mechanical properties for the SiLibeds glass and for the quartzite gravel are summarized in the *table 5.7*

	Poisson ratio (-)	***Young mod. (GPa)***	***Max compression stress (MPa)***
SiLibeds glass	*0.22*	*61-64* (67)	*187, small size* *136, large* (51)
Quartzite gravel	*0.15-0.35* (68)	*63.8* (69)	*110* (69)

Table 5-7:Mechanical properties for different HSM

The *equation 5.19* allows to find the $\frac{\mathrm{dT}}{\mathrm{t}}_{\mathrm{max}}$, that corresponds to an immediate rupture of the sample: it is possible to consider that these results correspond at zero number of cycle equivalent and they were compared with the data in the *table 5.6*.

The $\frac{dT}{t}_{max}$ depends only on the material and on the size of the particles:

	ΔT_{max}	$\left(\frac{dT}{t}\right)_{max}$	$\#\ cycles_{eq}$
SiLibeds, small size	*1616.8*	*13605.2*	*0*
SiLibeds, large size	*1004.2*	*2494.6*	*0*
Quartzite gravel, medium size	*1404.1*	*3985.2*	*0*

Table 5-8:Maximum dT/t corresponding at the immediate rupture of the sample for different HSM

The values show in the *table 5.8* could confirm the smaller samples of Silibeds glass have higher resistance to the thermal shock, with respect to the bigger size, with a ΔT_{max} 50% higher and a $\left(\frac{dT}{t}\right)_{max}$ four times higher. The qualitative model presents only a general evaluation of the response of the different material proposed for the heat storage: with this model it is impossible to predict exactly the number of life-cycle that correspond to the real system, where the HSM is subjected at $\frac{dT}{t}$ of 50 K/s. From a thermal resistance point of view, the quartzite gravel has a similar trend with respect to the SiLibeds glass. An influent drawback for the gravel is represented by a very low uniformity in size, that makes more difficult an exact estimation of its behaviour.

6 Conclusions and future perspectives

In the last few years, the LAES technology reached increasing interests as electric storage system, proving to be a potential alternative with respect to PHS and CAES.

In particular, this work proposed the investigation of a fundamental component for the LAES technology: The Cold Energy Storage. Its performances were evaluated by varying a set of inlet parameters through an analytical model, that allows to determine the more efficient configuration, considering some technical and economic constrains.

Once obtained a sufficient database of different layout configuration, they were proposed three different approximation methods with the purpose of extracting the efficiency of the system, with whatever parameter combination, without resorting to the analytical model. These methods were considered very effective, because they reached an error on the estimation of the exact value of 1-2%

From the first analysis, it was evident the influence of the pressure drops across the packed bed of the storage, highlighting the importance of the size and the shape of the HSM. For this reason, they were proposed 3 different samples of storage material, the Pyrex glass, the SiLibeds glass and the Quartzite gravel. Their performances were experimentally compared, and the data extracted were inserted in the analytical model presented previously, reaching better results for the most rounded samples. Despite lower pressure drops were obtained with a bigger size, the best efficiency corresponded to a smaller size of the particles: 92.02 % for the SiLibeds glass samples with a diameter of 2.29 mm.

A further experimental study was developed to test the thermal resistance, comparing the behaviours of different storage materials when they are subjected to a thermal fatigue, to simulate the operational condition of a real system, where their temperature change for almost 120 °C twice each day. Also in this case, the results obtained showed, through a qualitative estimation, a better behaviour for the smaller size, highlighting the limits of resistance for the quartzite gravel: it presents high irregularities in the shape and in the results, complicating its evaluation: it is definitely less resistant than the SiLibeds glass.

A more precise estimation about the lifetime of the different samples could be achieved with the adoption of more performing and accurate experimental instruments, that allows to measure higher value of equivalent survival number of cycle, that corresponds to a lower $\frac{dT}{t}$.

References

1. ***Eurostat.*** *Europe 2020 indicators-climate change and energy. http://ec.europa.eu/eurostat/statistics-explained/index.php/Europe_2020_indicators_-_climate_change_and_energy. [Online]*

2. —. http://ec.europa.eu/eurostat/statisticsexplained/index.php/Renewable_energy_statistics. [Online]

3. ***REN 21 STEERING COMMITEE.*** *http://ec.europa.eu/eurostat/statisticsexplained/index.php/Renewable_energy_statistics. [Online]*

4. ***Engineer planning.*** *https://judithcurry.com/2016/01/06/renewables-and-grid-reliability/. [Online]*

5. Overview of current development in electrical energy storage technologies and the application potential in power system operation. ***Luo, X., Wang, J., Dooner, M.,Clarke, J.***

6. ***Internal Electrotechnical commission.*** *http://www.iec.ch/whitepaper/pdf/iecWP-energystorage-LR-en.pdf. [Online]*

7. ***The Grid.*** *https://thegrid.rexel.com/en-us/energy_efficiency/w/solar_renewable_and_energy_efficiency/345/bulk-vs-distributed-energy-storage-which-approach-will-win?Redirected=true. [Online]*

8. ***Barbour, Edward.*** *http://energystoragesense.com/pumped-hydroelectric-storage-phs/. [Online]*

9. ***Council, World Energy.*** *https://www.worldenergy.org/wp-content/uploads/2016/10/World-Energy-Resources-Full-report-2016.10.03.pdf. [Online]*

10. Progress in electrical energy storage system: a critical review. . ***Chen H, Cong TN, Yang W, Tan C, Li Y, Ding Y.***

11. Electrical energy storage: white paper. Technical report. Prepared by electrical energy storage project team. ***Electrotechnical, International.***

12. Progress in electrical energy storage system: A critical review. Progress in Natural Science. ***Chen, H., Cong, T.N., Yang, W., Tan, C., Li, Y.,Ding, Y.*** *2009.*

13. Pathways for energy storage in the UK. Technical report. Centre for low carbon futures. ***Taylor P, Bolton R, Stone D, Zhang XP, Martin C, Upham P, et al.***

14. characteristics and comparisons. ***Ibrahim H, Ilinca A, Perron J. Energy storage systems.***

15. Liquid air energy storage could become £1bn industry. The Institution. ***E., Gent.***

16. Highview power storage: secure, clean power. ***Highview Power.***

17. Characteristics and technologies for long- vs. short-term. ***SM., Shoenung.***

18. Electricity energy storage technology options: a white paper primer on applications, costs, and options. Electric Power Research Institute (EPRI). ***D., Rastler.***

19. ***Energy Storage Association.*** *http://energystorage.org/energy-storage/technologies/liquid-air-energy-storage-laes. [Online]*

20. ***Highview Power Storage.*** *http://www.highview-power.com/wp-content/uploads/Highview-Brochure-2016-A4.pdf. [Online]*

21. ***Lombardo, Tom.*** *http://www.highview-power.com/wp-content/uploads/Highview-Brochure-2016-A4.pdf. [Online] 2013.*

22. Liquid air energy storage (LAES) with packed bed cold thermal storage – From component to system level performance through dynamic modelling. ***A. Sciacovelli, A. Vecchi, Y. Ding.***

23. Refrigerated Warehouses as Intelligent Hubs to Integrate Renewable Energy in Industrial Food Refrigeration and to Enhance Power Grid. ***24. Fikiin, Kostadin, Borislav Stankov, Judith Evans, Graeme Maidment, Alan Foster, Tim Brown, Jonathan Radcliffe, et al.***

24. Transport Longue Distance Et Stockage D'énergie Calorifique, En Couplage Avec Des Procédés De Valorisation Énergétique Des Déchets. Etude N° 09-0233/1a. ***Mefret, O., L. Bequet, A. Manificat, and C. Weber.***

25. ***Neutrium.*** *https://neutrium.net/fluid_flow/pressure-drop-through-a-packed-bed/ . Pressure drop through a packed bed. [Online] 23 July 2013.*

26. ***Wikipedia.*** *https://en.wikipedia.org/wiki/Kriging. [Online]*

27. ***Weisend, John.*** *https://www.cryogenicsociety.org/resources/defining_cryogenics/joule-thomson_effect/. [Online] 2010.*

28. Performance evaluation of various cryogenic energy storage systems. ***Abdo, R.F., Pedro, H.T.C., Koury, R.N.N., Machado, L., Coimbra, C.F.M.,Porto, M.P.*** *2015.*

29. ***Li, Y.*** *Cryogen based energy storage: process modelling and optimisation. University of Leeds : s.n., 2011.*

30. ***Sciever, S.W.V.,.*** *Helium Cryogenics. International Cryogenics Monograph Series. s.l. : Springer, 2012.*

31. Power augmentation of combined cycle power plants using cold energy of liquefied natural gas. . ***Kim TS, Ro ST.*** *2000.*

32. Evolution of an LNG Terminal: Senboku Terminal of Osaka Gas. ***T, Otsuka.*** *Amsterdam : s.n., 2006.*

33. On the recovery of LNG physical exergy by means of a simple cycle or a complex system. . ***Bisio G, Tagliafico L.*** *2002.*

34. Integration of low-level waste heat recovery and Liquefied Nature Gas cold energy utilization. ***Bai FF, Mang ZX.*** *2008.*

35. Development of Generator of Liquid Air Storage Energy System, Mitsibushi Heavy Industries, Ltd. ***Kenji Kishimoto, K.H., Takahisa Asano.*** *1998.*

36. COLD HEAT REUSED AIR LIQUEFACTION/VAPORIZATION AND STORAGE GAS TURBINE ELECTRIC POWER SYSTEM. ***Wakana, H., Chino, K.,Yokomizo, O.*** *2005.*

37. Thermodynamic analysis of energy storage with a liquid air Rankine cycle. . ***Ameel, B., T'Joen, C., De Kerpel, K., De Jaeger, P., Huisseune, H., Van Belleghem, M.,De Paepe, M.*** *s.l. : Applied Thermal Engineering, 2013.*

38. An analysis of large-scale liquid air energy storage system. Institution of Civil Engineers. ***Morgan, R., Nelmes, S., Gibson, E.,Brett, G.*** *2015.*

39. ***A. Sciacovelli, D. Smith, M. E. Navarro, A. Vecchi, X. Peng, Y. Li, J. Radcliffe and Y. Ding.*** *Performance Analysis and Detailed Experimental Results of the First Liquid Air Energy Storage Plant in the World. ASME Digital collection. [Online] 2017. http://energyresources.asmedigitalcollection.asme.org/article.aspx?articleid=2663016.*

40. Thermodynamic analysis of a liquid air energy storage system. ***Guizzi, G.L., Manno, M., Tolomei, L.M.,Vitali, R.M.*** *2015.*

41. Refrigerated warehouses as intelligent hubs to integrate renewable energy in industrial food refrigeration and to enhance power grid sustainability. ***Kostadin Fikiin, Borislav Stankov, Judith Evans et al.*** *2017.*

42. Comparative thermodynamic analysis of compressed air and liquid air energy storage systems. ***Piotr Krawczyk, Łukasz Szabłowski, Sotirios Karellas, Emmanuel Kakaras, Krzysztof Badyda.*** *2018.*

43. Investigation of storage materials for packed bed cold storages in liquid air energy storage (LAES) systems. ***Lars Huttermann, Roland Span.*** *2017.*

44. An analysis of a large-scale liquid air energy storage system. ***Robert Morgan, Stuart Nelmes, Emma Gibson, Gareth Brett.*** *2014.*

45. ***CRYOHUB.*** *Cryogenic Energy Storage for Renewable Refrigeration and Power Supply. [Online] https://cryohub.eu/en-gb/.*

46. ***E.D. Marquardt, J.P. Le, and Ray Radebaugh.*** *Cryogenic Material Properties Database . s.l. : National Institute of Standards and Technology Boulder.*

47. Measurements of Particle-Liquid Heat lkansfer in Systems. ***S. Mankad, K. M. Nixorf & P. J. Fryer.*** *1997.*

48. ***Neutrium-****Pressure drop through a packed bed.* ***https://neutrium.net/fluid_flow/pressure-drop-through-a-packed-bed. [Online] 2013.***

49. de Smith, Goodchild, Longley. Geospatial Analysis-5th Edition. http://www.spatialanalysisonline.com/HTML/index.html?kriging_interpolation.htm. [Online] 2015.

50. Cameron, K,P Hunter. *Using Spatial Models and Kriging Techniques to Optimize Long-Term Ground-Water* ***Monitoring Networks: A Case Study. [Online] 2002.***

51. Sigmund Lindner GmbH. PDS en Water wells. *SiLibeads – Glass beads for water wells /* ***drinking water abstraction Version: V22/2017. [Online] 2017.***

52. Corning. Property of PIREX,PIREXPLUS and Low Actinic PIREX Code 7740 Glasses. [Online] http://www.quartz.com/pxprop.pdf.

53. LAUSCHA Fiber International. *Cryogenic Insulation Glass Mat.* ***[Online] 2015. www.lfifiber.com/.***

54. *Design and modeling of a high temperature solar thermal energy storage unit based on molten soda lime silica glass.* ***Bruno Cárdenas, Noel León, John Pye, Héctor D. García. 2016.***

55. *Specific heat capacity of Apiezon N high vacuum grease and of Duran borosilicate glass.* ***W.Schnelle, J.Engelhardt, E.Gmelin. s.l. : ELSEVIER, 1999.***

56. *Cryogenic Material Properties Database.* ***E. D. Marquardt, J. P. Le, Ray Radebaugh. 80303.***

57. Stone warehouse.co.uk. [Online] https://www.stonewarehouse.co.uk/gravel-chippings/buff-quartz-chippings-3-8mm.

58. Warehouse.co.uk, Stone. [Online] https://www.stonewarehouse.co.uk/gravel-chippings/trent-pea-gravel-6mm-hazel.

59. Sigmund Linder. *Price list water wells.* ***[Catalogue]***

60. *Data Correlation for Drag Coefficient for Sphere-Department of Chemical Engineering-* ***MIT. Morrison, Faith A. 2016.***

61. *Measurements of Particle-Liquid Heat lkansfer in Systems.* ***S. Mankad, K. M. Nixorf & P. J. Fryer. 1997.***

62. *An overview of thermal energy storage systems.* ***Guruprasad Alva, Yaxue Lin, Guiyin Fang. 2018.***

63. *Experimental investigation of the thermal and mechanical stability.* ***Viola Becattini, Thomas Motmans, Alba Zappone, Claudio Madonna, Andreas Haselbacher. 2017.***

64. WIkipedia. [Online] 2018. https://en.wikipedia.org/wiki/Hagen–Poiseuille_equation.

65. *Advanced Mechanical Engineering solutions.* ***Hertzian contac stress calculator. [Online] http://www.amesweb.info/HertzianContact/HertzianContact.aspx.***

66. W.B. Crandall, J. Ging. *Thermal shock analysis of spherical shapes- Technical report.* ***New York : s.n., 1954.***

67. Cambridge University Engineering Department. Cambridge University Engineering Department. [Online] 2003. http://www-mdp.eng.cam.ac.uk/web/library/enginfo/cueddatabooks/materials.pdf.

68. GEOL 615. *Some Useful Numbers on the Engineering Properties of Materials (Geologic and Otherwise)* ***. [Online] https://sites.psu.edu/tzhu/files/2016/10/Some-Useful-Numbers-1g1rkuu.pdf.***

69. *Stress-strain relationships and modulus of elasticity of rocks and of ordinary and high performance concretes.* ***Wojciech Piasta, Jacek Góra, Waldemar Budzyński. 2017.***